

Title	Hybrid integration and packaging of grating-coupled silicon photonics
Authors	Snyder, Bradley William
Publication date	2013
Original Citation	Snyder, B. W. 2013. Hybrid integration and packaging of grating-coupled silicon photonics. PhD Thesis, University College Cork.
Type of publication	Doctoral thesis
Rights	© 2013 Bradley W. Snyder - http://creativecommons.org/licenses/by-nc-nd/3.0/
Download date	2024-04-24 09:15:51
Item downloaded from	https://hdl.handle.net/10468/1455

Hybrid Integration and Packaging of Grating-Coupled Silicon Photonics

Bradley William Snyder

MSEE MIEEE MSPIE



NATIONAL UNIVERSITY OF IRELAND, CORK

FACULTY OF SCIENCE

DEPARTMENT OF PHYSICS

TYNDALL NATIONAL INSTITUTE

**Thesis submitted for the degree of
Doctor of Philosophy**

11 July 2013

Supervisors: Dr. Peter O'Brien
Dr. Frank H. Peters

Head of Department/School: Prof. John G. McInerney

Research supported by Science Foundation Ireland

Contents

Acknowledgements	v
Abstract	vi
1 Introduction and Motivation	1
1.1 Context	2
1.2 Silicon Photonics	3
2 Related Research	8
2.1 Introduction	9
2.2 Fiber Coupling	9
2.2.1 End-Coupling Techniques	9
2.2.2 Near-Vertical Coupling	10
2.2.2.1 Grating Coupler Theory	10
2.2.2.2 Recent Grating Coupler Research	13
2.2.3 Fiber Arrays	15
2.3 Laser Integration	16
3 Fiber-Coupled Packaging	19
3.1 Introduction	20
3.2 Theory	20
3.2.1 Physical Principle	20
3.2.2 Calculation of Alignment Tolerances	24
3.3 Measurements	27
3.3.1 Alignment Tolerances	27
3.3.2 Coupling Efficiency	30
3.4 Packaging Design Rules	33
3.5 Conclusions	35
4 Fiber Array Packaging	36
4.1 Introduction	37
4.2 Construction	37
4.2.1 V-Grooves	37
4.2.2 Single-Polish Designs	38
4.2.3 Double-Polish Design	40
4.3 Measurements	41
4.3.1 Alignment Tolerances	41
4.3.2 Coupling Efficiency	45
4.4 Packaging Design Rules	47
4.4.1 Alignment Shunts	49
4.5 Conclusions	52
5 Design of Hybrid Integration Technology for Lasers	53
5.1 Hybrid Integration Techniques	54
5.1.1 Actively-Aligned Micromirrors	54
5.1.2 MOEMS-Based Micro-Optical Bench	57
5.1.3 Discrete Component Micro-Optical Bench	58
5.2 Design Process	59
5.2.1 Optical Design	59

5.2.2	Mechanical Design	64
5.2.3	Thermal Design	66
5.2.4	Electrical Design	71
5.3	Conclusions	71
6	Implementation and Testing of Hybrid Integration Technology for Lasers	73
6.1	Introduction	74
6.2	Construction of the Micro-Optical Bench Assembly	74
6.3	Integration with the SOI Chip	78
6.4	Tests and Measurements	82
6.4.1	Alignment Tolerance	82
6.4.2	Tunable Laser Spectrum	82
6.4.3	Coupling Efficiency	84
6.4.4	Thermal Imaging	86
6.5	Conclusions	88
7	Conclusions and Further Work	89
7.1	Summary	90
7.2	Polarization-Dependent Isolator	92
7.3	Laser Arrays and Aspherical Lenses	95
7.4	Final Thoughts	98
A	Zemax Macro Source Listings	101
	Bibliography	104
	List of Figures	113
	List of Tables	115
	Publications	116

I, Bradley William Snyder, certify that this thesis is my own work and I have not obtained a degree in this university or elsewhere on the basis of the work submitted in this thesis.

Bradley William Snyder

To Dr. Jane Chance

Acknowledgements

First and foremost, I would like to thank my supervisor, Dr. Peter O'Brien, for providing me with endless support and mentoring. I could not possibly have asked for a more enthusiastic leader or a better promoter of my research. I look forward to future fruitful collaborations as I continue my career outside of Tyndall.

I must also thank my co-supervisor, Dr. Frank H. Peters, for providing helpful feedback and aiding me in interfacing with the university.

I would like to thank Tyndall National Institute as a whole for providing and maintaining the lab facilities in which this research was conducted, and I would like to thank Science Foundation Ireland for funding this research under Grant 07/SRC/I1173.

Among my colleagues, I would like to thank Cormac Eason for contributing the SolidWorks illustration in Fig. 5.3 as well as the CAD drawings in Figs. 4.4 and 4.6, and for providing me with helpful information concerning the use of the thermal imaging camera. I would also like to thank the various current and former members of my team and of Tyndall National Institute for providing assistance and advice. These include but are not limited to: Marc Rensing, 송정환 (Jeong Hwan Song), 韩威 (Han Wei), 王欣 (Wang Xin), 杨华 (Yang Hua), Nicola Pavarelli, Robert Sheehan, William "Eddie" Cotter, Brian Corbett, Ken Rodgers, Paul Tassie, Carmel Kelleher and Krimo Kalfi.

I would like to extend a special thanks to Andreas Wiczorek for helping me move so many times in my seeming quest to live in every neighborhood in Cork, and to Noreen Nudds for providing a set of steady lab hands with submicrometer precision, and for always having an answer to my practical questions about navigating life in Ireland.

I would also like to thank Prof. Clifford Pollock for writing his *Fundamentals of Optoelectronics*. Though it was already out-of-print by the time I bought it, it has always been my first resort for questions about waveguides, fiber optics and electromagnetics in general. It is also one of the few textbooks that I have ever sat down and read word-for-word.

In addition, I would like to thank the developers of Zemax and COMSOL for writing such superlative simulation software so that I would not have to do an inferior job of writing it myself. I would also like to acknowledge Eblana Photonics, Chuxing Optical Fiber Application Technologies Ltd., Precision Micro-Optics LLC, and L.E.W. Techniques Ltd. for providing Fabry-Pérot lasers, angle-polished fibers, V-groove assemblies and ceramic substrates respectively, as well as Dr. Pieter Dumon and Dr. Amit Khanna of imec and Universiteit Gent for providing a steady supply of test chips.

Finally, many thanks go out to my family, especially my mother, for making me possible and for encouraging me and going to bat for me throughout my life.

Abstract

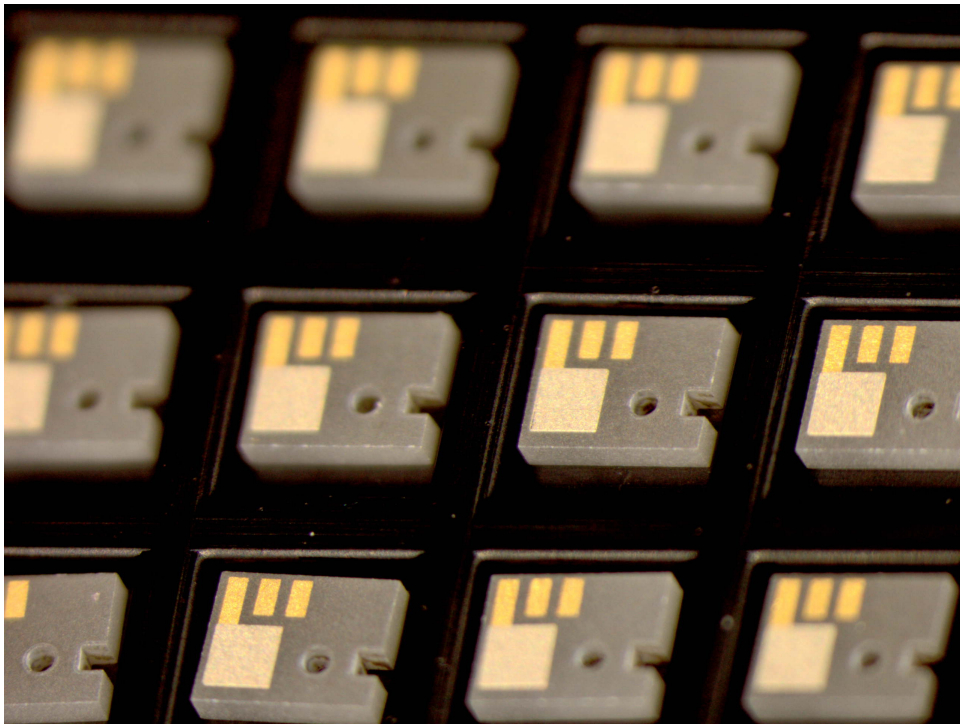
This thesis covers both the packaging of silicon photonic devices with fiber inputs and outputs as well as the integration of laser light sources with these same devices. The principal challenge in both of these pursuits is coupling light into the submicrometer waveguides that are the hallmark of silicon-on-insulator (SOI) systems. Previous work on grating couplers is leveraged to design new approaches to bridge the gap between the highly-integrated domain of silicon, the interconnected world of fiber and the active region of III-V materials.

First, a novel process for the planar packaging of grating couplers with fibers is explored in detail. This technology allows the creation of easy-to-use test platforms for laser integration and also stands on its own merits as an enabling technology for next-generation silicon photonics systems. The alignment tolerances of this process are shown to be well-suited to a passive alignment process and for wafer-scale assembly. Furthermore, this technology has already been used to package demonstrators for research partners and is included in the offerings of the ePIXfab silicon photonics foundry and as a design kit for PhoeniX Software's MaskEngineer product.

After this, a process for hybridly integrating a discrete edge-emitting laser with a silicon photonic circuit using near-vertical coupling is developed and characterized. The details of the various steps of the design process are given, including mechanical, thermal, optical and electrical steps. The interrelation of these design domains is also discussed. The construction process for a demonstrator is outlined, and measurements are presented of a series of single-wavelength Fabry-Pérot lasers along with a two-section laser tunable in the telecommunications C-band. The suitability and potential of this technology for mass manufacture is demonstrated, with further opportunities for improvement detailed and discussed in the conclusion.

Chapter 1

Introduction and Motivation



1.1 Context

In the 20th century, the invention of the laser and of low-loss fiber optics revolutionized the telecommunications world. The ability to transmit data using coherent light over long distances without the need for frequent signal regeneration opened new possibilities for interconnecting people. In a short time, the world was connected with a network of optical communication links, spanning both land and sea. With these new possibilities, new applications were dreamt of and realized. At the same time, more and more bandwidth was required to support these applications and the new users of these systems.

During this same period, the computer microprocessor was realized. This invention allowed data to be processed and created, and it provided a means for controlling the transmitters and receivers on the telecommunications network. The increasing mathematical computation power of the computer also aided in the design and improvement of the next generations of computing and telecommunications components, leading to the exponential growth of both. At the same time the computer was growing faster and more powerful, it was also growing smaller, until today a computer that fits in one's pocket possesses orders of magnitude more processing power and memory than a computer that 50 years ago would have taken up the area of an entire basketball court.

As these systems grow in power and at the same time grow smaller, certain bottlenecks are being reached. The computer processor, a traditionally electrical system, is reaching limits in the amount of data that can be transmitted on electrical wires. As the frequency of data modulation has approached the radio frequency (RF) regime, challenges of power loss, reflection and signal interference have arisen. Another related challenge is the management of heat and power consumption. Not only do leaky transistors waste power and generate heat, but lossy electrical transmission lines do as well. Furthermore, the large size of low-resistance electrical connectors when compared to fiber-optic cables, combined with their lower data rate, has posed a significant physical routing challenge in data centers and supercomputing facilities.

In telecommunications systems, when addressing the challenge of increased bandwidth requirements, there is significant benefit in reusing existing infrastructure such as already-laid fiber and current repeater stations. In this case, the goal is to increase bandwidth by squeezing more data into the current fiber, without relying on the improvements in fiber design and manufacture that have been made since the fiber was installed. Linked to this challenge is that of squeezing more equipment—or rather more functionality—in a single physical site with a fixed power supply. Going beyond meeting this infrastructure requirement, it is

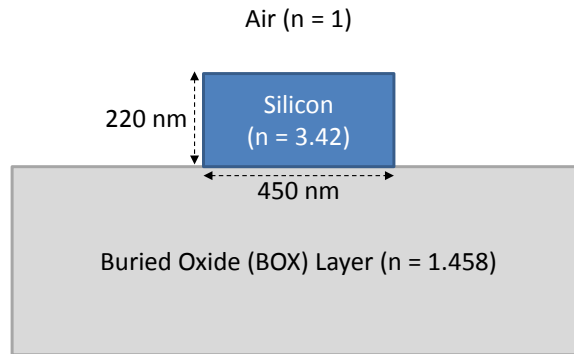


Figure 1.1: Cross-section of a sample silicon photonic waveguide

important to decrease power further so that more bandwidth can be achieved at a net reduction in energy consumption (lowered J/bit) in order to meet environmental sustainability goals.

1.2 Silicon Photonics

One technology looking to address these challenges is silicon photonics. At its core, silicon photonics operates on the same principle of guided light demonstrated by John Tyndall [1]. By this principle, a medium with an index of refraction n greater than the surrounding media will create a path for the propagation of light, analogous to the way a copper wire forms a path for an electrical signal. In traditional fiber optics, the difference of the so-called “core” and “cladding” indices is very small, around 0.36 % for single-mode fibers [2]. In contrast, the index of refraction of a silicon waveguide core is around 3.42 in the infrared [3], while the surrounding cladding index of refraction can be, e.g., approximately 1 for air or 1.458 for silica [4]. Fig. 1.1 shows a diagram of the cross-section of a typical “strip” geometry for a single-mode silicon waveguide etched on a silicon-on-insulator (SOI) wafer. Other geometries, such as a “ridge” or a “slotted” waveguide are possible as well.

This large contrast in index of refraction between the core and cladding results in the chief technical advantage of silicon photonics. It causes light to be highly confined in the waveguide and allows for the specification of submicrometer structures. It also allows for very tight bends with low losses, further reducing the size of a silicon photonic device. As an example, consider the devices shown in Fig. 1.2. Both devices are arrayed waveguide gratings (AWGs), a type of symmetric multiplexer and demultiplexer common in wavelength-division multiplexing (WDM) telecommunications systems. The one on the left is made in doped silica, a material system similar to a normal fiber optic cable. It occupies an area about the

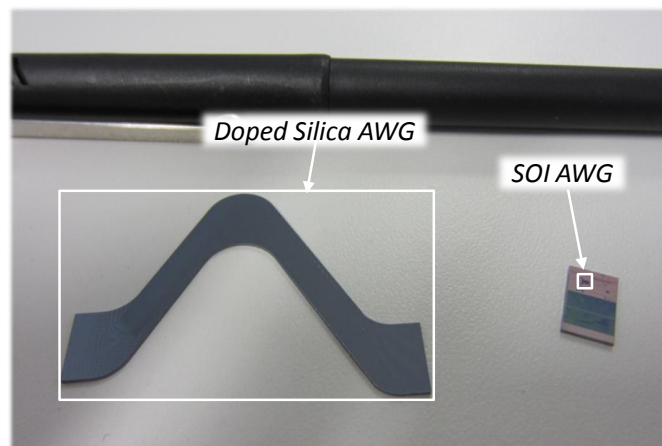


Figure 1.2: Doped-silica AWG and much smaller silicon AWG

size of a credit card. The device in the smaller box on the right is the larger of two AWGs on a single SOI chip containing about 40 different devices. It takes up approximately $1\text{ mm} \times 3\text{ mm}$ even though it uses an early unoptimized design.

The small size of silicon photonics also lends itself to applications outside of traditional computing and telecommunications. Tiny photonic chips or flexible silicon circuits can be sewn into clothes for wearable devices. While not fully biocompatible [5], silicon photonics can also be used as an important component in medical and sensing devices, whether used outside the body or implanted within. In these fields, the photonics capabilities of silicon can be integrated with the recent advances in microelectromechanical systems (MEMS) and microfluidics being developed on the same platform.

In realizing these various applications, a particular advantage of silicon photonics is that it is compatible with the complementary metal-oxide-semiconductor (CMOS) processes already widely in use in the production of computer processors. This means that in principle silicon photonics devices can be fabricated directly alongside CMOS logic circuits, which aids in the goal of replacing copper data lines in computers with photonic data lines or in the goal of making a compact fully-integrated telecommunications transceiver. Significantly, it also means that all the existing experience and economies-of-scale from CMOS manufacturing can be applied to silicon photonics production, whether or not it is closely integrated with CMOS logic.

This, in combination with the low cost of the base material, especially when compared to III-V materials systems like InP, means that silicon photonics can be manufactured in the billions of units at a very low cost. However, unlike in electronics where inexpensive packaging solutions have been developed and implemented, in photonics, packaging still constitutes a large percentage of the cost of production, often as much as 90% [6]. As a result, cost is a crucial factor to

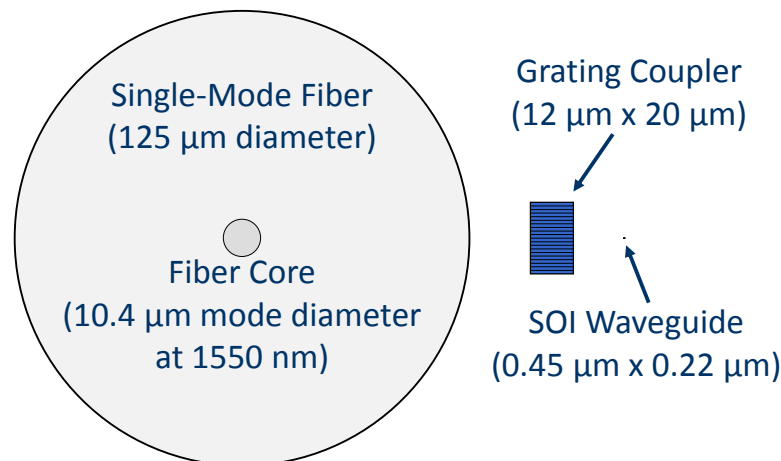


Figure 1.3: Diagram showing relative sizes of fiber and silicon photonic components (to scale)

consider in the design of any photonic packaging and integration technologies.

The main contributor to this cost is the very precise alignment tolerance required to ensure efficient operation of optical components. In particular, when alignment tolerances fall below the micrometer level, slow and expensive active alignment processes are required. In these processes, light is actually passed through the optical components of a system and measured. While the measurement is taking place, the components are moved in submicrometer steps to gauge and maximize the system efficiency. The light for this measurement can come from an external source or by driving a laser that is part of the system. In either case, optical or electrical sources need to be connected, often manually, to each system being packaged. This then introduces significant time and labor requirements that translate directly into additional cost.

If the alignment tolerance can be increased above a micrometer, then passive vision-based alignment can be used instead. This type of alignment can be applied at the wafer scale or in fast discrete chip manufacturing processes. The speed of this process depends largely on the magnitude of the alignment tolerance, as automatic alignment systems with positioning stages built to work with a repeatable precision of 5 μm or more operate with higher throughput than stages built for 1 μm precision. Finer precision also comes with an increase in the cost of the alignment systems themselves. Thus, even when passive alignment is possible, it is beneficial to relax alignment tolerances as much as possible.

Even better than both of these processes is self-alignment, where multiple components piece together in ways such that even submicrometer alignment can be achieved without the need for active measurement, high-precision motion stages or high-resolution imaging.

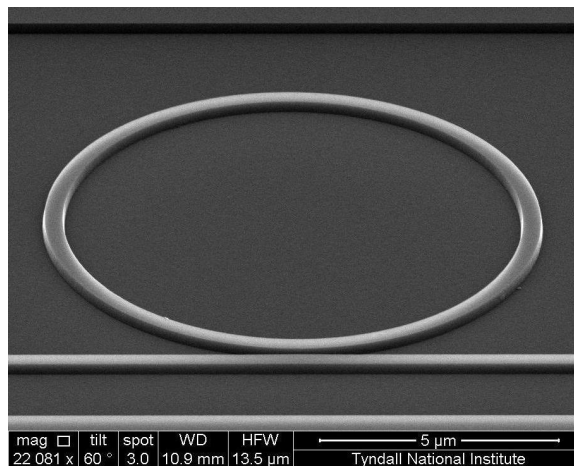


Figure 1.4: Angled scanning electron micrograph of silicon ring resonator optical filter

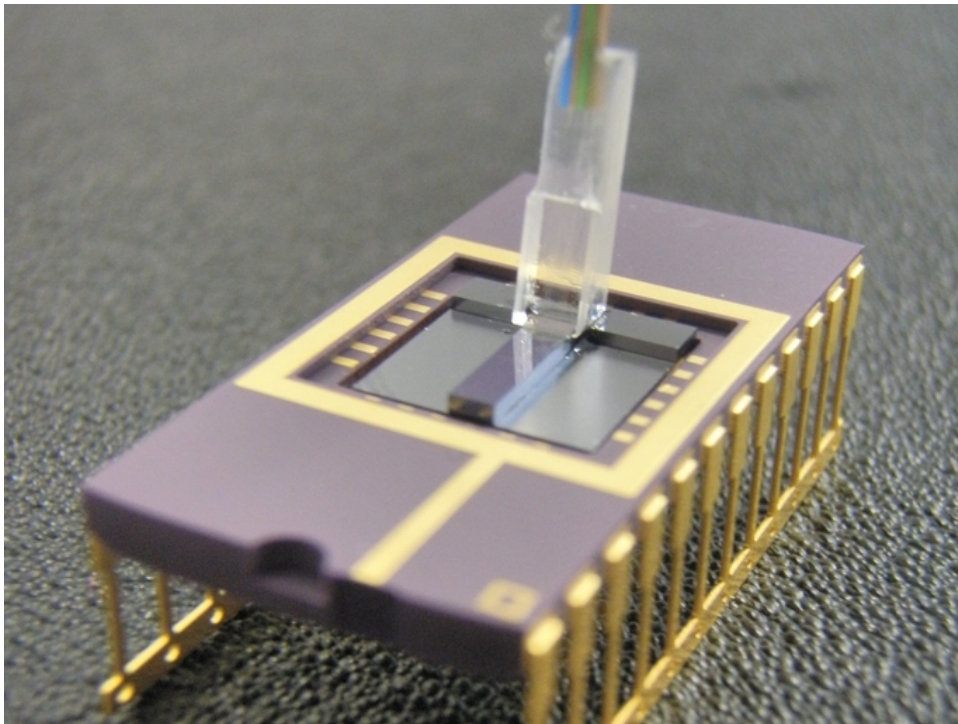
As mentioned before, one of the advantages of silicon photonics is its submicrometer size. This turns out to be a disadvantage when considering alignment tolerance and packaging. The size difference between silicon waveguides and standard components like single-mode fibers (Fig. 1.3) means that light cannot be directly coupled from one to the other without suffering significant power loss. Instead, a means for transitioning the size of the light mode (the spot size) in one device to its size in the other must be implemented. One way to do this is with a grating coupler, the size of which is also shown in the figure. This sort of structure has the potential to ease alignment tolerances to a level where passive alignment can be used, but it also poses its own challenges. For efficient operation, when these couplers are fabricated on a silicon chip they require input and output light to follow a path not completely vertical, but nearly vertical, to the chip surface. If the light path was oriented completely vertically, there would already be an approximately 3 dB (50 %) loss due to half of the light coupling in the opposite direction from that desired. So instead, incident angles of between 8° and 10° off-vertical are used. The challenge of satisfying this requirement while also maintaining a planar package form factor is one of the topics addressed in this thesis.

Another significant disadvantage of silicon photonics is that there has not been developed to this date an efficient electrically-pumped laser in silicon. Existing designs based on highly-doped strained germanium are still inefficient [7], and designs based on optical pumping are not amenable to monolithic integration [8]. This means that directly integrating a useful light source with the silicon photonic chip is not currently possible. However, there has been considerable research done to solve this problem through other, non-direct means of integration. This thesis describes one of these approaches that has been demonstrated successfully and found to be compatible with large-scale manufacturing.

This thesis is organized as follows. “Related Research” will provide a brief survey of ongoing research into the fiber packaging of silicon photonics as well as several methods of laser integration. It will also give a high-level description of the physics of the grating coupler technology chosen for use in the solutions presented herein. The “Fiber-Coupled Packaging” and “Fiber Array Packaging” chapters will then cover a novel planar fiber packaging technology as realized with single fibers and fiber arrays respectively. Following that, in “Design of Hybrid Integration Technology for Lasers,” the design process for integrated optical systems will be discussed along with the detailed example of a hybrid integration technology for active devices on SOI. “Implementation and Testing of Hybrid Integration Technology for Lasers” will show the realization of this design and measurements validating its compatibility with mass production. Finally, in “Conclusions and Further Work,” a road map for future research will be set out, and concluding perspectives will be given.

Chapter 2

Related Research



2.1 Introduction

As laid out in the previous chapter, the challenge of coupling light into silicon photonics devices arises chiefly due to the submicrometer size of the waveguides used. This applies both to packaging devices with fibers and to integrating devices with lasers. This chapter will cover previous and ongoing research aimed at addressing this challenge.

2.2 Fiber Coupling

In the realm of fiber coupling and packaging, several approaches to bridging the gap between a typical fiber mode size and a silicon waveguide mode size have been pursued. These approaches can be broadly placed into two categories based on the orientation of the optical path of the couplers and mode adapters used. The first category is end coupling, where the optical axis of the input and output ports is parallel to that of the silicon waveguide, and the second category is vertical coupling, where the optical axis of the couplers is nearly or completely perpendicular to the waveguide.

2.2.1 End-Coupling Techniques

In the category of end coupling, two major approaches have been pursued. The first involves using a lensed fiber to focus light directly to the small spot size of the silicon waveguide for input and then to refocus the diverging light exiting the silicon waveguide for output [9, 10]. Even when using thick SOI with 4 μm waveguides, the submicrometer alignment tolerance of lensed fibers is not suited to passive alignment. In addition, when epoxy is used as the fixing agent, the fiber is subject to drift on the order of the alignment tolerance, thus ruling out even an active-alignment-based process.

The other end-coupling technique involves adding a taper to the silicon waveguide itself [11–13]. Fig. 2.1 shows a schematic of such a structure. The silicon waveguide is surrounded by a larger waveguide consisting of polymer or another material such as SiON with an index of refraction lower than that of silicon. The silicon waveguide is then tapered to make it narrower, which decreases the confinement of the light in the waveguide, driving it out of the silicon waveguide and coupling it into the larger lower-index waveguide. A reciprocal process exists as well for input, where the light in the larger waveguide couples into the silicon waveguide as the latter waveguide grows wider. However, the demonstrated coupling waveguides are still quite small, ranging from 2 $\mu\text{m} \times 1 \mu\text{m}$ to 3 $\mu\text{m} \times 3 \mu\text{m}$. The resulting spot size of the larger

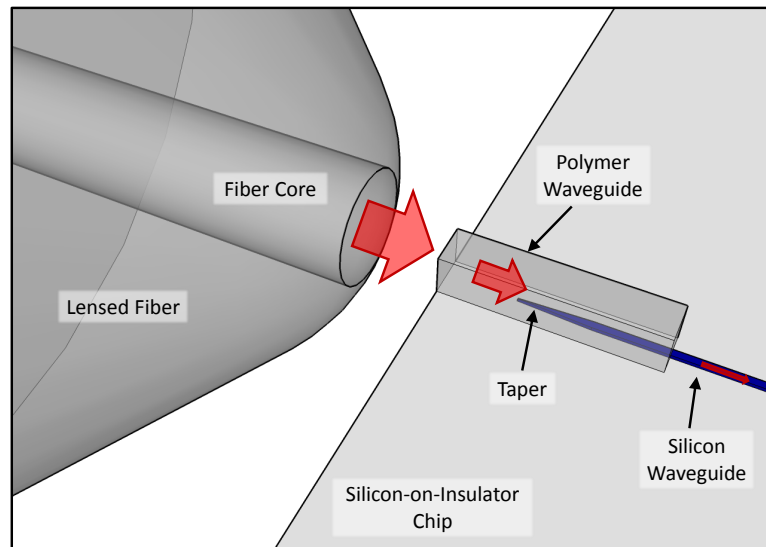


Figure 2.1: Schematic of inverse taper structure to couple light into a silicon waveguide

waveguide is then still much smaller than that of a standard single-mode fiber, and so the use of lensed fibers or a separate external taper to match the fiber mode is still required. In either case, the resulting 1 dB alignment tolerance is less than $1\ \mu\text{m}$. An additional restraint lies in the fact that the efficiency of the coupling with the inverse taper is dependent on wavelength, though the wavelength dependence is significantly less than for grating couplers.

2.2.2 Near-Vertical Coupling

2.2.2.1 Grating Coupler Theory

Another approach to coupling light into silicon waveguides uses planar diffraction gratings to couple light from a near-vertical incidence to the submicrometer silicon waveguide. The concept of a grating coupler has been known for decades. It relies on a periodic structure in a waveguide to change the direction and magnitude of the wavevector of a beam of light.

Consider a beam of light with a vacuum wavevector k_0 incident on a grating coupler. The well-known phenomena of reflection and refraction occur. These are familiar to anyone who has seen trees reflected in a stream or reached into the same stream to catch a fish only to find that it was not where it appeared to be. The physical property governing this behavior is the matching of the phase fronts at the interface of two media. Quantitatively, this means that the components of the wavevectors parallel to the interface, in this case k_y , must be equal on either side. On the other hand, the components of the wavevectors perpendicular to the interface,

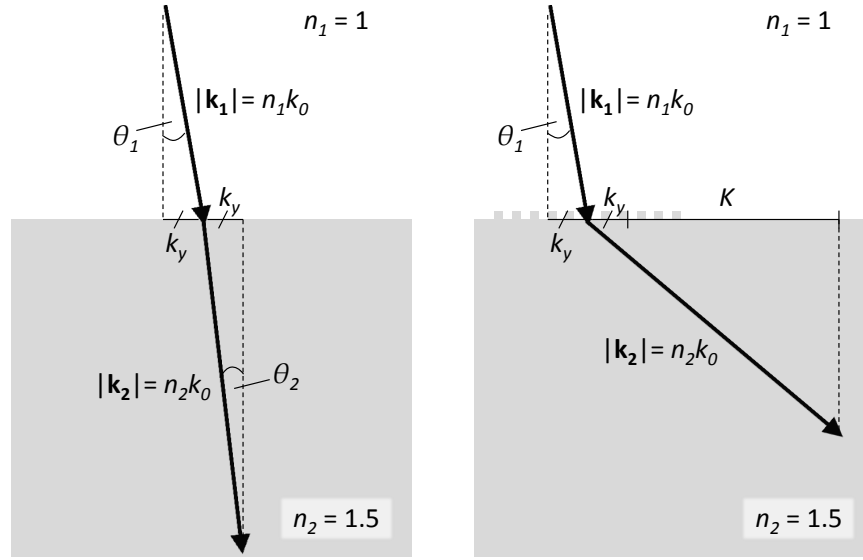


Figure 2.2: Wavevectors of light refracted (left) and diffracted (right) showing matching of the parallel components

k_z , can and do change. The total magnitude of the wavevector \mathbf{k} is dependent on the index of refraction of the medium according to

$$|\mathbf{k}| = nk_0 = \frac{n2\pi}{\lambda_0} \quad (2.1)$$

where n is the index of refraction of the medium and λ_0 is the wavelength of the light in vacuum. The combination of the matched parallel components and varying perpendicular components form the underpinnings of Snell's Law, where the angle of the wavevector with parallel component k_y and total magnitude $|\mathbf{k}|$ determines the direction of beam propagation. This is shown graphically on the left in Fig. 2.2.

When there is a grating between two of the media, this is taken one step further with the phenomenon of diffraction [14]. Instead of the parallel components being strictly equal, diffracted beams can have wavevectors with parallel components from a set of well-defined values. These values are determined by the pitch of the grating. For a given pitch Λ , a value K is defined as follows.

$$K = \frac{2\pi}{\Lambda} \quad (2.2)$$

Then, the allowed parallel wavevector components are given by

$$k_i = k_y + iK \quad (2.3)$$

where i is a positive or negative integer, and reflection and refraction are simply the

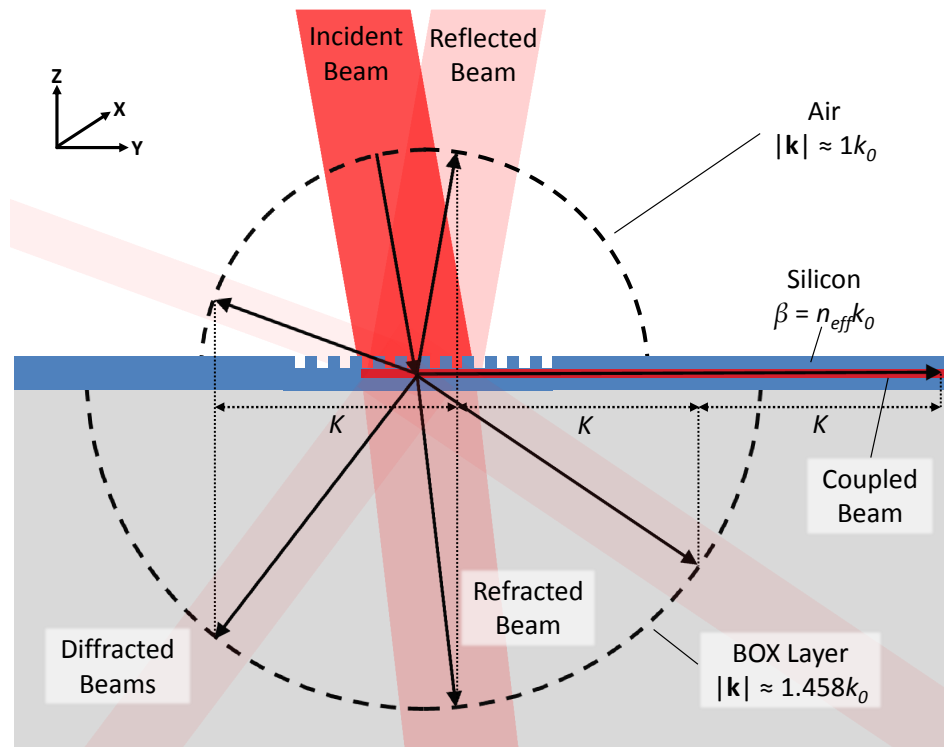


Figure 2.3: Schematic showing the wavevectors of reflected, refracted and diffracted beams upon incidence with a grating coupler

case where $i = 0$. For all other cases, where k_i does not exceed the total magnitude of \mathbf{k} for the light in one of the media, a diffracted beam occurs. This effect is shown in the right side of Fig. 2.2.

In the case of a grating coupler (Fig. 2.3), the pitch is set so that one or more of these possible diffracted beams are directed into the guiding medium. In addition, to ensure efficient coupling to a guided mode, the value of k_i should match a value of β , the longitudinal component of the wavevector for the waveguide mode (Fig. 2.4). This value is in turn related to the effective index of the mode by the following relationship

$$\beta = n_{eff}k_0 \quad (2.4)$$

If this value is not perfectly matched, coupling will still occur for sufficiently close values, but the efficiency will be diminished due to phase mismatch between the profile of the diffracted beam and the guided mode. This same effect leads to a wavelength-dependent behavior of the grating that will be discussed and quantified shortly. It should also be noted that because of the high index of refraction of silicon, and the resultant large β values of SOI waveguide modes compared to the incident wavevector, a higher-order diffraction such as $i = 3$ is typically used to

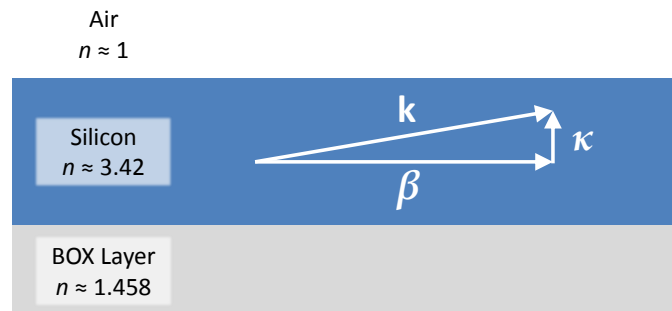


Figure 2.4: Components of the wavevector of a guided mode

couple into the waveguide.

In practice, this sort of direct analysis is not used to design gratings. Instead, numerical methods such as implemented in the free software package CAMFR [15] are used and can be easily applied to a wide variety of geometries, including gratings with varying pitch or angled (blazed) ridges. CAMFR uses a technique called “eigenmode expansion,” whereby the guided and radiation modes of each section (e.g., shallow-etched section, unetched section) of the grating structure are calculated, with perfectly-matched layers (PML) used as boundary conditions above and below the grating [16]. The resulting modes can then be used to calculate the field anywhere in the grating structure. This and other numerical methods allow for the determination of the coupling efficiency to the various diffracted orders and to other mode profiles such as that of an optical fiber, a capability which is especially important when using a grating for optical coupling.

2.2.2.2 Recent Grating Coupler Research

Early grating coupler designs [17] that were fabricated and tested in SOI used straight ridges partially etched into a wide silicon section (Fig. 2.5) to reduce the spot size of the light in the vertical axis, then followed the grating with a long adiabatic taper section to focus the spot in the horizontal axis (Fig. 2.6). These designs provide a peak coupling efficiency of around 30% per grating, with the coupling efficiency varying significantly with the wavelength of the incident light. Fig. 2.7 illustrates how much the insertion loss can vary. This graph shows the combined effect of both an input and output grating, so the 3 dB bandwidth for a single one of these gratings is only 50 nm. Despite this, grating couplers provide a key advantage over other technologies due to their relaxed alignment tolerance, with less than 1 dB misalignment penalty over an approximately 5 μm range. This in turn facilitates passive alignment and wafer-scale assembly.

Improving on early designs with the introduction of bottom reflectors [18, 19] and apodized ridge spacing [20] has resulted in significant increases in coupling

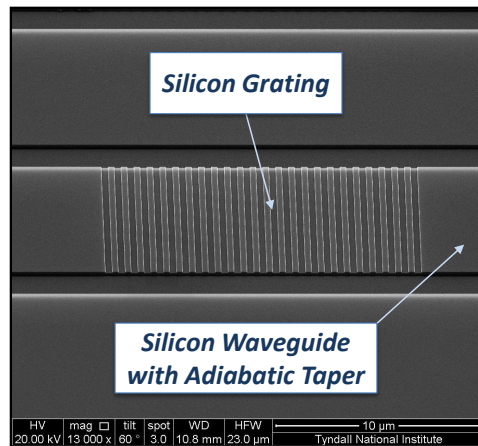


Figure 2.5: Angled scanning electron micrograph of grating coupler

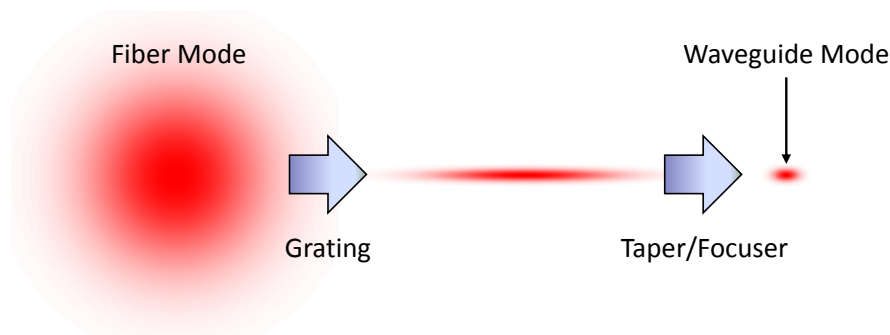


Figure 2.6: Steps to reduce spot size using a grating coupler showing cross-section of spot at each stage (not to scale)

efficiency, with peak coupling efficiencies reaching as high as -0.75 dB [21]. At the same time, novel etch geometries are expected to expand the 1 dB bandwidth of the coupling spectrum to as much as 180 nm [22]. Finally, the widespread use of curved “focusing” gratings has removed the requirement for long taper sections [23].

Another characteristic of these gratings is that they only work for a single polarization. In some cases, this can be useful, as when polarization filtering or a known output polarization is desired. On the other hand, in applications like polarization-division multiplexing where preserving both orthogonal polarizations is important, a 2D grating must be used. The design of this type of grating replaces the 1D array of grating lines with a 2D array of grating holes. Such gratings have been demonstrated with up to -2.7 dB peak coupling efficiency [21].

While grating couplers provide a convenient way to bridge the gap between silicon waveguides and standard single-mode fiber, and a convenient means for wafer-scale testing, at the same time they pose significant challenges for packaging. A fiber in a ferrule or V-groove assembly can be aligned directly at the input angle for the grating coupler [24–27] (as seen on the cover of this chapter), but this technique results in a package that is both bulky and fragile, and also obstructs a significant

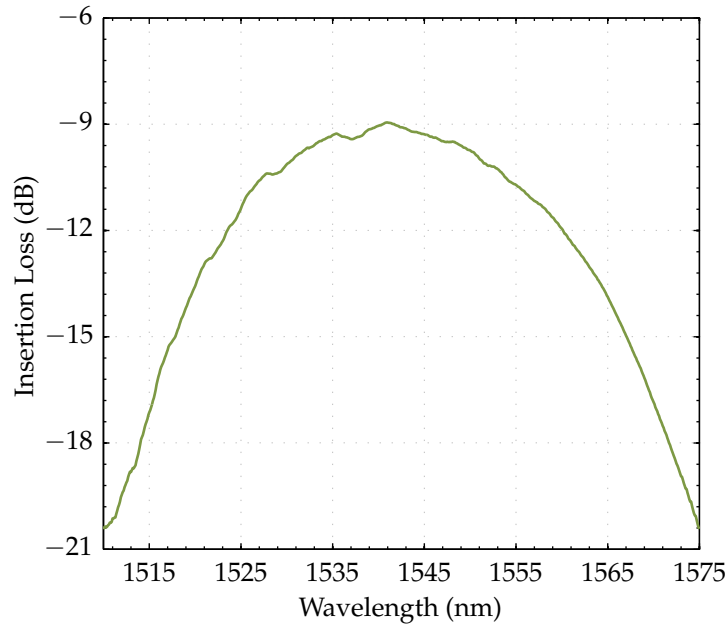


Figure 2.7: Measured fiber-to-fiber optical insertion loss of grating-coupled straight waveguide showing significant variation with wavelength

area of the chip surface. This obstruction prevents valuable chip real estate from being used for electrical connections, microheaters and other functional enhancements.

2.2.3 Fiber Arrays

It is desirable to be able to package photonic integrated circuits not just with single fibers, but also with dense arrays of fibers, especially for devices such as splitters, multiplexers and demultiplexers. One technique for doing this is to use V-groove assemblies as described in the previous section. However, with these V-grooves, the pitch is generally limited to the standard values of $127\ \mu\text{m}$ or $250\ \mu\text{m}$. Even with a custom array, the pitch cannot be less than $125.7\ \mu\text{m}$ when using standard single-mode fibers [2]. In addition, the number of fibers in a given array is limited by the rotational alignment tolerance. For example, considering an array of 32 fibers at a pitch of $127\ \mu\text{m}$, the first and last fiber cores have a separation of $3.937\ \text{mm}$. Assuming the first fiber is perfectly aligned, a rotational misalignment in the roll axis of only 0.04° results in the last fiber core being shifted by a full $5.5\ \mu\text{m}$ from its ideal position per the following geometric relationship,

$$2\ell \sin \frac{\theta}{2} \quad (2.5)$$

where ℓ is the distance between the first and last fiber cores and θ is the angle of

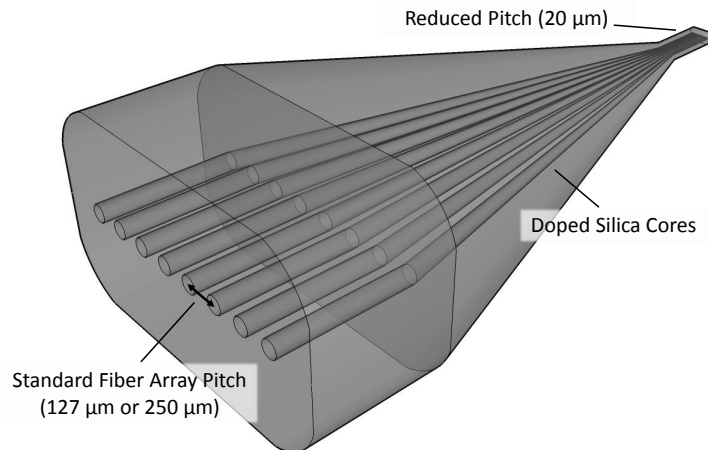


Figure 2.8: Schematic of pitch-reducing fiber array (PROFA) used for fiber end-coupling

rotation of the fiber array.

Another approach to multi-fiber packaging is to use pitch-reducing fiber arrays (PROFAs) (Fig. 2.8) combined with inverse tapered waveguides [13, 28]. The PROFA is built by heating a specialized glass preform and drawing it in a controlled fashion to create a tapered structure. This tapered structure contains several guided cores. These cores are situated at a standard fiber array pitch at the large end of the taper, but at a much lower pitch at the smaller end. In this way, an array of fibers at a pitch of $250\ \mu\text{m}$ can be coupled to an array of waveguides at a much denser pitch of $20\ \mu\text{m}$. This approach also allows for polarization diversity and has losses lower than 1 dB between the tapered end of the array and the silicon waveguide. However, the alignment tolerances are comparable to lensed fibers, with submicron accuracy required for less than 1 dB loss in both the lateral axes and the optical axis. Furthermore, there is an insertion loss of 3 dB through the PROFA itself.

2.3 Laser Integration

Currently, there are two approaches being undertaken to integrate lasers with silicon photonic waveguides. The first approach, so-called heterogeneous integration, involves the attachment of a III-V gain medium to a silicon chip or wafer, either directly onto a silica passivation layer or with an intermediate polymer (BCB) layer. The III-V layer is then patterned and etched to form a laser, with the coupling of light between the active medium and the silicon layer done evanescently. The cavity of the laser can either be formed by a ring in the III-V [29, 30], or by etching grating-based reflectors in the III-V [31] or silicon [32] layer, or by using a

distributed feedback resonator [33]. The III-V dies can be placed individually, or efficiently in groups at the wafer scale using a transfer printing method [34].

The other approach is referred to as hybrid integration and consists of integrating a discrete finished laser diode chip with a silicon photonic waveguide. In the case of thick SOI ($3\ \mu\text{m}$ – $4\ \mu\text{m}$), direct end-coupling can be used. In one implementation, a flip-chip process with an accuracy of $\pm 1\ \mu\text{m}$ is used to horizontally align and bond the laser die active-side-down by thermocompression [35]. The laser output facet is placed within $5\ \mu\text{m}$ of an etched and AR-coated input facet in the thick SOI. The vertical alignment of the laser is controlled by the etch depth and the thickness of the deposited metal of the bond pad, with a very high accuracy of $\pm 100\ \text{nm}$. The advantages of this end-coupling method are simplicity and lack of additional focusing optics, resulting in a reasonable coupling efficiency of $-2.7\ \text{dB}$.

Other implementations using thick SOI involve coupling a discrete semiconductor optical amplifier (SOA) in III-V to the silicon waveguides. In these cases, one of the laser cavity reflectors is formed by a Bragg grating etched in an SOI ridge waveguide. Bookham Technology reported coupling efficiency of better than 50% along with a self-alignment scheme yielding alignment tolerances better than $0.5\ \mu\text{m}$ [36], while Kotura reported a coupling efficiency as high as 2 dB relying on active alignment with the future prospect of flip-chip integration [37]. Still, reflections remain an issue with these end-coupling techniques, and it is not possible to place an optical isolator between the laser output and SOI photonic circuit.

For thin SOI ($0.22\ \mu\text{m}$), directly coupling to an SOI waveguide will not result in efficient coupling. Instead, a different approach must be taken. As in the case of fiber packaging, either end-coupling to an inverse taper [38] or else near-vertical coupling to a planar grating [39] can be used. The end-coupling can be implemented in a similar fashion to what is done with thick SOI, where in this case the larger low-index waveguide is comparable in size to the thick SOI layer. However, the use of some polymers for the low-index waveguide may not be compatible with thermocompression bonding depending on the heat tolerance of the chosen material, and so a different method of bonding and controlling vertical alignment may be required.

On the other hand, with near-vertical coupling, the laser die does not have to be bonded to the chip surface and associated optics can be removed from the chip surface as well. As a result, the space that would otherwise be dedicated to bond pads or mounting trenches for optics can be freed up and used for other photonic circuit elements. The additional space and flexibility afforded by taking the laser and optics off the chip also allows for the penalty-free addition of space-consuming functional enhancements such as a discrete optical isolator.

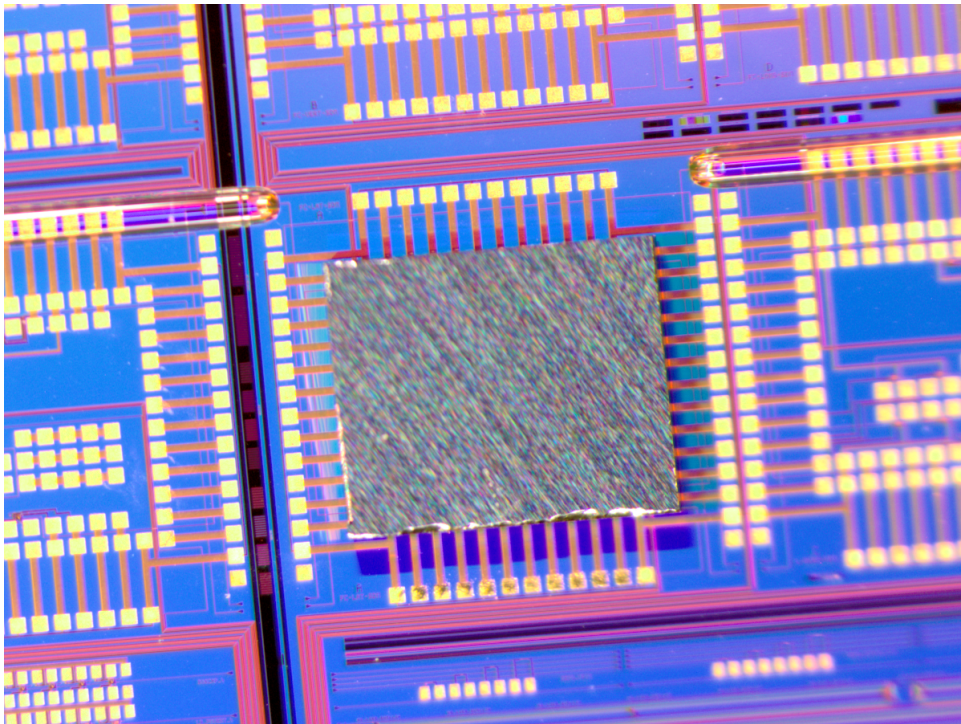
Contemporaneous to this research, Luxtera has developed an integration technology

for edge-emitting lasers using near-vertical coupling based on a silicon micro-optical bench [21]. This technology uses a passive-aligned reflector, is not compatible with high-speed direct modulation and requires active alignment during the integration of the micro-optical bench with the SOI chip [40].

This thesis will focus on the development of a novel technology for integrating lasers using a high-speed ceramic micro-optical bench. First, an original process for the planar packaging of grating couplers with fibers will be explored in detail. This technology allows the creation of easy-to-use test platforms for laser integration and also stands on its own merits as an enabling technology for next-generation silicon photonics systems. After this, a process for hybrid-integrating a discrete edge-emitting laser with a silicon photonic circuit using near-vertical coupling will be developed and characterized. The suitability and potential of this technology for mass manufacture will be demonstrated, with further opportunities for improvement detailed and discussed in the conclusion.

Chapter 3

Fiber-Coupled Packaging



3.1 Introduction

As described in the last chapter, previous packaging processes using grating couplers have relied on orienting a fiber or fiber block directly at a 10° angle [39, 41, 42]. However, it is desirable to maintain a planar profile so as to decrease the overall size of the package. Existing non-planar designs are bulky and fragile. They also result in the obstruction of a large amount of the chip surface, preventing it from being used for electrical connections, microheaters and other functional enhancements. This chapter outlines a new planar packaging process. This new process uses a standard cylindrical fiber with an end facet polished at an angle so as to reflect light from the fiber core to the required input angle of the grating coupler and *vice versa* for output couplers.

This chapter is organized as follows. First, the theory of the packaging process is outlined and simulations of alignment tolerances are presented. Then, physical measurements of alignment tolerance and coupling efficiency are presented. Finally, conclusions and future directions for the packaging process are discussed.

3.2 Theory

3.2.1 Physical Principle

Fig. 3.1 shows a schematic view of the path of the light as it passes through the fiber, reflects off the fiber facet and is coupled into the waveguide by the grating coupler. While this figure shows the light in the input direction, a reciprocal operation exists for output light. A ray optics analysis can be used to determine the necessary polish angle for the fiber that will reflect the light to the proper angle for the grating coupler. This angle is given by the following relationship

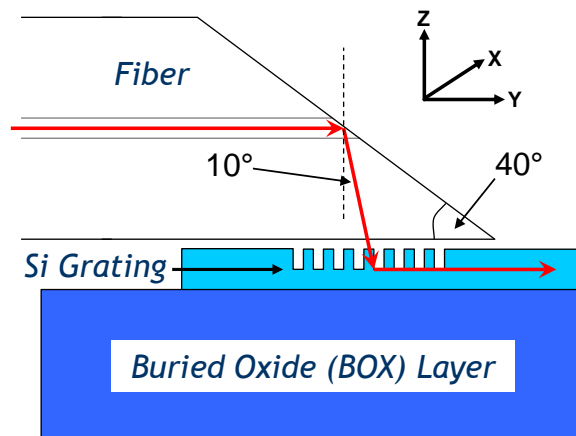


Figure 3.1: Schematic of light path in angle-polished fiber

$$\theta_{fiber} = \frac{90^\circ - \theta_{off-vertical}}{2} \quad (3.1)$$

For a grating coupler with a design angle of 10° , the relationship yields a polish angle of 40° . Furthermore, the well-known relationship in (3.2) defining the critical angle θ_c for total-internal reflection (TIR) shows that TIR occurs at this angle, and thus an additional reflective coating on the fiber end face is not necessary.

$$\sin \theta_c = \frac{n_{air}}{n_{fiber}} \Rightarrow \theta_c = 42.930^\circ < (90^\circ - \theta_{fiber}) \quad (3.2)$$

This relationship also shows the limit of angles that can be used without the need to add a reflective coating to the fiber facet. So for instance, an 8° grating coupler could be used as well with a fiber polish angle of 41° . In fact, a fiber polish angle up to 47° with corresponding grating input angle of -4° (i.e. principal coupling backward) will still result in TIR. Furthermore, at both the standard angles of 8° and 10° , there is a comfortable margin of error for TIR.

The total internal reflection that occurs at the facet is also accompanied by a polarization-dependent phase shift. For light with electric field polarized in the X-direction, the phase shift φ_x is given by (3.3), whereas (3.4) gives the phase shift φ_z for light with electric field polarized in the Z-direction [43]. In both of these, θ_i is the incident angle of light with respect to the normal of the polished facet and θ_c is the critical angle for total internal reflection calculated in (3.2).

$$\tan \frac{\varphi_x}{2} = \frac{\sqrt{\sin^2 \theta_i - \sin^2 \theta_c}}{\cos \theta_i} \quad (3.3)$$

$$\tan \frac{\varphi_z}{2} = \frac{\sqrt{\sin^2 \theta_i - \sin^2 \theta_c}}{\cos \theta_i \sin^2 \theta_c} \quad (3.4)$$

With a 40° facet polish, this results in phase shifts of 0.31789π for X-polarization and 0.55131π for Z-polarization. In the case of a 1D grating coupler, this discrepancy does not matter as the X-polarization is the only polarization coupled by the grating. However, in the case of a 2D grating coupler this does make a difference. In a 2D grating coupler, the 1D array of ridges is replaced with a 2D array of holes. This structure couples light into one of two arms depending on the polarization of the electric field of the light. The polarization needed to couple into each arm, referred to hereafter as the target polarization, is linear and diagonal at 45° clockwise or counterclockwise about the optical axis. If the polarization in the fiber matches this directly, the resulting reflected polarization will be elliptical rather than diagonal. Jones calculus can be applied to understand analytically what happens to these

polarizations. For this analysis, Z will be taken to be the optical axis of the grating, in the vertical direction, rather than the optical axis of the fiber, which lies in the horizontal direction (Fig. 3.1). Then, the two diagonal polarizations as they propagate in the fiber can be expressed in the X-Z basis by two Jones vectors \mathbf{v}_1 and \mathbf{v}_2 , where

$$\mathbf{v}_1 = \frac{\sqrt{2}}{2} \begin{bmatrix} 1 \\ 1 \end{bmatrix}, \mathbf{v}_2 = \frac{\sqrt{2}}{2} \begin{bmatrix} -1 \\ 1 \end{bmatrix}. \quad (3.5)$$

Next, a set of Jones matrices can be used to find the coupling for a given input polarization to the target polarization of each 2D grating coupler arm.

$$\mathbf{M}_1 = \frac{1}{2} \begin{bmatrix} 1 & 1 \\ 1 & 1 \end{bmatrix} \begin{bmatrix} e^{i\varphi_x} & 0 \\ 0 & e^{i\varphi_z} \end{bmatrix} = \frac{1}{2} \begin{bmatrix} e^{i\varphi_x} & e^{i\varphi_z} \\ e^{i\varphi_x} & e^{i\varphi_z} \end{bmatrix} \quad (3.6)$$

$$\mathbf{M}_2 = \frac{1}{2} \begin{bmatrix} 1 & -1 \\ -1 & 1 \end{bmatrix} \begin{bmatrix} e^{i\varphi_x} & 0 \\ 0 & e^{i\varphi_z} \end{bmatrix} = \frac{1}{2} \begin{bmatrix} e^{i\varphi_x} & -e^{i\varphi_z} \\ -e^{i\varphi_x} & e^{i\varphi_z} \end{bmatrix} \quad (3.7)$$

In the calculation of these matrices, first a phase shift is applied for each of the X and Z components of the light and then the result is projected onto the desired grating target polarization. By multiplying these matrices by an input vector and taking the norm, the amount of field that is coupled to the target polarization can be determined.

$$|\mathbf{M}_1 \mathbf{v}_1| = \left| \frac{\sqrt{2}}{4} \begin{bmatrix} e^{i\varphi_x} + e^{i\varphi_z} \\ e^{i\varphi_x} + e^{i\varphi_z} \end{bmatrix} \right| = \frac{\sqrt{2}}{2} \sqrt{1 + \cos(\varphi_z - \varphi_x)} \quad (3.8)$$

$$|\mathbf{M}_1 \mathbf{v}_2| = \left| \frac{\sqrt{2}}{4} \begin{bmatrix} -e^{i\varphi_x} + e^{i\varphi_z} \\ -e^{i\varphi_x} + e^{i\varphi_z} \end{bmatrix} \right| = \frac{\sqrt{2}}{2} \sqrt{1 - \cos(\varphi_z - \varphi_x)} \quad (3.9)$$

When the fiber input polarization matches the grating polarization, 93.3% of the incident field magnitude is coupled into the grating polarization. This decrease in field represents a 13% or 0.6 dB penalty to the transmitted power. Furthermore, this results in 0.6 dB of crosstalk to the other grating arm, as the power lost in one polarization is coupled into the orthogonal polarization. One can also determine the accumulated phase shift in the grating polarization that results from the reflection by rewriting $\mathbf{M}_1 \mathbf{v}_1$ as

$$\frac{\sqrt{2}}{2} \cos \frac{\varphi_x - \varphi_z}{2} \begin{bmatrix} 1 \\ 1 \end{bmatrix} e^{i \frac{\varphi_x + \varphi_z}{2}} \quad (3.10)$$

and reading the phase term of $\frac{\varphi_x + \varphi_z}{2}$ directly.

It is desirable then to find a set of polarizations in the fiber that will be reflected completely into the grating polarizations and also exhibit no crosstalk. These polarizations can be found by solving the following system of equations

$$\begin{cases} \mathbf{M}_1 \mathbf{v}_{e1} = \frac{\sqrt{2}}{2} \begin{bmatrix} 1 \\ 1 \end{bmatrix} \\ \mathbf{M}_1 \mathbf{v}_{e2} = \begin{bmatrix} 0 \\ 0 \end{bmatrix} \\ \mathbf{M}_2 \mathbf{v}_{e1} = \begin{bmatrix} 0 \\ 0 \end{bmatrix} \\ \mathbf{M}_2 \mathbf{v}_{e2} = \frac{\sqrt{2}}{2} \begin{bmatrix} -1 \\ 1 \end{bmatrix} \end{cases} \quad (3.11)$$

where \mathbf{v}_{e1} and \mathbf{v}_{e2} will be the new elliptical polarizations in the fiber for maximum coupling and minimum crosstalk to the 2D grating. The solution of this system is straightforward in light of what is known about the compositions of \mathbf{M}_1 and \mathbf{M}_2 , and the results are the following Jones vectors,

$$\mathbf{v}_{e1} = \frac{\sqrt{2}}{2} \begin{bmatrix} 1 \\ e^{-i(\varphi_z - \varphi_x)} \end{bmatrix}, \mathbf{v}_{e2} = \frac{\sqrt{2}}{2} \begin{bmatrix} -1 \\ e^{-i(\varphi_z - \varphi_x)} \end{bmatrix}. \quad (3.12)$$

It should also be noted that these polarizations are orthogonal per the inner product in (3.13). This means that they are still suitable for polarization-division multiplexing (PDM) data encoding schemes. Beyond PDM, the understanding and quantification of these polarization changes is important in fiber sensing systems, where the sensing mechanism may rely partially or completely on determining the polarization in the fiber based on the outputs of the two arms of the 2D grating coupler.

$$\langle \mathbf{v}_{e1}, \mathbf{v}_{e2} \rangle = 0 \quad (3.13)$$

In addition to the concerns of polarization, the TIR relationship in (3.2) only holds true so long as the fiber facet is surrounded by air. Any contamination of the end facet with bonding epoxy or other non-reflective substances significantly reduces the reflectivity of the facet. The requirement to avoid contamination then presents a significant challenge when fixing the fiber in place.

To solve this issue, the fiber is affixed to the chip with 0.5 μL of low-viscosity (300 cP) ultraviolet (UV) cure epoxy applied at least 2 mm from the fiber end facet.

The uncured epoxy spreads through capillary action along the gap between the fiber cladding and the SOI chip surface. Critically, due to the capillary effect the spreading stops immediately at the end of the fiber and does not contaminate the polished facet (Fig. 3.5). At this point, the epoxy can be cured and TIR is maintained.

3.2.2 Calculation of Alignment Tolerances

The Physical Optics Propagation feature of the commercial software Zemax was used to simulate the alignment tolerances of the fiber to the grating. This feature models the propagation of Gaussian and arbitrary modes through a sequential optical system, taking into account various material properties such as index of refraction, absorption and birefringence. There is also limited support for reflections, as well as support for simulating the effects of reflective, antireflective and beam-splitting coatings. In addition, Zemax supports a basic macro language for automation of simulations. Zemax also contains a sophisticated ray tracing feature that can be used to simulate highly-multi-mode systems or systems where modal behavior is not significant, and this feature can be used with arbitrary non-sequential systems as well.

A model was constructed to simulate the divergence of the light as it passes through the cladding of the fiber and the lensing effect of the cladding in air and finally the coupling of the light into the design mode of the grating coupler. The lens data for this model is shown in Table 3.1. FIBER_CLAD.ZTG specified a custom glass file containing data for the cladding material of a fiber possessing an index of refraction of 1.4682 at a light wavelength of 1.55 μm . The core of the fiber was neglected, as the index of refraction difference between the core and cladding was only 0.36 % [2]. The coupling efficiency was determined using the well-known mode-coupling equation,

$$\eta = \frac{[\iint F(x,y)E^*(x,y) dx dy]^2}{\iint F(x,y)F^*(x,y) dx dy \iint E(x,y)E^*(x,y) dx dy} \quad (3.14)$$

where $F(x,y)$ and $E(x,y)$ represent the fields of the grating input mode and incident light respectively. These functions are complex in value, so the overlap of the magnitude as well as the matching of the phase were taken into account.

The grating coupler input mode was chosen to be that of a single-mode fiber tilted at 10°. This mode was chosen because it is the target mode for various grating coupler designs, and thus separates the details of the packaging process from the details of the grating coupler design process, treating the grating coupler itself as a black box. Similarly, the various grating designs treat the packaging process as a black box and optimize to the aforementioned target mode. An exact mode for an individual grating, with its particular divergences from the ideal target mode, could

Table 3.1: Zemax Lens Data for Fiber Coupling

Surface	Type	Radius	Thickness	Glass	Aperture	Tilt/Decenter	Description
0	Standard	Infinity	1 μm	FIBER_CLAD.ZTG			Custom Glass For Core/Cladding
1	Coordinate Break		0			-50° Tilt About X	Set up Angled Reflector
2	Standard	Infinity	0	MIRROR	62.5 μm Semi-Diameter		Polished Facet
3	Coordinate Break		-61.5 μm			-40° Tilt About X	Finish up Angled Reflector
4	Biconic	Y: Infinity X: 62.5 μm	-2 μm		62.5 μm Semi-Diameter		Edge of Cladding
5	Coordinate Break		0				Used for Alignment Tolerance
6	Standard	Infinity			20 μm Semi-Diameter	-10° Tilt About X Before Surface	Grating Coupler Surface

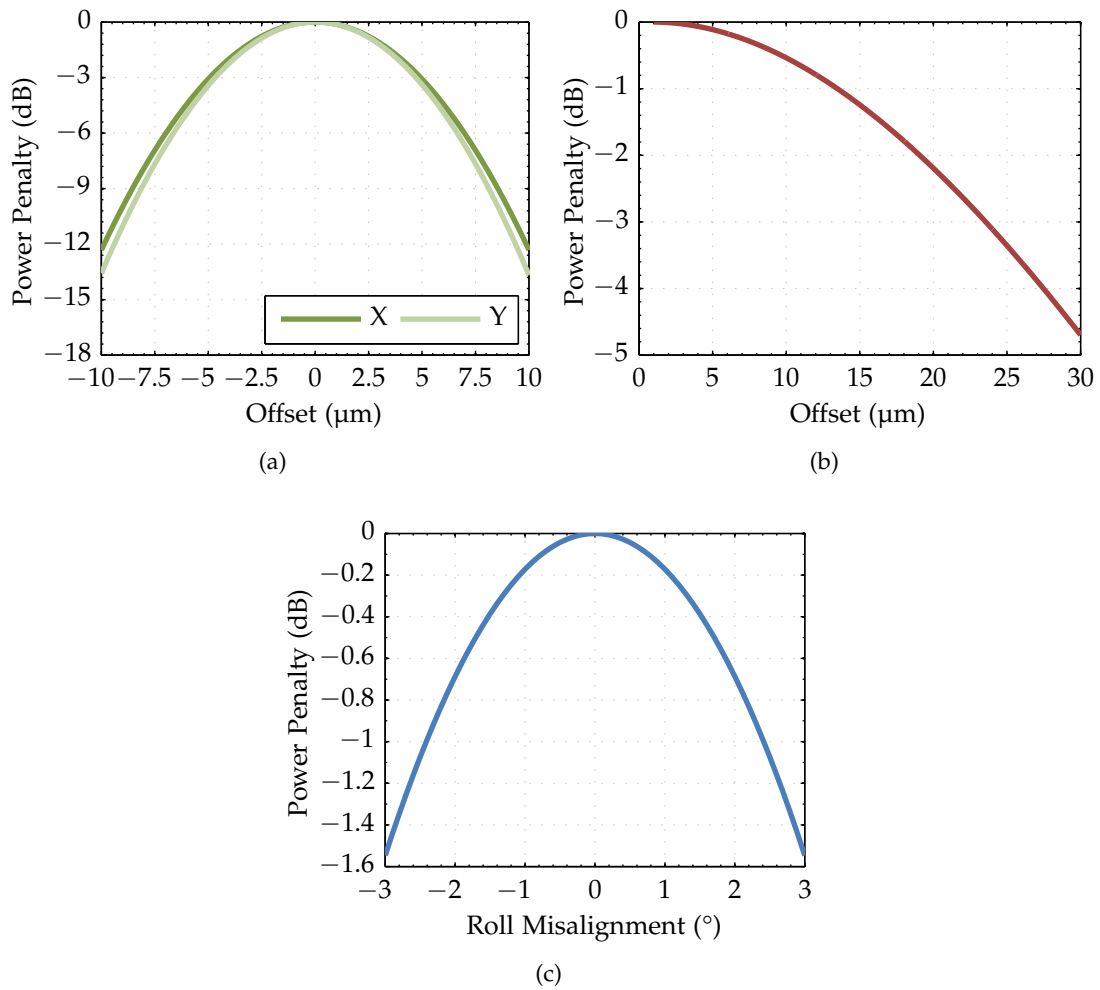


Figure 3.2: Simulated alignment tolerances: (a) Along and across the plane of the grating (b) Working distance from fiber cladding base to grating surface (c) Roll of fiber along fiber axis

have been chosen, but then this would require resimulation and reoptimization for each individual grating design.

The results for simulation of the alignment tolerances are shown in Fig. 3.2. Of these, Fig. 3.2a shows the power penalty of misalignment parallel to the plane of the grating coupler. It was determined that there is less than 1 dB additional loss due to misalignment over a $5.6 \mu\text{m}$ range in the X direction and a $5.2 \mu\text{m}$ range in the Y direction. Fig. 3.2b shows simulation results for the working distance of the fiber, i.e. the distance between the lower surface of the cladding and the grating itself. These results show that the fiber can be up to $13.5 \mu\text{m}$ away from the grating coupler and still suffer less than 1 dB additional loss. This tolerance is important for the packaging process because it ensures that the thickness of the epoxy bond will not be a critical factor. Finally, Fig. 3.2c shows that the tolerance of the fiber roll on its axis is $\pm 2.5^\circ$ for less than 1 dB additional loss.

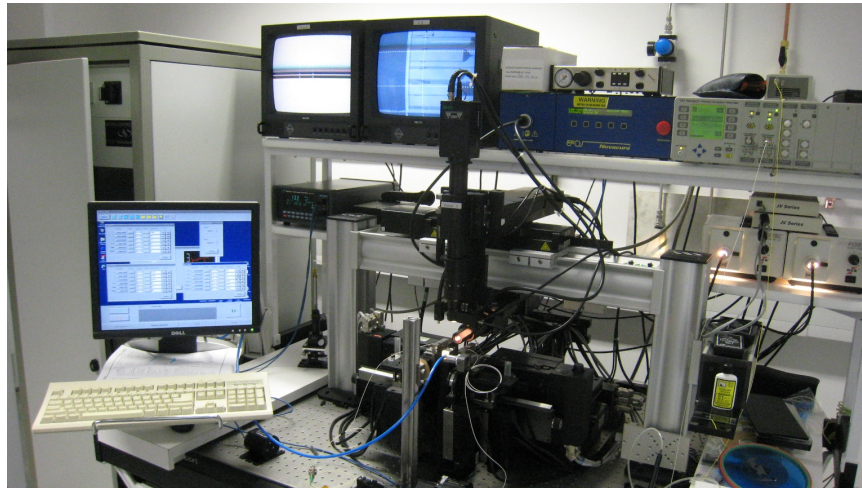


Figure 3.3: Newport AutoAlign workstation used for fiber and laser packaging

Zemax simulations also show that a 2.95 dB increase in coupling efficiency occurs when replacing the air between the fiber cladding and the grating coupler with epoxy. This is a result of removing a refraction that occurs at the cladding-air interface, which in turn causes significant phase mismatch at the grating input mode. This refraction will be discussed further in section 3.3.2.

3.3 Measurements

3.3.1 Alignment Tolerances

Measurements of the alignment tolerances were performed using a Newport AutoAlign waveguide alignment system (Fig. 3.3). Angle-polished fibers were placed into silicon V-groove carriers. The roll orientation of the fiber in the V-groove was performed using a visible laser. The reflected spot at a distance was compared to a line oriented perpendicular to the V-groove. When the spot was oriented along the line, the fiber was cured in the V-groove with UV cure epoxy.

Two fibers in V-grooves were then aligned over the input and output grating couplers of a straight waveguide. The automated metrology features of the AutoAlign software were used to measure the change in power output as the input fiber was moved in two axes parallel to the plane of the grating. The results of this are shown in Fig. 3.4a. These results are in good agreement with the simulations. In the X direction, the loss due to misalignment is less than 1 dB over a $5.5 \mu\text{m}$ range, whereas in the Y direction the range for the same loss is $5.2 \mu\text{m}$.

A similar process was used to measure the alignment tolerance of the working distance, with the results shown in Fig. 3.4b. At first glance, this would appear to be quite different from the simulation results in Fig. 3.2b. This is due to the sequential

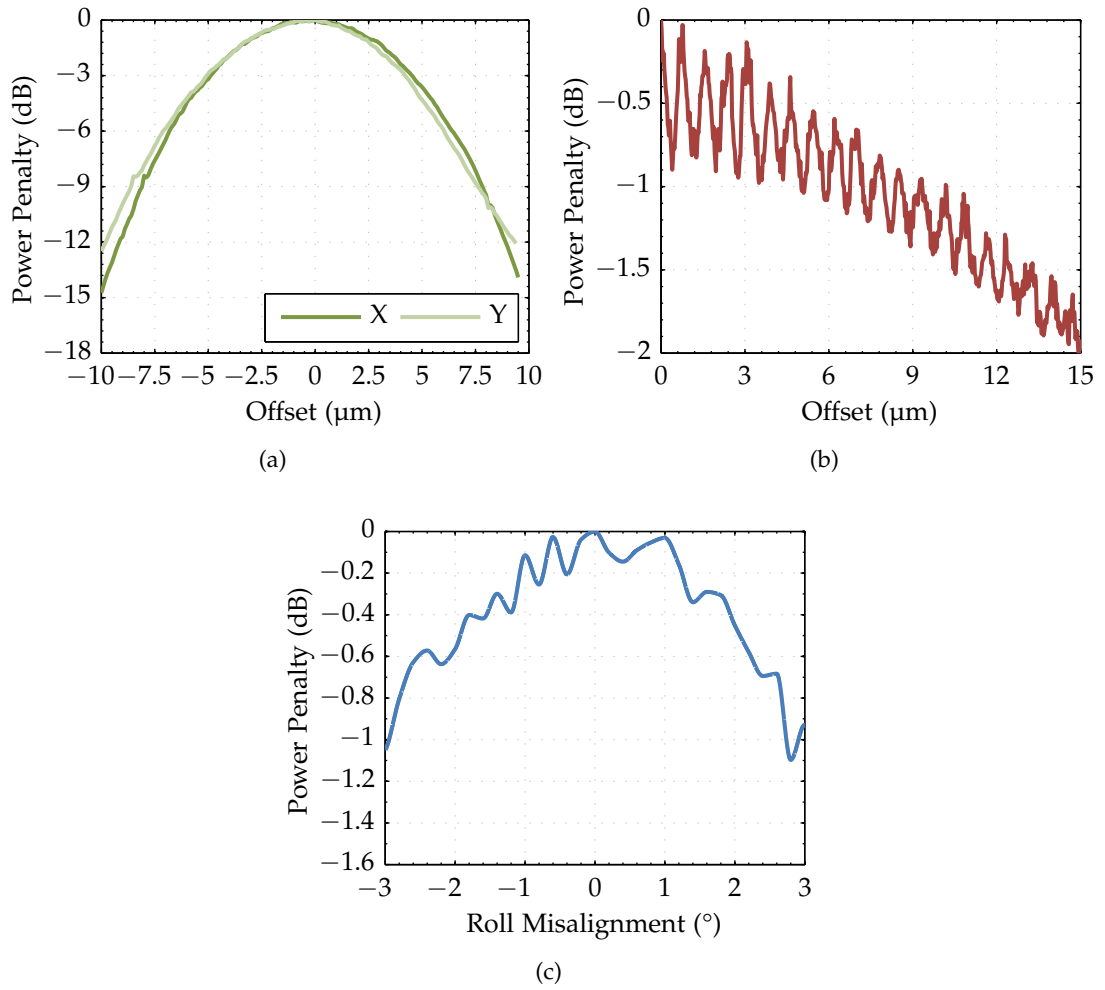


Figure 3.4: Measured alignment tolerances: (a) Along and across the plane of the grating (b) Working distance from fiber cladding base to grating surface (c) Roll along fiber axis

nature of the physical optics simulation in Zemax. That is to say that multiple reflections are not accounted for, and the Fabry-Pérot cavity formed between the lower surface of the fiber cladding and the grating is neglected. However, the resonances in Fig. 3.4b occur at roughly $\lambda/2$ intervals. This is consistent with what is expected in such a cavity according to the following relationship for Fabry-Pérot maxima,

$$\Delta\ell = \frac{\lambda_0}{2n \cos \theta} \quad (3.15)$$

where $\Delta\ell$ is the increment in reflector separation between successive transmission maxima, λ_0 is the central wavelength (in this case approximately 1550 nm), n is the index of refraction of the medium between the reflectors and θ is the angle between the propagating light and the normal of the reflecting surfaces. When one considers

the envelope of the measurement results and neglects the Fabry-Pérot oscillations, it becomes clear that the data in Fig. 3.4b match well with the simulation.

The roughness in the measurement can be attributed to vibrations as the fiber was moved and to the limited 100 nm resolution of the motion stage. Also, due to the vision system used, it was difficult to precisely determine the absolute distance between the fiber and grating at the beginning of the working distance scan. However, by fitting the envelope of the measurement to the simulated results, it can be determined that the initial working distance was between 2 μm and 3 μm .

Finally, a set of measurements was taken to ascertain the sensitivity of the coupling due to variation in the roll alignment of the fiber. These measurements were done manually at 0.2° intervals. Between each measurement, the fiber and V-groove were rolled slightly and realigned. Some manual compensation was also required for the working distance, as the fiber was not perfectly centered on the roll axis of the stage. As such, a certain amount of uncertainty was introduced by where the final working distance fell in the aforementioned resonances. However, these considerations are outweighed by the final results shown in Fig. 3.4c, where the additional loss due to roll misalignment is better than 1 dB over more than a 5° range. This result is also consistent with the simulated tolerance in Fig. 3.2c.

Taken together, these results mean that this packaging process is well-suited to passive alignment, which in turn facilitates wafer-scale assembly. The final roll alignment of the fiber can be done either with a high resolution camera imaging the fiber end facet, or by aligning a reflected spot from an infrared (IR) or visible light source. In particular, with a light source, the fiber can be raised or lowered above the chip surface, and the trajectory of the spot can be observed. If this trajectory is in line with the axis of the fiber then the roll is correct, whereas if it deviates to either side of the axis the roll should be adjusted.

The placement in X and Y can again be done with a suitable vision system and aided by alignment markers. The working distance can be minimized by using a side camera and top illumination and observing the reflection of the fiber on the chip surface. When the image of the reflection meets the image of the fiber, the working distance has been minimized. The precision of this process is sufficient to result in negligible additional loss and is used in current packaging activity.

As described previously, application of 0.5 μL of low-viscosity (300 cP) UV cure epoxy at least 2 mm from the fiber end facet results in a repeatable, controlled distribution through capillary action. The capillary effect causes the epoxy to stop just at the end facet of the fiber, maximizing the bonding area without flowing onto the critical end facet surface.

The epoxy curing process involved using a 100 W mercury arc lamp with a UV

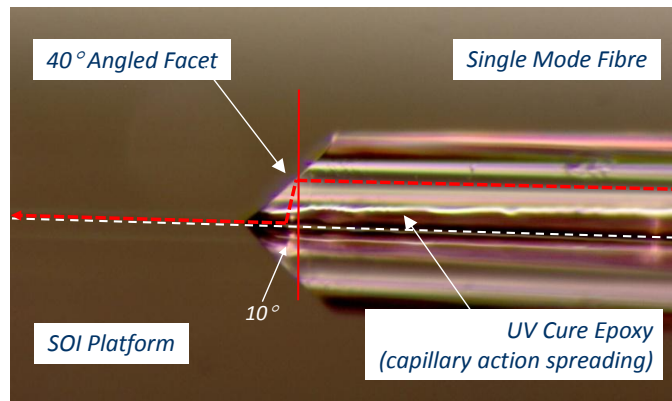


Figure 3.5: Fiber after controlled distribution of epoxy showing clean end facet

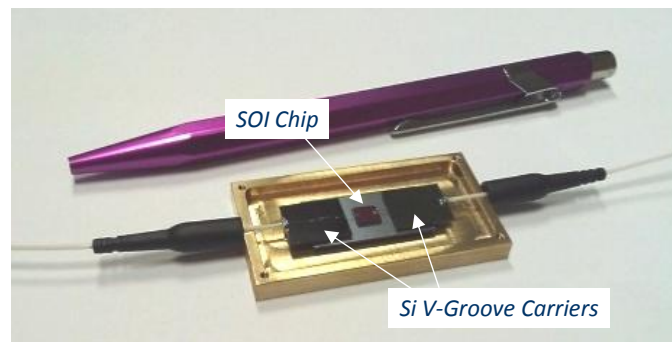
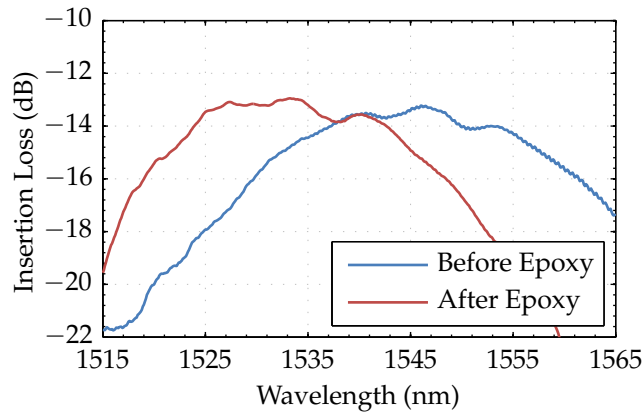


Figure 3.6: Completed package with top removed

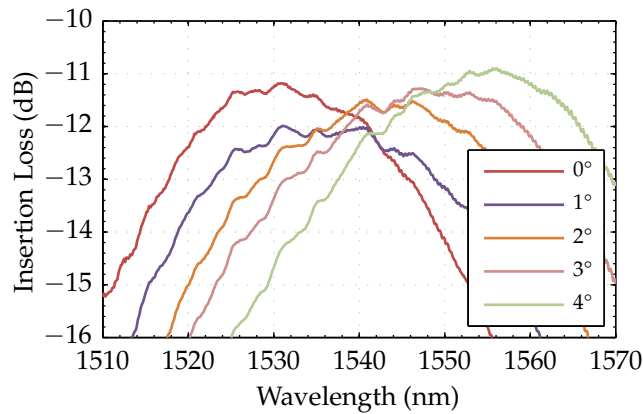
spectral range of 320 nm to 500 nm to precure the epoxy. A power level of 500 mW was applied for 150 s for a total curing energy of 75 J. During the precure, the epoxy experiences a linear shrinkage of 1.5% [44]. This shrinkage is actually beneficial as it occurs primarily in the optical axis of the grating coupler and thus reduces the working distance slightly. After the precure, the epoxy was baked for 12 h at 50 °C to complete the cure. This resulted in an aligned and affixed fiber as shown in Fig. 3.5. Complete packages were constructed by mounting the chip on a submount and attaching the V-grooves to the same. This assembly was mounted in a case with additional strain relief provided for the fibers. A sample of such a completed package can be seen in Fig. 3.6.

3.3.2 Coupling Efficiency

The optical coupling efficiency of a grating coupler varies with the wavelength of incident light. This variation can be measured efficiently with the use of a superluminescent diode (SLD) and an optical spectrum analyzer (OSA). The spectrum of the SLD is first measured, and then the output spectrum is measured after passing in one grating coupler, through a short waveguide, and out another grating coupler. The SLD spectrum is then used to normalize the output spectrum



(a)



(b)

Figure 3.7: Optical spectrum changes: (a) With epoxy and a flat-cleaved fiber (b) As the pitch of the fiber varies

and isolate the effects of the coupling with the grating.

For our packaging tests, a grating coupler designed to have highest efficiency in the telecommunications C-band was chosen. Furthermore, the grating chosen was designed to operate efficiently with both an air cladding and a silica cladding. These materials have indices of refraction of approximately 1 and 1.458 respectively. The epoxy chosen for affixing the fibers was Norland NOA 61, which has uncured and cured indices of refraction of approximately 1.527 and 1.54 respectively in the C-band [44]. Thus, this epoxy is very well suited for the chosen gratings.

However, the use of different cladding materials for the grating alters the optical spectrum of the coupling efficiency. In particular, the peak of the spectrum shifts. Previously, it was reported that a blue shift of 20 nm to 30 nm occurs with the application of epoxy in similar gratings [16, 45]. This test was repeated with the samples and epoxy on-hand using standard flat-ended fibers oriented at 10° off-vertical. This test yielded a blue shift of 14 nm (Fig. 3.7a).

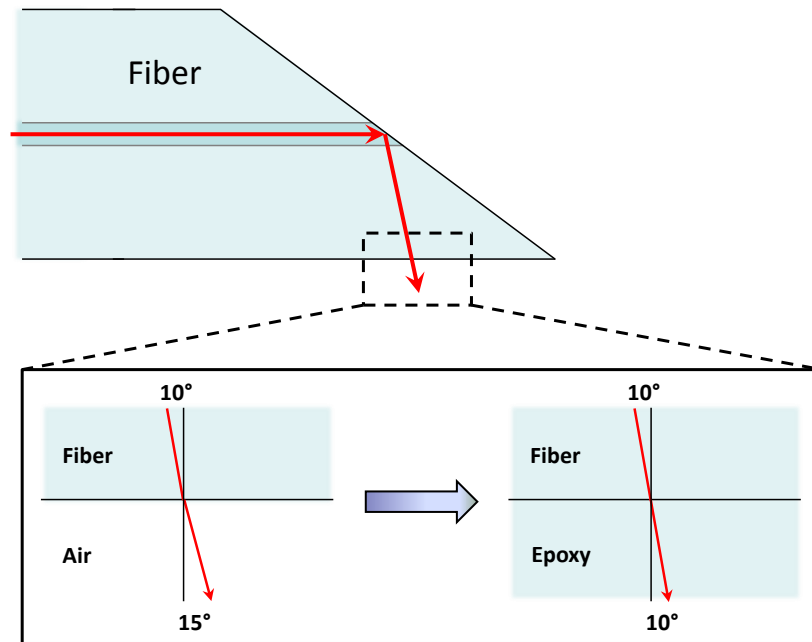


Figure 3.8: Schematic of changes due to the introduction of epoxy at the fiber base

In addition to the effects of the cladding material, there is also a dependence on the angle of the incident beam. While the design angle is set at 10° from vertical, there is some tolerance for variation from this value where coupling will still occur, and any variation results in a shift in the peak of the coupling efficiency spectrum. It was previously reported that a red shift of approximately 9 nm occurs for each degree of steeper orientation [17, 45]. Again, this test was repeated, this time using angle-polished fibers, and a red shift of 6.25 nm per degree (Fig. 3.7b) was measured with the samples on hand.

Both of these phenomena are important to understand. During the packaging process there is both a change in cladding material and a change of incident angle (Fig. 3.8). The latter occurs because there is initially a refraction of approximately 5° at the lower surface of the fiber. This is according to Snell's Law,

$$n_i \sin(\theta_i) = n_t \sin(\theta_t) \quad (3.16)$$

where n_i and θ_i are the index of refraction and angle of the beam on incidence, and n_t and θ_t are the same respectively of the beam upon transmission. When the epoxy is applied, index-matching removes this refraction, and thus a red shift is expected. Combined with the blue shift caused by the epoxy, the net result is a red shift of 10 nm (Fig. 3.9). It should also be noted that the index-matching eliminates the Fabry-Pérot cavity discussed previously.

Along with the shift in the wavelength of the peak, the coupling efficiency at the peak also rises. The observed rise of nearly 3 dB is consistent with the value

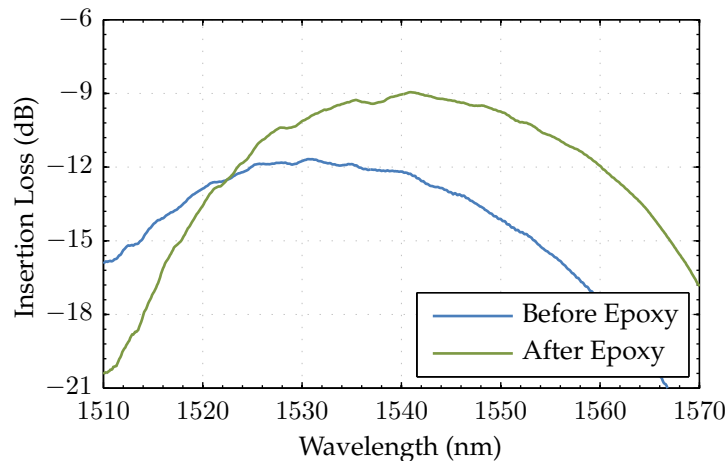


Figure 3.9: Net effect of epoxy with angle-polished fiber

obtained in simulation. The end result is a peak insertion loss of 9 dB fiber-to-fiber, or 4.5 dB from fiber to waveguide. This figure was measured with first-generation gratings, which had a theoretical maximum coupling efficiency of -4.3 dB per grating, and it also neglects the losses of the 4 mm waveguide connecting the input and output waveguide. Still, the final result falls within 0.2 dB of the theoretical maximum for the grating couplers chosen. With improved gratings such as in [21], it is expected that less than 1.9 dB fiber-to-fiber insertion loss will be achieved.

3.4 Packaging Design Rules

In order to facilitate fiber packaging of chips using this process, a brief set of design rules must be followed when laying out the photonic integrated circuit. In particular, the gratings must be placed in such a way that there is sufficient room for epoxy and so that input and output fibers will not collide during alignment. These rules are quantified in Table 3.2, which references the schematic in Fig. 3.10.

The rules regarding minimum distances from the edge arise chiefly from the requirements of distributing the epoxy. The X distance ensures that enough room is available to dispense the epoxy without it ending up on the fiber end facet, whereas the Y distance gives room for the epoxy to spread at the base of the fiber as in Fig. 3.5 and provide a sufficiently strong bond. The maximum distance is based on both a standard fiber order from the manufacturer and to avoid the lateral bending of long bare fibers that occurs when fine tuning the alignment with uncured epoxy in place. In other words, the longer the fiber, the more torque will be applied by the viscosity of the epoxy.

The separation of the gratings in X ensures, with a fair safety margin, that either of

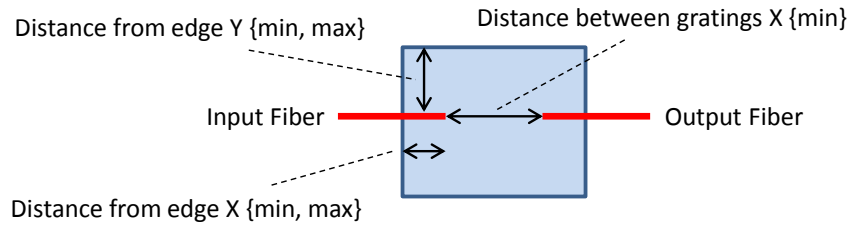


Figure 3.10: Schematic of single-fiber design rule dimensions

Table 3.2: Design Rules for Single-Fiber Packaging

No.	Parameter	Min	Max	Remarks
1	Distance from edge Y	250 μm	—	
2	Distance from edge X	1 mm	9 mm	
3	Grating pitch Y	—	—	
4	Distance between gratings X	500 μm	—	
5	Alignment channels	—	—	Must have measurable power from input to output

the fibers can be moved during alignment without coming into contact with the other. This margin is especially important during rotational movements such as yaw and pitch, where the rotational axis of the stage is not at the fiber tip and so significant translation of the fiber occurs.

For the single-fiber packaging process, there are no additional alignment channels such as will be seen later with the fiber arrays. The downside of this is that in order to do active alignment, there must be measurable power from the input to output fiber. This can pose problems if the device is detuned in its default state and is intended to be operated normally under electrical or temperature bias. This can be overcome by using passive alignment. However, passive alignment is intended for medium- to large-scale manufacturing, and the best performance from such a process will be achieved after first calibrating the fiber position relative to alignment markers using an active alignment.

It should also be noted during the design of the photonic circuit that epoxy will cover an area extending approximately 125 μm to either side of the fiber core in Y and from the chip edge to approximately 100 μm beyond the grating in X. This is important when a silica planarization layer is not present above the silicon waveguides. In this case, the epoxy will replace air as the cladding for the waveguide and change its effective index. Therefore, phase-sensitive devices such as ring resonators and AWGs should not be placed in this area unless they were

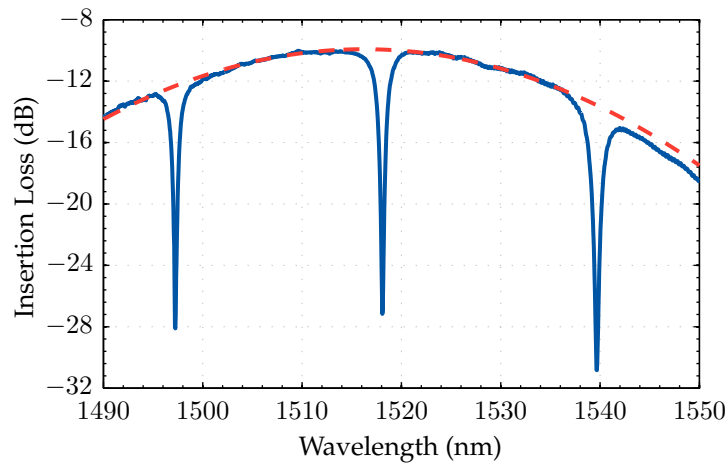


Figure 3.11: Optical transmission spectrum of packaged ring resonator filter (spectrum of grating coupler in dashes)

specifically designed to work with the epoxy cladding.

3.5 Conclusions

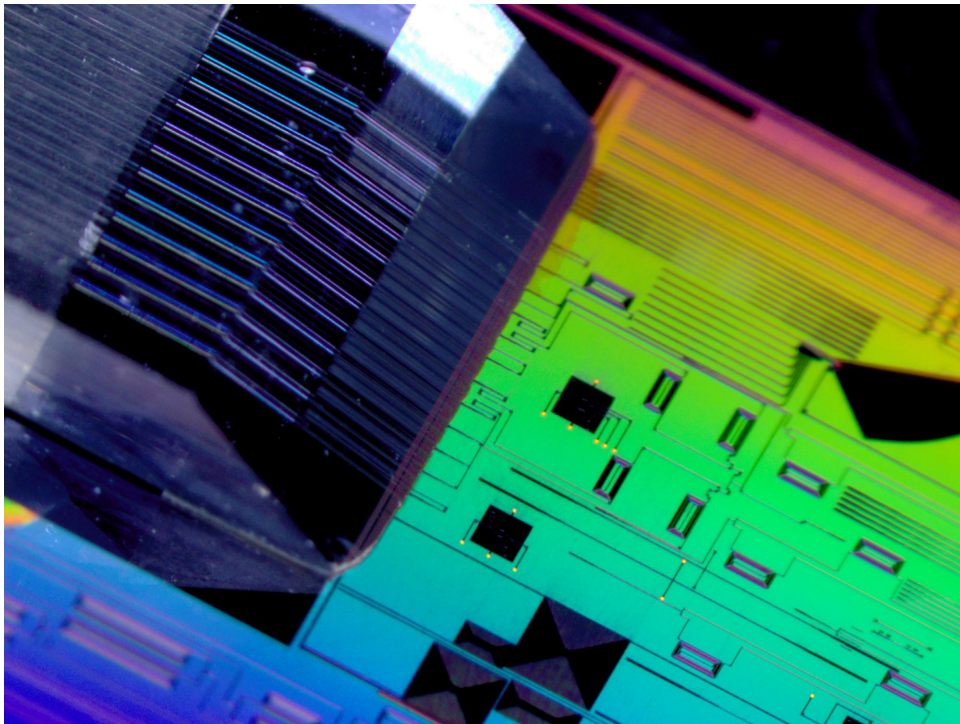
A novel planar fiber packaging process suitable for coupling light into and out of submicrometer grating-coupled photonic waveguides was outlined in this chapter. Simulations and confirming measurements for single input and output fiber packaging were presented. Results were obtained indicating that this technique can be successfully integrated into a passive-alignment-based wafer-scale manufacturing process. Furthermore, the measured coupling efficiency was within 0.2 dB of the theoretical value. With modern grating coupler designs, it is expected to be able to package planar devices with less than 1 dB loss between fiber and waveguide for both input and output, minimizing any impact on link budgets of devices and systems packaged using this process.

This packaging process is being offered publicly as part of the ePIXfab silicon photonics foundry service (www.epixfab.eu). An example of a device already packaged for researchers through this program is the ring resonator filter in Fig. 3.6 with the performance shown in Fig. 3.11. This and other successful work done through ePIXfab have proven the reproducibility and performance of the packaging process developed in this thesis beyond the specific chips and gratings used in the initial tests.

This packaging process was also successfully extended to fiber arrays for use in devices such as multi-port filters and demultiplexers. The additional issues that arise with multi-fiber scaling and alignment will be the subject of the following chapter.

Chapter 4

Fiber Array Packaging



4.1 Introduction

In the previous chapter, a process was described that enables the packaging of silicon photonic devices with individual fibers. While it is possible to repeat this process with multiple discrete fibers, there are practical limitations as to the pitch of the fibers and required clearances when doing the alignment. Also, the simple fact of doing multiple alignments adds to the packaging time, complexity and cost.

Instead, it is desirable to package with multiple fibers simultaneously in an array. This array can be formed by placing the fibers in an assembly based around V-groove technology. This provides an effective way to provide precise relative alignment between respective fibers. However, it presents its own set of challenges for coupling efficiency. This chapter will discuss those challenges as well as several solutions and come to a conclusion based around a highly-efficient design that maintains effective planarity and is manufacturable with high yield.

4.2 Construction

4.2.1 V-Grooves

V-grooves provide a convenient method of self-aligning and physically supporting single fibers or arrays of fibers. They can be made in either silicon or glass. They are formed either by partial dicing with an angled blade or by an anisotropic etching process, the latter method providing very precise relative alignment in arrays of fibers. In particular, when an etched V-groove is combined with a lid (Fig. 4.1), the three points of contact provide very accurate self-alignment of the fiber cores that is limited chiefly by the $\pm 0.7 \mu\text{m}$ tolerance of the cladding size and the $\pm 0.5 \mu\text{m}$ tolerance of the concentricity of the fiber core with the cladding [2].

In traditional end-coupled packaging applications, the end face of the fibers and V-groove assembly is polished to optical quality at either a flat 90° orientation or at,

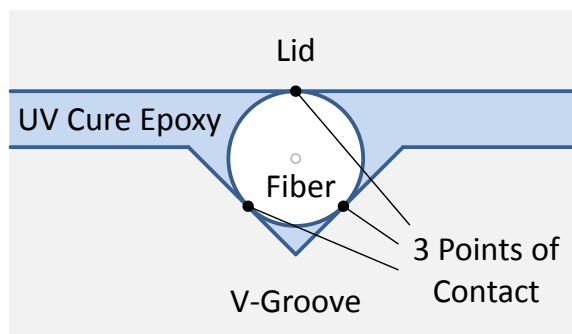


Figure 4.1: Diagram of V-groove showing precise three-point alignment

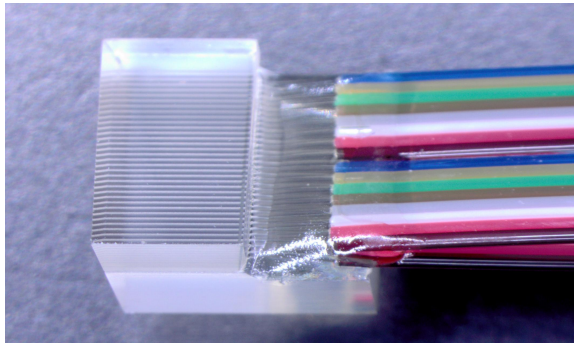


Figure 4.2: Standard $127\ \mu\text{m}$ pitch fiber array with 8° polish showing interleaved ribbons

e.g., an 82° orientation (Fig. 4.2) to prevent back reflections in much the same way as done with the angled polish on industry-standard FC/APC connectors (Fixed Connection/Angle-Polished Connector). The fiber array is then aligned to a photonic device with a matching polish. Any remaining gap between the V-groove assembly and the device to be packaged is then filled with ultraviolet (UV) cure epoxy, which provides index matching in addition to the physical bond.

4.2.2 Single-Polish Designs

The highly-accurate relative alignment of fibers in a V-groove can also be leveraged for planar packaging of near-vertical-incidence grating couplers. However, this poses some challenges for minimizing coupling loss and maximizing system performance. A standard V-groove assembly can be turned upside down and polished at a 40° angle to match the geometry of the single-fiber packaging process described in the last chapter. However, the minimum thickness for the lid (now below the fibers) is $400\ \mu\text{m}$ (Fig. 4.3). This results in significant losses as the light diverges in the distance between the input fiber and the input grating and between the output grating and output fiber. In principle, this could be mitigated by making larger input gratings and smaller output gratings, but this would then break the symmetry of the design and require optimization of two different grating designs. Moreover, the smaller output gratings would be limited in performance by the resolution of the lithography used.

The minimum thickness of the lid is set by the constraints of the process used to assemble the V-groove with fibers and lid. Using a thinner lid in this process results in low yield due to breakage during handling. However, it is possible once the initial assembly is completed to use chemical-mechanical polishing (CMP) to lap and polish the lid to thinner dimensions. Unfortunately, this approach also results in a low yield. Standard $125\ \mu\text{m}$ single-mode fibers used in v-groove assemblies come encased in a $250\ \mu\text{m}$ protective acrylate coating. This compensates for the

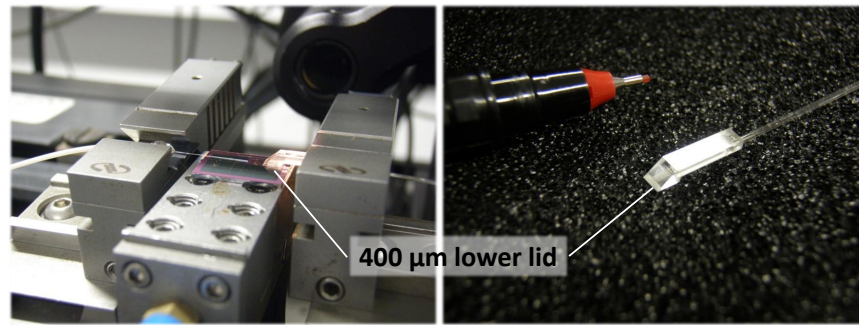


Figure 4.3: Standard fiber array with 400 μm lower lid and 40° polish

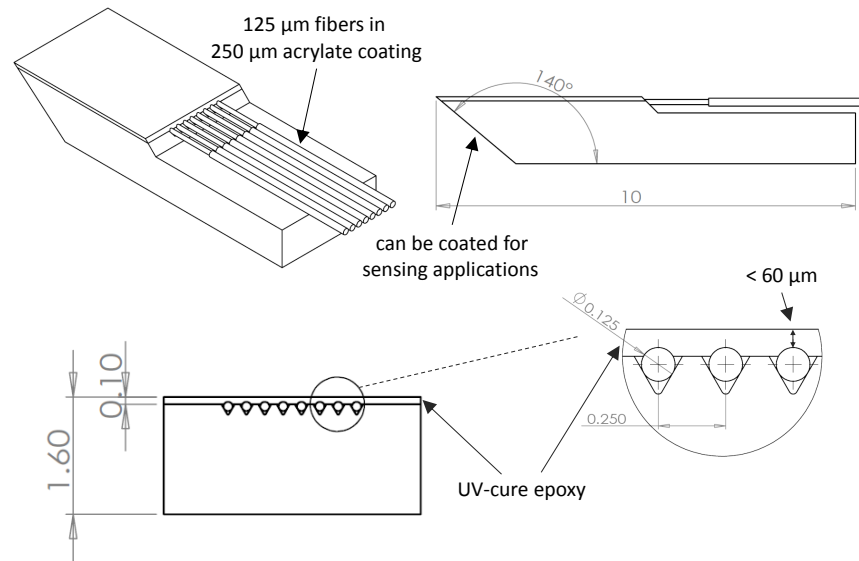


Figure 4.4: Schematic of “lidless” fiber array showing improved working distance

fragility of the glass fiber and allows it to be handled without breaking. To reduce the working distance below 125 μm from the fiber core and maintain a fully-planar package requires lapping and polishing into this coating. Experiments with doing this resulted in the shattering of upwards of 75 % of the fibers in the test arrays.

Another solution is to do away with the lid entirely (Fig. 4.4). In this process, the fibers are held down in the V-grooves and aligned by the combination of the downward force and the two points of contact with the groove. Then, a small amount of UV cure epoxy is applied and cured to maintain the position of the fibers. By doing this, the working distance can be reduced to less than 60 μm between the fiber cladding and the grating coupler without having to lap into the fiber coating.

Still, this process is not ideal either. The epoxy layer is not flat, which results in a small amount of lensing especially at the outside fibers. This is mitigated by the fact that matching epoxy can be used during attachment, so the lensing only becomes an issue during alignment. More troublesome is the low yield achieved when performing the 40° polish. Without the support of the lid, the edge of the V-groove

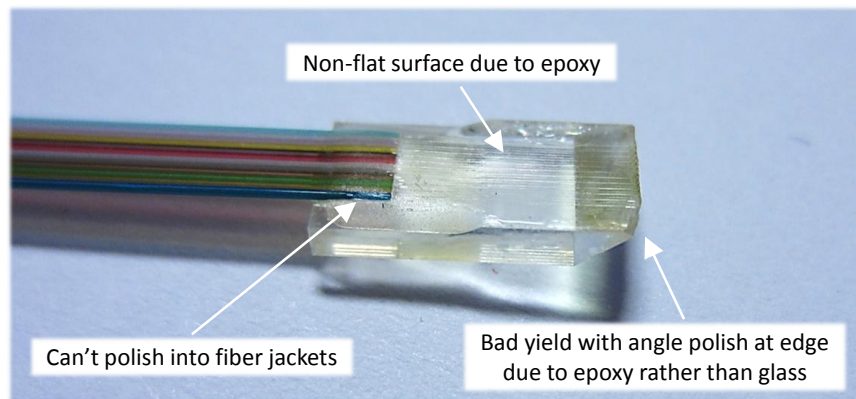


Figure 4.5: Image of “lidless” fiber array highlighting yield and performance issues

suffers cracking (Fig. 4.5), and for arrays larger than 8 fibers at a pitch of $250\ \mu\text{m}$, the outside fibers experience occasional cracking as well. In the end, however, the yield was sufficient to perform measurements and to do low-scale packaging at $250\ \mu\text{m}$ pitch with good coupling efficiency (Fig. 4.18).

Despite the success using a $250\ \mu\text{m}$ pitch, a further limitation of this process was its incompatibility with fiber arrays at the smaller standard pitch of $127\ \mu\text{m}$. Because V-groove assemblies at this pitch are produced by interleaving the fibers of two $250\ \mu\text{m}$ -pitch ribbons placed one on top of the other (Fig. 4.2), without the lid insufficient downward force was able to be placed on the fibers in the top ribbon to achieve proper alignment. This issue, as well as the previous issues, was solved by reintroducing the lid and fundamentally changing the geometry of the design.

4.2.3 Double-Polish Design

By relaxing the requirement for the packaging geometry to be completely planar, a new design was created (Fig. 4.6). This design retains effective planarity for the purposes of the larger package while opening the door to high-yield production and very high coupling efficiency. Instead of just polishing the facet once at 40° , the facet is polished twice. The first polish is at 36° , which results in an incidence angle of 18° according to (3.1). Furthermore, this polish angle of 36° meets the requirements for total internal reflection in (3.2). The additional 8° of incidence is compensated for by then polishing the lower facet at 8° . This angle maintains effective planarity while also removing the requirement of lapping into the acrylate coating. The final net polish angle of the edge is also increased from 40° to 44° , which further decreases the likelihood of chipping and improves yield.

With the lid in place, it is also possible to go even further by polishing into the fiber cladding. This reduces the working distance still more with the potential to reach distances from core to grating as low as $5\ \mu\text{m}$. This improves the coupling efficiency

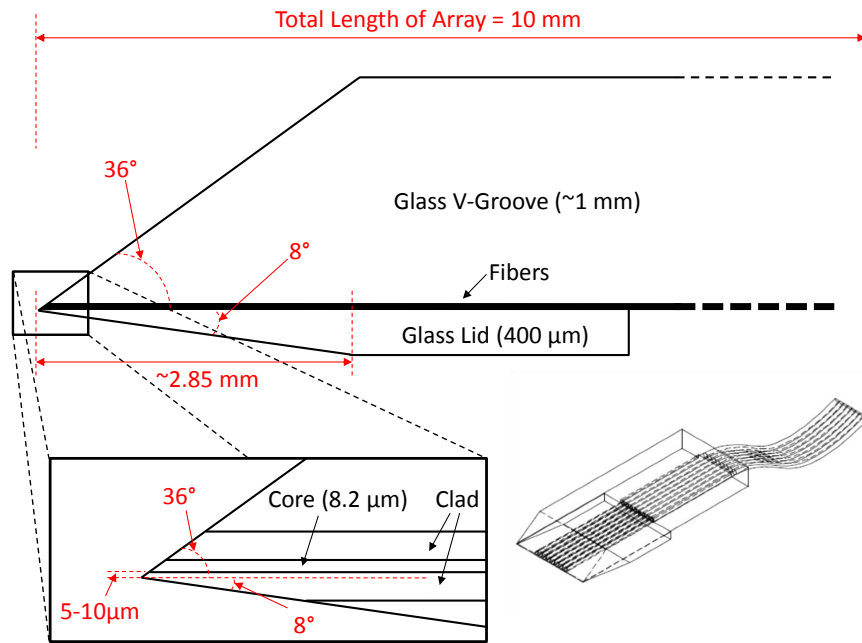


Figure 4.6: Schematic of double-polish fiber array showing near-planar layout and potential for very low working distance

beyond what was even achieved with the single-fiber packaging process. The amount of cladding removed can be measured directly using the micrometer gauge on the polishing jig or by measuring the length of the lower polished surface and multiplying by $\sin 8^\circ$.

4.3 Measurements

A series of measurements was performed using a 12-channel fiber array with a pitch of $250 \mu\text{m}$. This array was constructed based on the “lidless” design described before. The tests were performed by aligning the array over a shunt similar to in Fig. 4.16a consisting of twelve 1D grating couplers with the first and twelfth couplers connected. A broadband superluminescent diode (SLD) source was then used as the input into the first fiber of the array, and the output from the twelfth fiber of the array was measured using a power meter.

4.3.1 Alignment Tolerances

The first test performed was of the lateral alignment tolerances of the gratings when using the fiber array. The automated metrology features of a Newport AutoAlign workstation were used to create a map of the insertion loss as the fiber array was moved in an X-Y grid at 100 nm steps. The results were then normalized against the peak coupling efficiency and are shown in Fig. 4.7.

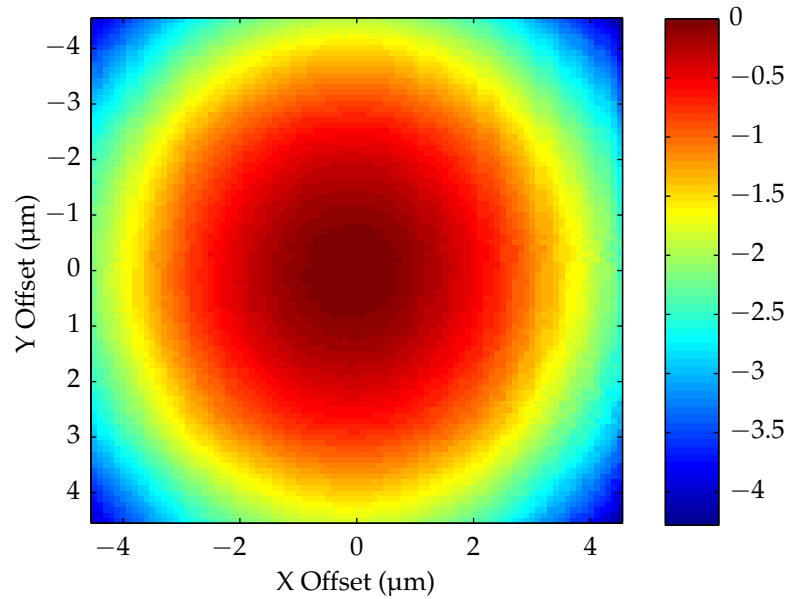


Figure 4.7: Lateral alignment tolerance of fiber array

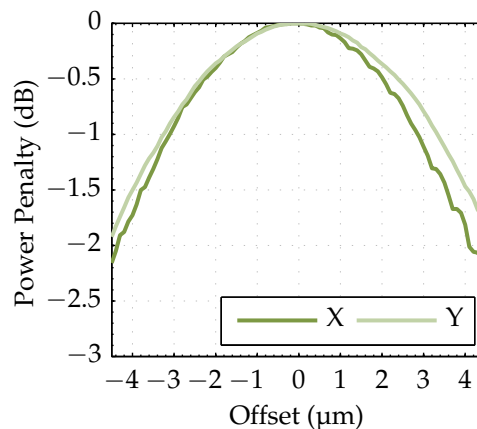


Figure 4.8: X and Y cross-sections of fiber array lateral tolerance

To better see the quantitative values of the alignment tolerance, two slices through the peak alignment point, one in the X direction and one in Y, were plotted. These plots are shown in Fig. 4.8. From this graph it can be seen that an additional loss due to misalignment of less than 1 dB occurs over a 6 μm range. At first glance this would appear to be better than even in the single-fiber case. However, one must take into account the increased working distance. This means that while the lateral alignment tolerance improves owing to the expanded beam at the coupler, the total coupling efficiency decreases for the same reason. In the end, even when the working distance is reduced, as in the double-polish design, the alignment tolerance will still be suitable for passive alignment.

As with the single-fiber packaging process, the rotational alignment tolerances of

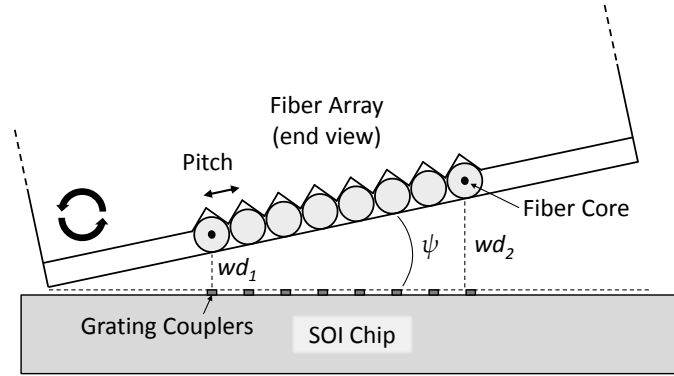


Figure 4.9: Schematic of effect of roll rotation on fiber array alignment

the fiber array must also be considered. The first tolerance measured was the roll of the array about an axis parallel to the fiber cores. In the single-fiber process, this was fairly tolerant with less than 1 dB loss over a 5° range. However, with the fiber array there are additional factors to consider. When the array is misaligned in the roll orientation (Fig. 4.9), there is a lateral offset induced. To quantify this, first consider the separation between the cores of the two outside fibers ℓ defined as

$$\ell = p(n - 1) \quad (4.1)$$

where p is the pitch of the fibers, either $250 \mu\text{m}$ or $127 \mu\text{m}$, and n is the number of fibers in the array. Then, given that one of the outside fibers is perfectly aligned above a grating coupler, the worst case lateral shift as experienced by the other outside fiber can be expressed by

$$\ell(1 - \cos \psi) \quad (4.2)$$

where ψ is the amount of roll misalignment. In general, this misalignment is quite small. For instance, a $12 \times 250 \mu\text{m}$ fiber array misaligned by 0.5° sees only a $0.1 \mu\text{m}$ shift. The more crucial factor is what a roll misalignment does to the working distances of the fibers. Given a typical array with 1 mm between the V-groove edge and the first fiber, and with the edge in contact with the chip, the working distances of the first and last fibers are increased by wd_1 and wd_2 respectively, defined as

$$wd_1 \approx (1\text{mm} + p/2) \sin \psi \quad (4.3)$$

$$wd_2 \approx (1\text{mm} + p/2 + \ell) \sin \psi \quad (4.4)$$

For the same array with a 0.5° roll misalignment, this results in an increase of nearly

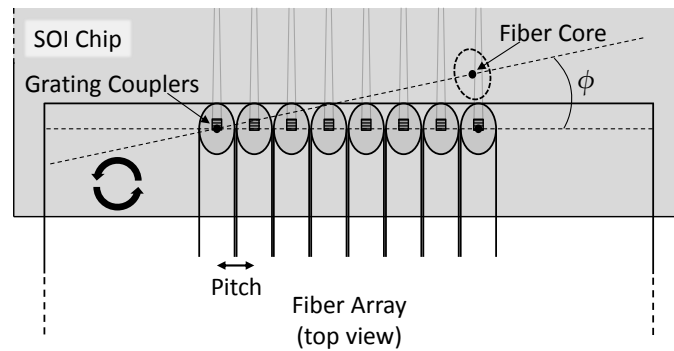


Figure 4.10: Schematic of effect of yaw rotation on fiber array alignment

10 μm for the first fiber and nearly 34 μm for the last fiber.

This tolerance was measured at 0.1° intervals, again using a $12 \times 250 \mu\text{m}$ array and a simple 1D-grating alignment shunt. After each roll, the working distance of the full array was minimized and corrected for any Fabry-Pérot resonances and a measurement was taken. The results are shown in Fig. 4.11a. These results show less than 1 dB loss over a 1.5° degree range. This is more severe than in the single-fiber process, yet using an array has one significant advantage. If the lower surface of the array is polished flat as in the double-polish design, then the array can be self-aligned through physical contact with the chip. If this is done, then the roll alignment is only limited by the accuracy of the polishing jig. For jigs manufactured using modern machining equipment, this accuracy is easily within 1° .

More crucial than the roll alignment is the yaw alignment (Fig. 4.10). For single-fiber packaging, this was very tolerant and alignment could be easily performed using passive techniques and the alignment features or waveguides present on a chip. For fiber arrays, however, a yaw misalignment results in a lateral shift of the fibers with respect to one another. Given one outside fiber aligned perfectly over a grating, the lateral misalignment of the other outside fiber for a yaw misalignment of ϕ is given by

$$2\ell \sin \frac{\phi}{2} \quad (4.5)$$

So, for a $12 \times 250 \mu\text{m}$ array, a yaw misalignment of only 0.1° already results in a lateral misalignment of 4.8 μm . The effects of this were measured at 0.01° steps using the waveguide alignment system. The results of this measurement are shown in Fig. 4.11b. They show that a 1 dB loss occurs with only 0.075° of yaw misalignment. Furthermore, these results correlate well with Fig. 4.8 when the angles are converted to offsets using (4.5). In the end, this yaw tolerance is the limiting factor on how wide or how many channels the fiber array packaging process can support and still be compatible with passive alignment. Even with

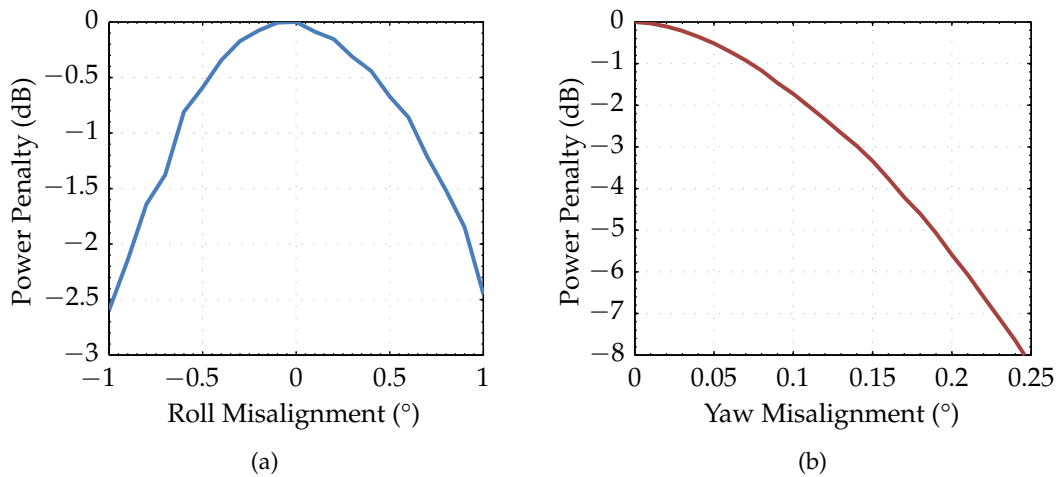


Figure 4.11: Measured rotational alignment tolerances: (b) Roll of fiber array about fiber axes (a) Yaw alignment of fiber array parallel to chip surface

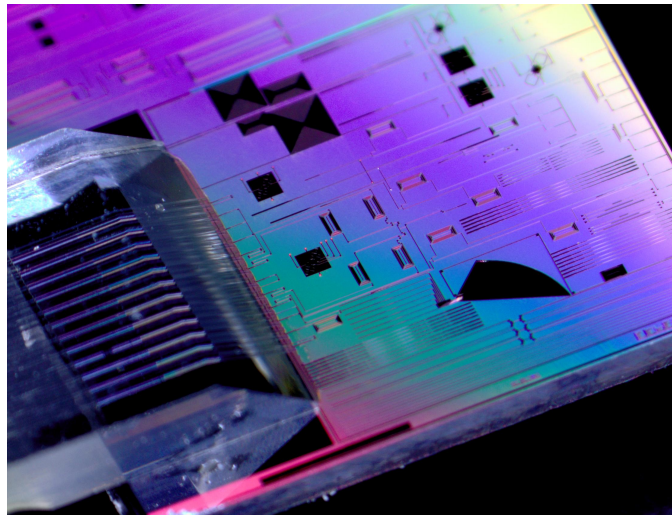


Figure 4.12: 12 channel array packaged with silicon photonic integrated circuit

active alignment, there is a limitation imposed by the accuracy of the rotational stages and the amount of time that can be devoted to packaging a single array.

4.3.2 Coupling Efficiency

Once the fiber array was aligned, a set of coupling efficiency measurements was taken. First, the coupling efficiency was taken without epoxy. This involved measuring the input optical spectrum from the SLD, followed by measuring the output optical spectrum from the fiber. The input spectrum was then subtracted from the output spectrum in the logarithmic scale to yield the spectrum of the insertion loss.

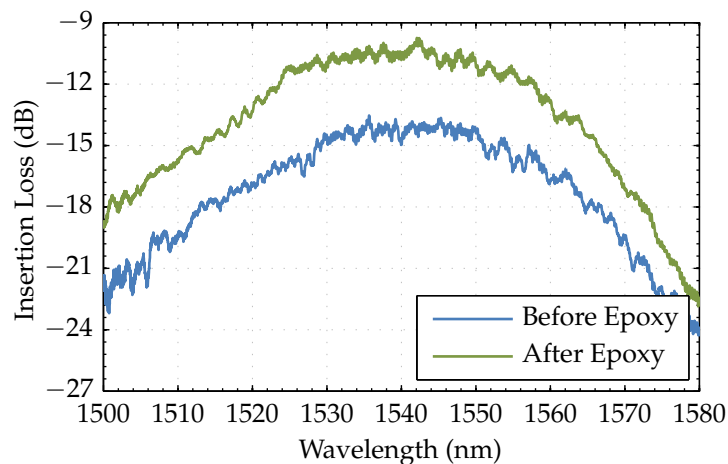


Figure 4.13: Fiber-to-fiber insertion loss of shunt connecting channels 1 and 12 of 250 μm pitch fiber array showing best-case loss of 9.74 dB

After taking the measurement without epoxy, approximately 40 nL of low-viscosity (300 cP) UV cure epoxy—enough to provide for up to a 5 μm layer of epoxy under the array—was applied and allowed to distribute under the array using capillary action. The epoxy was then precured under a UV lamp using a power level of 500 mW for 225 s for a total curing energy of 112.5 J. Once the precuring was complete, the same set of optical spectrum measurements was repeated. The results of both sets of measurements are shown in Fig. 4.13.

The first thing that can be seen is an increase in coupling efficiency after the epoxy is applied. This is similar to what occurred when introducing the epoxy during single-fiber packaging. The amount of the increase is approximately 4.5 dB and results from the index-matching of the epoxy as well as the decreased beam divergence in the epoxy versus air. However, unlike in the single-fiber case, no appreciable shift in the peak wavelength occurs. This is because the chip used for testing the fiber array had a silica planarization layer, which the chip used in the single-fiber tests lacked. The presence of the silica, which has an index of refraction near to that of both the fiber cladding and the epoxy used to construct the lidless array, compensates for the refraction that occurs when the light passes between the fiber array and air. As a result, the beam strikes the grating with nearly the same angle of incidence no matter whether the space between the array and the chip is filled with epoxy or with air.

A best-case insertion loss of 9.74 dB can be seen in the results. Considering the 4.3 dB loss of the gratings, and neglecting the 2.5 dB cm^{-1} to 3.0 dB cm^{-1} loss of the waveguides [46] as well as the loss of the bends, the results show an additional loss of less than 0.57 dB per fiber introduced by the packaging process. This in itself is a conservative figure considering that there were six 90° bends and approximately 3 mm of waveguide connecting the gratings. Still, with the introduction of the

double-polish design and the further reduction of the working distance between fiber core and grating, this loss is expected to improve significantly.

4.4 Packaging Design Rules

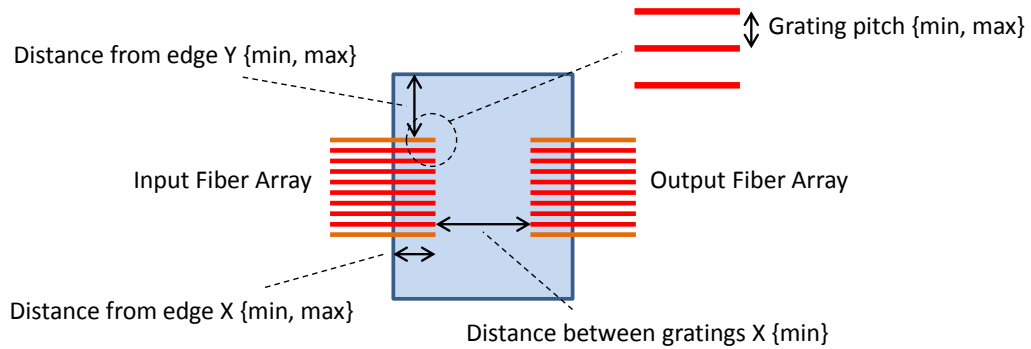
In addition to the single fiber packaging process described in the last chapter, the fiber array process detailed in this chapter has been incorporated into the packaging offering of the ePIXfab silicon photonics foundry service. In order to successfully package devices with fiber arrays through this service, a set of design rules must be followed. These relate to physical constraints as well as to ensuring that packaging can be done without having to rely on the performance of customer devices as in the case of the single fiber packaging.

First and foremost, certain physical clearances must be maintained. For fiber arrays with 250 μm pitch, these clearances are detailed in Table 4.1, with an illustration of the dimensions shown in Fig. 4.14. Unlike in the case of single fiber packaging, there is no minimum distance requirement in the Y direction. This is due to the effectively flat lower surface of the fiber array preventing the surface-tension induced epoxy arc seen in Fig. 3.5. It is also due to the array's greater size and assumes that the chip itself is more than 250 μm in the Y dimension. Thus, even with a grating coupler situated very close to the edge, there will be enough area for a sturdy epoxy bond.

The requirement of the minimum distance from the edge in X arises for similar reasons as with single fiber packaging and ensures that there is enough room to dispense the epoxy either from the side or from underneath, using capillary action to spread the epoxy in the entire area of contact between the array and the chip. The maximum X distance is a result of the 10 mm standard length of the fiber array, leaving a few millimeters at the end for the gripping clamp (shown in Fig. 4.3) and clearance with the sample stage of the waveguide alignment system.

In addition, the minimum X distance between gratings needs to be at least 1 mm due to the larger width of the fiber arrays and increased translation of the array corners during yaw rotations. The pitch in the Y direction, as measured from the center of one grating to the center of the next grating, must be a minimum of 250 μm . However, integer multiples of 250 μm such as 500 μm and 750 μm can be used for the pitch as well, so long as the total span does not exceed $8 \times 250 \mu\text{m}$. This maximum span is limited by the yaw tolerance of the fiber arrays measured previously.

Arrays with a pitch of 127 μm can be used for packaging as well. In this case, the schematic in Fig. 4.15 and the design rules in Table 4.2 apply. As with the 250 μm arrays, the pitch is not strictly limited to 127 μm , but can also be integer multiples of this value so long as the total span does not exceed $14 \times 127 \mu\text{m}$, again limited by

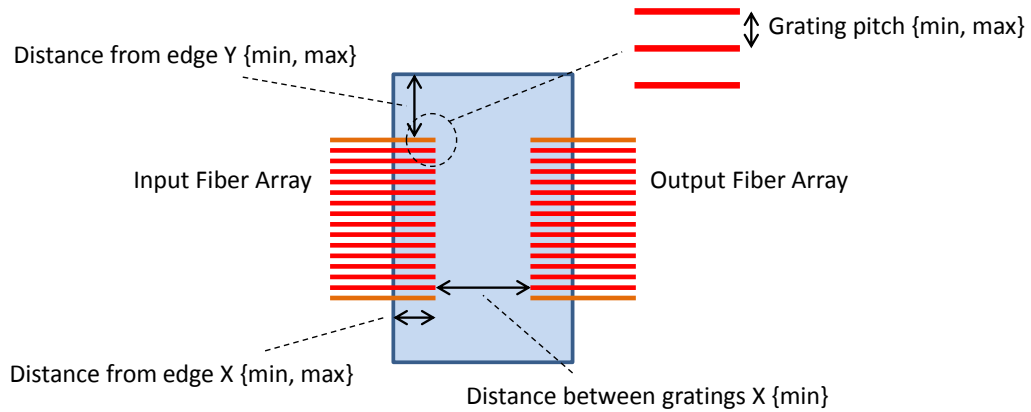
Figure 4.14: Schematic of 250 μm fiber array design rule dimensionsTable 4.1: Design Rules for Fiber Array Packaging at 250 μm Pitch

No.	Parameter	Min	Max	Remarks
1	Distance from edge Y	—	—	
2	Distance from edge X	1 mm	7 mm	
3	Grating pitch Y	250 μm	250 μm steps	Measured from center to center
4	Distance between gratings X	1 mm	—	
5	Alignment channels	2	—	10 channel arrays (8 usable, 2 for alignment)

the yaw alignment tolerance.

In both cases, two extra channels of the fiber array are used for connecting alignment shunt waveguides. These channels are shown in the schematics as orange lines, and the specific geometry of the shunt waveguides will be described in the next section. These additional channels are the reason that when using 127 μm pitch arrays the number of active channels is limited to 14. To facilitate 16 channels would require stepping up to a much larger 32 channel array or contracting an expensive custom production run of V-grooves. For $8 \times 250 \mu\text{m}$ packaging, a standard 12 channel array is used.

Similar to when designing for single-fiber packaging, with fiber arrays the area of the epoxy must also be considered. Upon packaging, epoxy will cover from the edge of the chip to approximately 150 μm beyond the grating in the X direction. Furthermore, the epoxy will extend approximately 4 mm in the Y direction, or 1 mm beyond the alignment shunt grating couplers in a design utilizing the full channel count. Again, phase sensitive devices such as AWGs or ring resonators should not be placed in this area unless they are designed to operate with an epoxy coating or unless the chip has been fabricated with a silica planarization layer.

Figure 4.15: Schematic of 127 μm fiber array design rule dimensionsTable 4.2: Design Rules for Fiber Array Packaging at 127 μm Pitch

No.	Parameter	Min	Max	Remarks
1	Distance from edge Y	—	—	
2	Distance from edge X	1 mm	7 mm	
3	Grating pitch Y	127 μm	127 μm steps	Measured from center to center
4	Distance between gratings X	1 mm	—	
5	Alignment channels	2	—	16 channel arrays (14 usable, 2 for alignment)

Bond pads and heaters should not be placed in this area either. This may at first seem burdensome, but it should be noted that the area occupied by epoxy or obstructed by the fiber array with this planar packaging technology is significantly less than that taken up in previous vertical fiber array designs.

4.4.1 Alignment Shunts

The required alignment shunts for fiber array packaging can be laid out in a variety of fashions depending on the application. Three sample geometries are shown in Fig. 4.16. Fig. 4.16a shows a basic design for use with 1D grating couplers. A waveguide is routed behind the active grating couplers to connect the two alignment couplers. The lithographic accuracy of the grating coupler placement means that if these two extreme couplers are well-aligned, then the other eight will be as well, within the limitations of the core alignment of the fibers in the V-grooves.

Fig. 4.16c shows a design that combines 2D active grating couplers and 1D

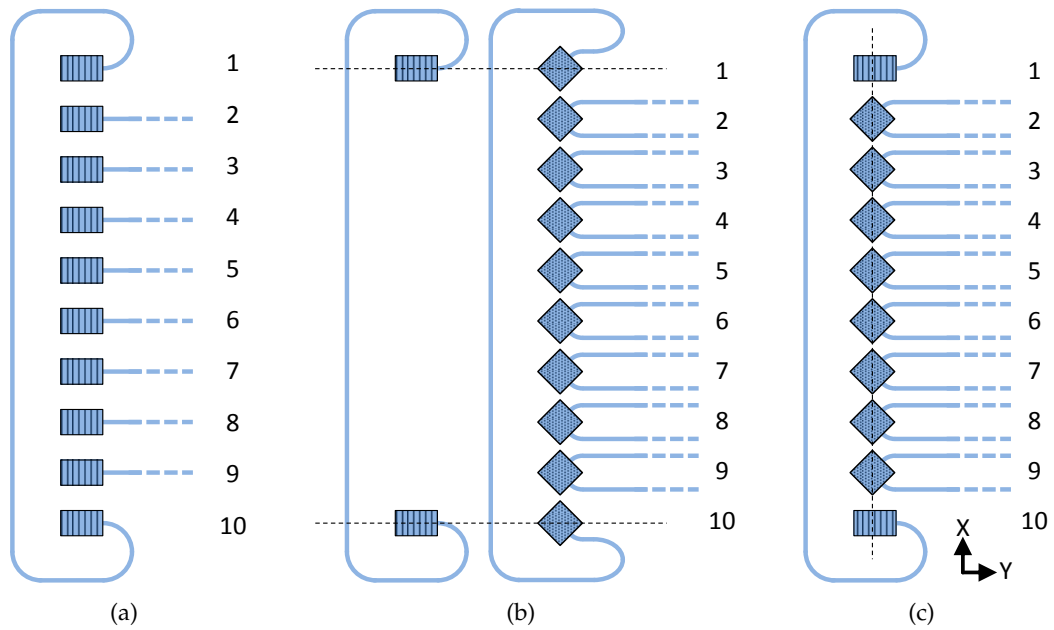


Figure 4.16: Schematics of alignment shunts for fiber array packaging: (a) Shunt for array of 1D gratings (b) Shunts for array of 2D gratings using two-step alignment process (c) Shunt for array of 2D gratings where relative position of optimal alignment is well-known for both 1D and 2D gratings

alignment grating couplers. It functions in much the same way as the all-1D geometry, but the introduction of 2D grating couplers presents an additional challenge for the designer. It is direct enough to lithographically align the optimal alignment points of the 1D and 2D grating couplers in the X direction as for both it is simply the geometric center of the grating in that axis. On the other hand, it is not as direct a process when aligning in Y. A simulation of each grating needs to be done to determine the optimal alignment points of each type of coupler in the Y direction, and then these two points must be properly aligned on the lithography mask (as in the dashed line in the figure). If the simulation matches well with the fabricated devices, then this type of shunt is a convenient and space-saving method for alignment.

If an accurate simulation cannot be performed, or if there is significant variation in the fabrication of the grating couplers, then the shunt geometry in Fig. 4.16b can be used instead. With this geometry, there is a two-step alignment process as outlined in Fig. 4.17. First, yaw alignment and alignment in the X axis is performed using two 1D gratings whose X midpoints are aligned with the X midpoints of the 2D gratings (per the dashed line in the figure). Then, the array is shifted only in the Y direction to the 2D grating area and the uncured epoxy is applied. After this, a final alignment is performed in the Y direction to locate the position with optimum coupling efficiency and the UV epoxy is cured. For this process to work properly, the 1D gratings need to be as close to the 2D gratings as possible, and the chip

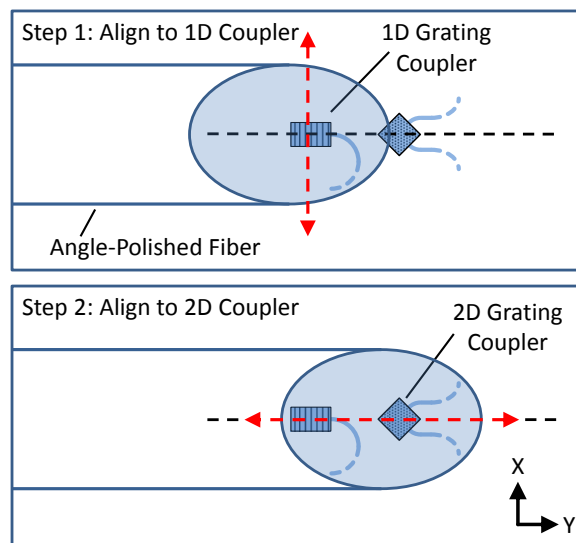


Figure 4.17: Two-step alignment process where 1D grating is used for X alignment and 2D grating is used for Y alignment

needs to be well-squared to the linear axes of the motion stage. If the chip alignment and stage alignment are not well-matched, then a small shift in the X direction may occur when moving in Y.

Neither of these latter two shunt geometries involved aligning in both X and Y using the 2D gratings. This is because performing the X alignment with the 2D grating can prove quite challenging. Each arm of the 2D grating couples a different orthogonal linear polarization into (and out of) the TE mode of its respective waveguide, and for each polarization there is a distinct point where there is optimal coupling [47]. These coupling points have been reported to be as close as $1\ \mu\text{m}$ apart, but lab measurements with available 2D gratings yielded a separation of approximately $4\ \mu\text{m}$.

Ideally, when packaged the fibers of the array will not be at either optimal coupling point, but at a point that balances the coupling of the two arms. One way to do this is to find each optimal point and then calculate the midway point between the two, yet this can be quite time-consuming. Another is to use a shunt where the waveguide connects one arm of one grating coupler to the other arm of another. However, this latter approach relies on the combined coupling efficiency of the two arms at the balanced point exceeding the coupling efficiency when positioned at the optimal point for one arm and a sub-optimal point for the other, which may not be true depending on the alignment tolerances, distance separating the optimal points or the input polarization. Instead, using the fact that the 1D couplers have a single optimal alignment point in X as in Figs. 4.16b and 4.16c results in a faster, more reliable alignment process.

4.5 Conclusions

In this chapter, the principle of planar fiber packaging introduced in the previous chapter was extended to arrays of fibers. Several designs for implementing the process using V-groove arrays were presented along with the challenges in realizing each design. Following this, the results of measurements of one of the designs were given, demonstrating alignment tolerances compatible with passive alignment and mass manufacture with the chief limitation being based on the combination of fiber count and pitch and their effect on the yaw tolerance. A coupling efficiency with less than 0.6 dB of the loss contributed by the packaging process was also demonstrated.

Significant interest in this multi-fiber packaging technology has already been shown, and it is currently being offered as a service of the ePIXfab silicon photonics foundry. An example of an arrayed waveguide grating (AWG) multiplexer/demultiplexer that was packaged through this service is shown in Fig. 4.18.

Detailed design rules for creating photonic integrated circuit layouts compatible with fiber packaging were presented in this chapter and are publicized through the ePIXfab website (www.epixfab.eu). Parametric components and design rule checks (DRCs) have also been implemented as a design kit add-on for Phoenix Software's MaskEngineer commercial software product. Furthermore, periodic in-person training sessions on ePIXfab and the use of MaskEngineer, including this packaging technology, have taken place in research sites throughout Europe. These sessions have been attended by researchers and students not just from Europe, but from across the globe.

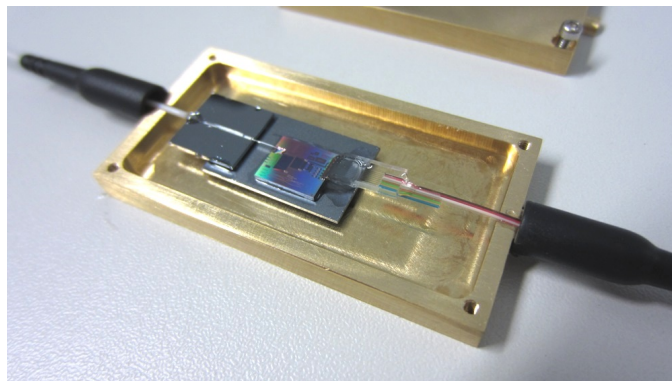
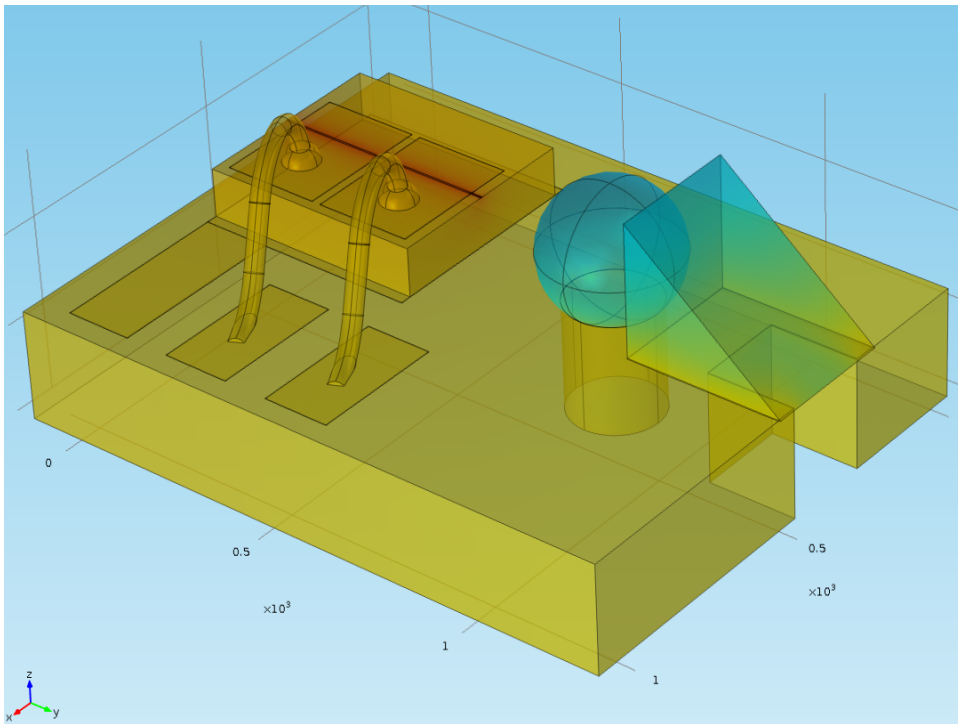


Figure 4.18: Fully-packaged AWG with single fiber input, fiber array output

Chapter 5

Design of Hybrid Integration Technology for Lasers



5.1 Hybrid Integration Techniques

For any photonic system, four principle design aspects must be considered: optical, mechanical, thermal and electrical. Of these four, optical and mechanical are typically given chief consideration. Optical is the first consideration, as this addresses whether the desired manipulation of light can be performed. Then, mechanical design must be considered to determine whether the system defined by the optics can actually be constructed. Finally, thermal and electrical design determines aspects of the performance of the system, e.g., whether a laser can be operated at an appropriate temperature for a desired output, or whether electrical modulation can pass through the system with a minimum of attenuation and reflection. The latter two often inform and modify the first two after a draft optical and mechanical design has been established.

In this thesis, three potential techniques for hybrid integration of a laser were considered. These included using actively-aligned micromirrors based on the previously-presented fiber packaging process, a micro-optical bench based on micro-opto-electro-mechanical systems (MOEMS) processing, and a micro-optical bench using discrete optical components. These techniques were evaluated against optical goals and mechanical feasibility, and eventually one technique was selected for further development and implementation. After a brief overview of all three, the full design process for the chosen technique will be described in detail.

5.1.1 Actively-Aligned Micromirrors

The first technique for hybrid integration that was considered emerged from the packaging work performed on single fibers. The angle-polished facet of the fibers functions as a micromirror. A key advantage of this type of mirror is that the fiber packaging process provides a convenient way to perform active alignment. The combination of the micromirror and grating serve as a planar mode adapter, where a standard fiber mode with mode field diameter (MFD) of $10.4\ \mu\text{m}$ at a wavelength of $1550\ \text{nm}$ is transformed to the submicrometer mode of the SOI waveguide. An edge-emitting laser can be either directly end-coupled to this mode adapter or else intermediary collimation or mode-conditioning optics can be used (Fig. 5.1).

To fully realize the micromirror, the majority of the fiber has to be removed. This can be accomplished by dicing. Either the whole chip can be diced off near the angled facet, or a shallow dice can be performed and the unused portion of the fiber and epoxy can be removed with mechanical force or by careful application of a solvent such as acetone.

For a full dice, the chief advantage is that the cut surface can be subsequently

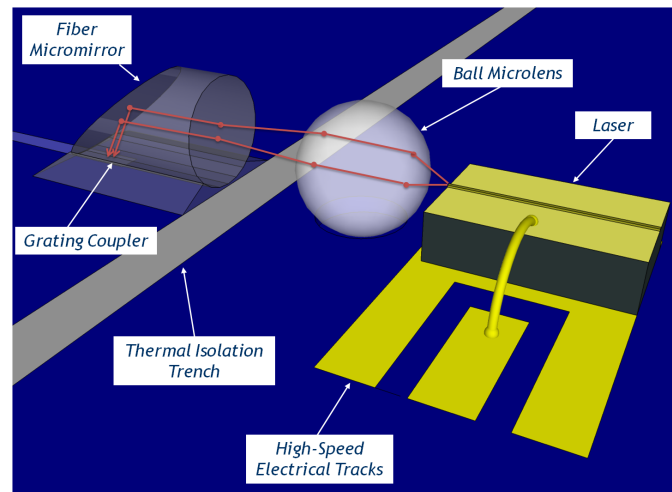


Figure 5.1: Schematic of actively-aligned micromirror

polished. After polishing, the chip and off-board laser can be aligned and mounted separately on an intermediate substrate for thermal isolation.

In the case of a shallow dice, later alignments are simplified as after dicing any alignment marks made during lithography remain aligned. On the other hand, thermal isolation is reduced significantly and direct polishing of the diced surface is not possible. As a result of this, the quality of the surface left by the cut must be evaluated. A test was performed with a standard dicing blade, and the results show significant chipping of the fiber material (Fig. 5.2). This roughness must then be removed or otherwise dealt with. One possible compensation method is to introduce index-matching material between the diced surface and intermediary passive optics. Another method for elimination of the roughness is the application of a controlled arc near the diced surface to bring the fiber just to its glass transition point and thus allow surface tension to repair the facet [48]. If neither of these proves effective or feasible, then another method such as fiber cleaving or scribing must be used to truncate the fiber.

A third option exists, combining the thermal isolation of the first with the alignment simplification of the second. This option consists of mounting the chip on an intermediate thermally-insulating substrate before dicing. Then, a dice is performed deep enough to cut through the chip but not through the substrate. The resulting deep trench increases the thermal isolation between the SOI pieces while leaving lithographic features on each portion aligned to one another. This approach leaves challenges similar to the case of the shallow dice *vis-à-vis* managing the quality of the optical surface.

Once the micromirror is realized, the laser and any passive optics must be aligned and attached. There are two alignment scenarios.

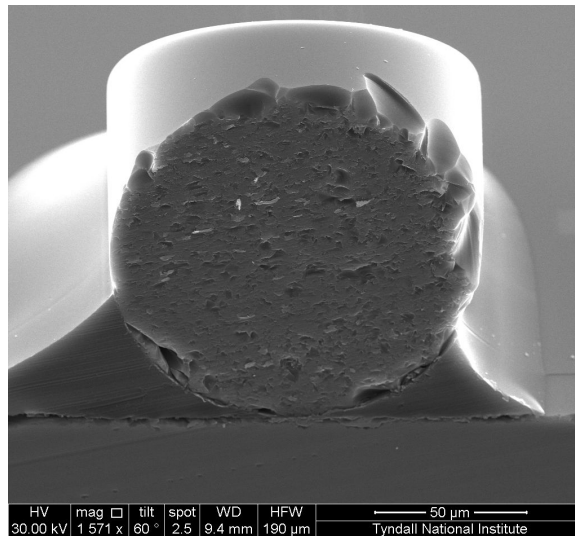


Figure 5.2: Scanning electron microscope image of diced fiber

The first scenario applies to the latter two dicing options, where the two portions of the original chip remain fixed in place with respect to one another. In this case, the optional ball lens can be self-aligned. This can be done with lithographic accuracy by deep reactive-ion etching (DRIE) a divot to position the lens, either during the same process flow as the grating etch, or in a separate micro-electro-mechanical systems (MEMS) etching process assisted by alignment marks from the first process. Once the divot is defined, the ball lens is secured in place using UV cure epoxy.

The laser can then be passively aligned based on alignment marks, or else it can be actively aligned using one of two processes. The first is an iterative flip-chip process with a custom tool to hold and power the laser. In this process, successive placements will be attempted until a maximum position is found. In the second process, the laser is attached to a custom tool on a waveguide alignment system consisting of motion stages with submicrometer accuracy. In either case, once alignment is complete, the laser is attached via thermocompression bonding or UV cure epoxy followed by wire-bonding of the top contacts. The height alignment is controlled by the thickness of the laser substrate and the thickness of the metal or SOI layer to which the laser die is bonded, with a possibility for adjustment by etching into the SOI. It is expected that the height can be controlled to within $\pm 1 \mu\text{m}$ [35].

This process has the potential to be fully-automated, but it may still prove to be time-consuming and inaccurate. Modern automatic flip-chip machines have a placement accuracy of $5 \mu\text{m}$. However, this accuracy applies to a passive alignment process and incorporates several factors including the optical resolution of the vision system, whereas an active alignment process can be designed and programmed to avoid some of these constraints. In fact, the chief limitation of active

alignment using flip-chip is the mechanical resolution of the X-Y-Z stage, which is 0.64 μm in the lateral directions for the state-of-the-art automatic flip-chip system available for this research. In the case of the waveguide alignment system, the mechanical resolution is much better at 0.1 μm or less.

In the second alignment scenario, which applies to the case of a full dice, there are two SOI pieces. The edge of the piece with the micromirror is polished using chemical-mechanical polishing (CMP), while the laser and optional ball lens are passively aligned and bonded to the other piece. The piece with the laser and optics is then actively aligned to the micromirror piece using a waveguide alignment system, and then both pieces are affixed to an intermediate substrate using a thin layer of UV cure epoxy.

The full-dice technique coupled with the latter alignment scenario has the advantage of simplicity and the ability to use CMP to improve the diced surface. However, if multiple lasers are to be aligned simultaneously, as in an array of lasers coupling to an array of waveguides, the coupling efficiency will suffer significantly from the multiple passive alignments of the lasers prior to actively aligning the array. This can be mitigated in system design by using a broadband laser or comb laser combined with an arrayed waveguide grating (AWG) demultiplexer or ring resonator filters, or else by using a tunable laser to substitute for multiple single-wavelength lasers.

5.1.2 MOEMS-Based Micro-Optical Bench

An alternative process to placing the laser and optics directly on the chip is to use a so-called "micro-optical bench." This consists of a micro-scale substrate which serves as a platform for constructing a free-space optical system. This bench can be aligned in plane with, or in the case of a near-vertical grating coupler, above the waveguide (Fig. 5.3).

One way to construct this sort of system is by using silicon pieces that have been etched using a deep reactive-ion etching (DRIE) process typically employed in micro-opto-electro-mechanical systems (MOEMS) and micro-electro-mechanical systems (MEMS) applications. With this etching, a gold-coated silicon micro-mirror with two legs for support can be constructed and placed into a substrate with deep slots etched to support and self-align the mirror over a deep-etched aperture. A divot can then be etched for the self-alignment of a ball lens. The laser itself can be attached by thermocompression bonding to a metallized portion of the substrate. The metallized portion can be designed to support high-speed electrical connection through, e.g., a ground-signal-ground (G-S-G) layout, or can contain a single ground pad with multiple additional lines for connection to a multi-section tunable laser.

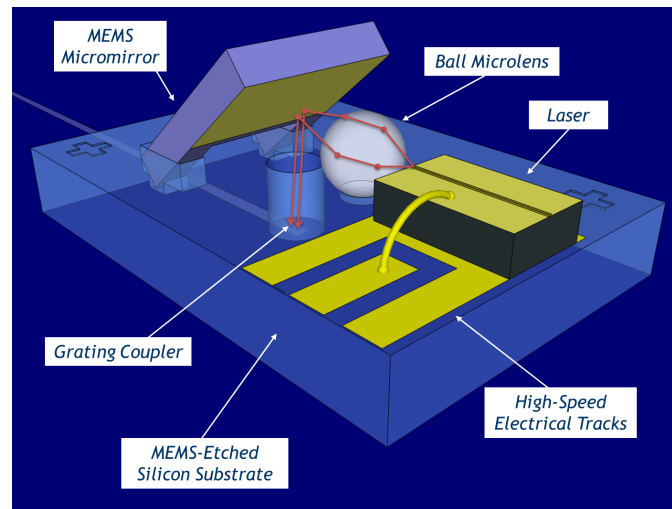


Figure 5.3: Schematic of MOEMS-based micro-optical bench

The principle of the optics of this system is quite simple. The ball lens collects and refocuses the output laser light, while the micro-mirror reflects the light to the 10° off-vertical input path of the grating coupler. The working distance from the laser to the ball lens is chosen so that the light will not be completely focused at the grating coupler, but will instead roughly match the $10.2\ \mu\text{m}$ mode field diameter (MFD) circular spot of a single-mode fiber, as this is the design input mode of the grating coupler.

The process of DRIE etching to construct an optical bench is appealing due to the very accurate alignment tolerance of lithography, however it does present some practical problems with structures such as those suggested above. First of all, the depth of the etches results in a low quality of the sidewalls. In particular, multiple iterations of etching must be performed which result in “scallop” on the side walls. Furthermore, due to limitations in the DRIE etching process, it is difficult to create steps at height differences of many micrometers, as in the case of the slots used to hold the mirror legs.

5.1.3 Discrete Component Micro-Optical Bench

An alternative to using MOEMS techniques to construct the various parts of a micro-optical bench is to use discrete components consisting of a selection of different materials. Instead of a DRIE-etched silicon substrate, a ceramic (AlN) substrate can be used. Ceramic substrates with laser-drilled features and patterned metallization, including Au-Sn solder reflow pads, are commercially available. Instead of etching slots into the ceramic substrate, a self-supporting prism inspired by the angle-polished fiber design can be used to reflect light to the 10° off-vertical input path of the grating. The ball lens can be self-aligned in a round hole

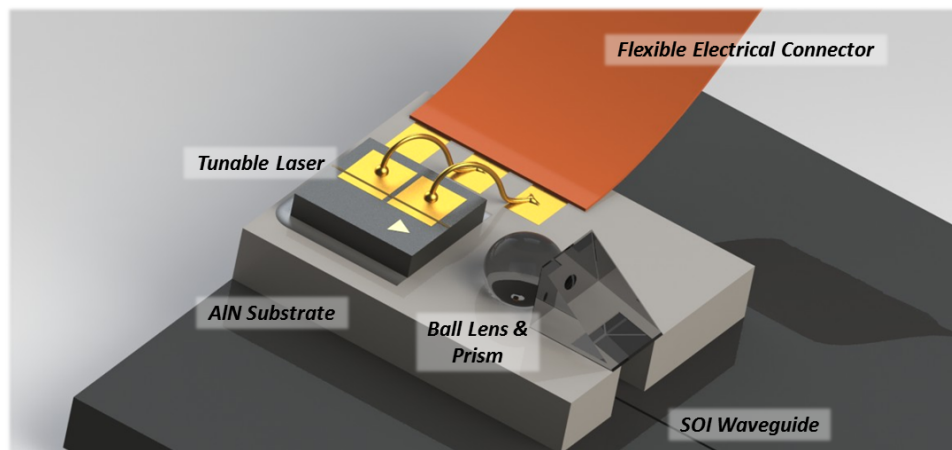


Figure 5.4: Schematic of micro-optical bench constructed with discrete components

laser-drilled through the substrate, and an aperture below the prism can be laser-drilled as well, while at the same time leaving space for the prism to be epoxy bonded to the substrate (Fig. 5.4). Rather than attaching the laser die with thermocompression bonding, a Au-Sn solder reflow pad can be used.

As with the MOEMS design, electrical tracks for high-speed and tunable lasers can be included. Moreover, the high-speed electrical performance of an AlN substrate is significantly better than that of a silicon substrate, and the thermal properties are better as well. A flexible electrical connector can be attached to the electrical tracks to aid in active alignment, and can later be removed to allow wire bonding from the micro-optical bench tracks to active areas on the silicon photonic chip.

This design was the one chosen to be pursued in this research. The chief disadvantage of the design is in the larger tolerances of the substrate (hole size for ball lens, pad position for laser, etc.) when compared to lithographic tolerances. However, these will be considered in the optical design, and it will be shown that the magnitude of these tolerances does not significantly impact the ability to construct a well-performing optical system. The following sections will describe this optical design, as well as the other aspects of system design in full detail.

5.2 Design Process

5.2.1 Optical Design

The principal goal of the optical design is to refocus the output light of the laser to match as closely as possible the optical input mode of a grating coupler. As with the earlier case of fiber coupling, this input mode is considered to be equivalent to that of a single-mode fiber tilted at 10° from vertical about an axis parallel to the ridges

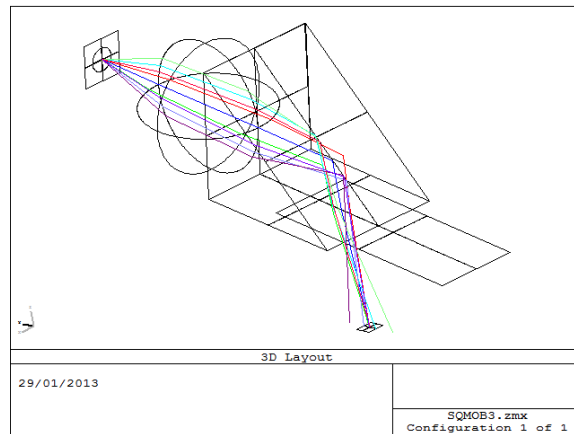


Figure 5.5: Zemax 3D layout of micro-optical bench

of the grating. A model of the optical components of the micro-optical bench was constructed in the commercial software Zemax as shown in Fig. 5.5. The definition of this model is shown in detail in Table 5.1.

In general, the output light from a laser can be approximated as a Gaussian beam with its beamwaist at the emitting facet. The evolution of the spot size of this light along the optical axis is given by

$$w^2(z) = w_0^2 \left[1 + \left(\frac{\lambda z}{\pi w_0^2} \right)^2 \right] \quad (5.1)$$

where w is the radius of the beam at a given position z , w_0 is the radius at the beamwaist, and λ is the wavelength of the beam in the material [49]. In the far field, this behavior can be approximated as a simple diverging cone with half-angles in each axis given by

$$\theta \simeq \frac{\lambda}{\pi w_0}. \quad (5.2)$$

Using this relationship, the far field of a laser can be used to approximate the spot size at its output facet, which can then be used to simulate a particular laser. As this divergence varies for different laser designs, a worst case and best case divergence of 30° and 10° was chosen for the purposes of making the micro-optical bench design as flexible as possible.

The Physical Optics Propagation feature of Zemax was then used to perform the simulation. This simulation included the effects of diffraction and losses incurred through single reflections. The ideal working distance from the laser to the ball lens was determined by using a macro to simulate a range of values, from which the optimal value was chosen and set in the model for all later simulations. The

Table 5.1: Zemax Lens Data for Laser Integration

Surface	Type	Radius	Thickness	Glass	Aperture	Tilt/Decenter	Description
0	Standard	Infinity	1 μm				For Ray Drawing Only
1	Standard	Infinity	171 μm		100 μm \times 100 μm Rectangle		Stop Surface
2	Coordinate Break		0				Used for Alignment Tolerance
3	Standard	150 μm	300 μm	N-BK7	150 μm Semi-Diameter		Ball Lens Start
4	Standard	-150 μm	0		150 μm Semi-Diameter		Ball Lens End
5	Coordinate Break		0				Used for Alignment Tolerance
6	Standard	Infinity	179 μm	N-BK7	300 μm \times 300 μm Rectangle	40 μm Decenter Y Before Surface	Prism Start
7	Coordinate Break		0			-50° Tilt About X	Set up Angled Reflector
8	Standard	Infinity	0	MIRROR	300 μm \times 466 μm Rectangle		Prism Reflector Surface
9	Coordinate Break		-150 μm			-40° Tilt About X	Finish up Angled Reflector
10	Standard	Infinity	0		300 μm \times 358 μm Rectangle		End of Prism
11	Standard	Infinity	-255 μm		200 μm \times 500 μm Rectangle	-223 μm Decenter Y Before Surface 223 μm Decenter Y After Surface	Substrate Aperture
12	Standard	Infinity	0		40 μm \times 40 μm Rectangle	-137 μm Decenter Y Before Surface -10° Tilt About X Before Surface	Grating Coupler Surface

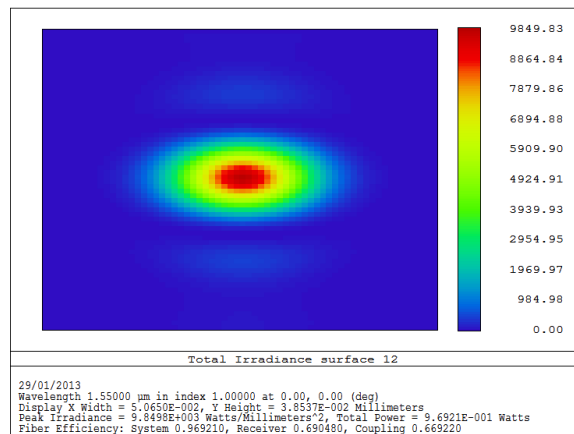


Figure 5.6: Zemax physical optics propagation output showing irradiance at input grating

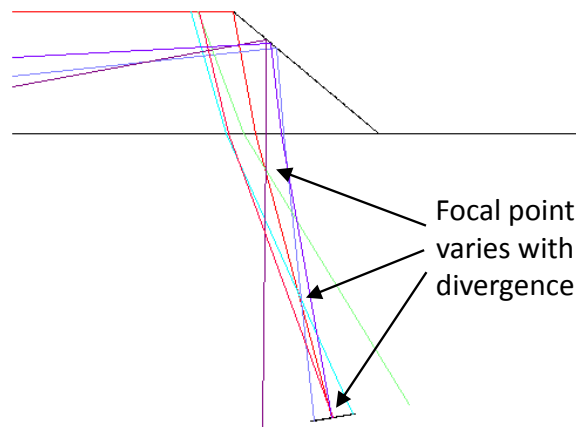


Figure 5.7: Close-up of plan rays in Zemax showing effects of spherical aberrations

contents of this macro are shown in Listing A.1. This code can also be used to plot the assembly tolerances of the micro-optical bench as will be discussed later.

Once the optimal working distance was determined, the simulation returned the resulting field at the grating as shown in Fig. 5.6. The differing divergences are readily evident from the non-circular field. Also, side lobes in the vertical direction indicate wave interference. This interference is due to the spherical aberrations that result from using a balls lens. Closer inspection of the 3D layout (Fig. 5.7) shows rays of different initial divergence angles coming into focus at different points along the propagation path, clearly illustrating the effects of the aberrations.

In fact, spherical aberrations are the main limiting factor in the ability of this optical system to match the desired mode as they result in significant phase mismatch. In an ideal system, an aspherical lens could be used to compensate for these aberrations. However, the alignment of such a lens proves difficult in this design. As

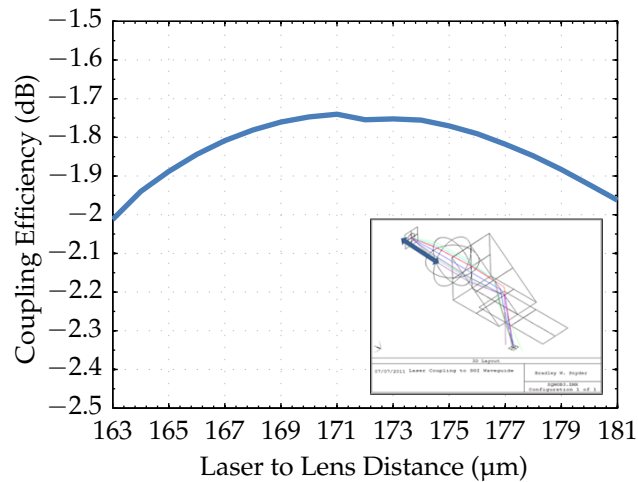


Figure 5.8: Simulation results for laser to ball lens working distance tolerance

will be discussed later, for future work a design has been proposed that allows for mass-produced aspherical lenses with simplified alignment.

In the end, this design predicts insertion losses from laser to grating of 1.74 dB for antireflective-coated components and 2.84 dB for bare components. This however does not include the losses of the grating coupling to the SOI waveguide, which have been reported to be as low as 0.75 dB [21].

With the draft design in hand, the assembly tolerances of the components must be determined. If these tolerances are too tight, then the design must be refined to specify a system that is actually manufacturable. Ideally, a self-alignment process will be used in as many cases as possible, with a passive process used for any remaining alignments. Active alignment is to be avoided whenever possible. In this micro-optical bench design, the placement of the ball lens is done using self-alignment, where the ball fits into the laser-drilled hole. Furthermore, the alignment of the prism and ball lens is performed using a self-alignment process in which the prism is placed in intimate physical contact with the ball lens.

The final alignment is that of the laser itself, which is a passive process. This process is aided by the position of the Au-Sn solder pad and by the fact that the ball lens itself serves as a fiducial alignment feature. Machines used for passive-alignment-based placement, such as flip-chip machines, rely on vision systems to determine position. A characteristic of a good fiducial alignment feature is that its absolute position can be determined irrespective of small errors in the focus of the vision system. The ball lens possesses this characteristic due to the fact that its center lies at the same position no matter whether it is perfectly in focus or slightly out-of-focus.

Given the center of the ball lens and the edge of the solder reflow pad as points of

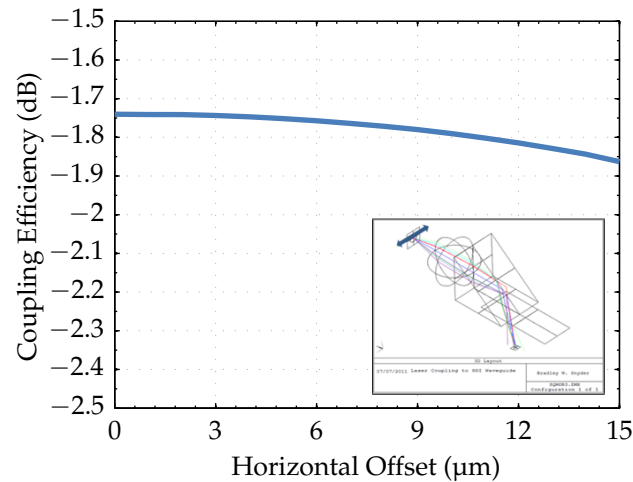


Figure 5.9: Simulation results for laser lateral alignment tolerance

reference, there are then two axes of misalignment for the laser placement. The first is the working distance of the laser to the ball lens, defined by the accuracy of the position of the solder pad edge and the accuracy of placing the laser at that edge. The previous macro used to find the optimal working distance also provides data about the tolerance of this value. The data for this is shown in Fig. 5.8. This data shows a penalty of less than 0.3 dB over an 18 μm range. The other potential misalignment occurs in the lateral placement of the laser. Ideally, with the laser facet aligned to the solder pad, the laser active region will be collinear with the center of the ball lens. The Zemax macro in Listing A.2 can be used to simulate the tolerance of this alignment, with the resulting data shown in Fig. 5.9. Again, this data shows a high degree of tolerance, with a maximum of 0.1 dB power penalty $\pm 15 \mu\text{m}$ away from the ideal position.

A further degree of misalignment can occur if the size of the hole for the ball lens varies. This will be discussed in detail in the following section on mechanical design.

5.2.2 Mechanical Design

With the draft optical design completed, the initial mechanical design can be performed. In this case, the mechanical design is fairly direct. 250 μm -thick AlN was chosen as the substrate material. The laser-drilled round alignment hole is sized to center the ball lens at the typical height of a laser, in this case taken to be 110 μm , which results in a 204 μm diameter hole. The aperture is sized so as to provide sufficient support for the sides of a 300 μm -wide prism while also resulting in minimal obstruction to the reflected light. The solder reflow pad for the laser is chosen to be a standard Au-Sn alloy and is placed at the distance from the ball lens specified in the optical design, with a size of 500 $\mu\text{m} \times 500 \mu\text{m}$ suitable to

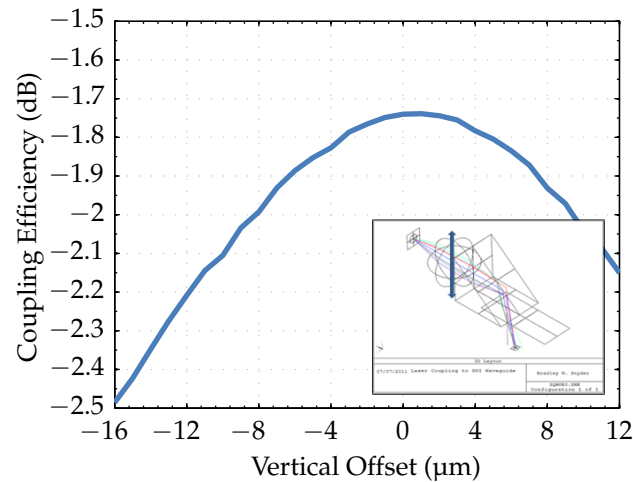


Figure 5.10: Simulation results for ball lens height variation due to manufacturer tolerance

accommodate most semiconductor laser dies. Furthermore, three basic electrical tracks in gold are placed on the substrate with one connected to the solder pad as a hardwired cathode connection.

This draft mechanical design was then sent for review to L.E.W. Techniques, a firm whose specialties include manufacturing ceramic submounts for microelectronics applications. Feedback and tolerance data were returned that then required some modifications to the draft design. In particular, there is a restriction that the distance between a laser-drilled hole and the edge of the substrate, or between the hole and the laser-drilled aperture, should be at least equal to the substrate thickness [50]. As a result, the distance from the aperture and ball lens hole to the substrate edge was increased by 100 μm and the distance from the ball lens hole to the aperture was increased. The latter dimension was only increased to 200 μm, as in combination with the ±30 μm size tolerance of the aperture there was the possibility of the aperture blocking some of the reflected light. This deviation from the supplier design rules was accepted as a risk to yield, but was considered necessary for optical performance.

Another tolerance that had to be considered was the ±30 μm tolerance of the ball lens hole size. Variations in this size result in a variation of the height of the ball lens. A simple geometric analysis shows that this can cause the lens to be lowered as much as 16 μm or raised as much as 12 μm. This information was then fed back into the optical design to determine what effect this might have on the performance. The macro used to perform the simulation is shown in Listing A.3, and the results of the simulation are shown in Fig. 5.10. These results show a reasonable tolerance, with a maximum additional loss of approximately 0.7 dB. Whereas this tolerance is not ideal, it is mitigated in part by the tendency of the affixing epoxy to raise the ball

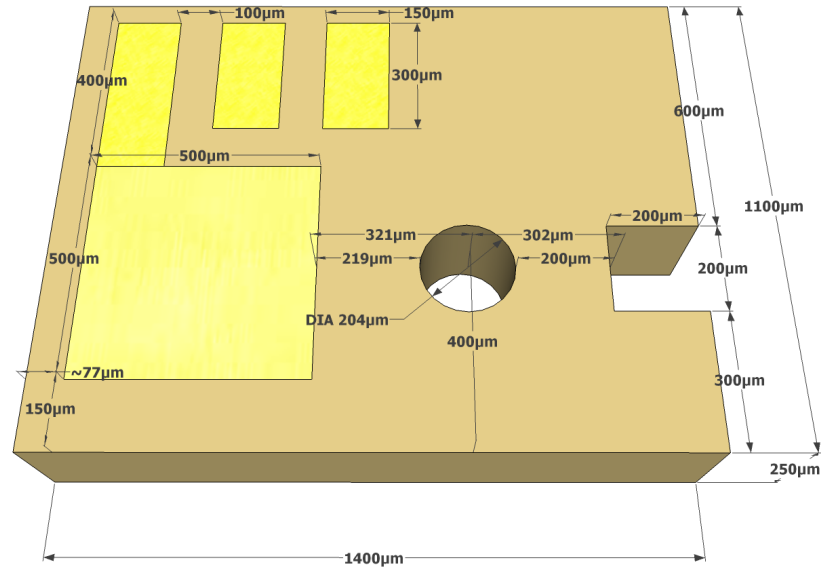


Figure 5.11: Mechanical design of micro-optical bench substrate

lens a few micrometers, thus moving the distribution of heights to a range with lower loss.

A plan view of the final design as submitted to the manufacturer is shown in Fig. 5.11.

5.2.3 Thermal Design

A basic temperature simulation was performed to validate the thermal behavior of the system. This simulation was done in the commercial software COMSOL, which uses the finite element method to perform physics calculations on discretized systems. In the case of the thermal design of a hybrid integration technology for CW lasers, it is primarily important to find the steady-state thermal response of the system. In particular, it must be shown that it does not diverge. In order to do this, the Heat Transfer Module of COMSOL [51] was used to solve the heat equation

$$\rho C_p \frac{\partial T}{\partial t} = \nabla \cdot (k \nabla T) + Q \quad (5.3)$$

where ρ is the density, C_p the specific heat and k the thermal conductivity of a material, T is the temperature and Q is any additional heat generated, e.g., by the active region of a laser.

This equation is governed by a set of boundary conditions. For the purposes of this design, two types of boundary conditions were used. The first was natural convection cooling, whereby heat is removed by an unforced flow of air. This is

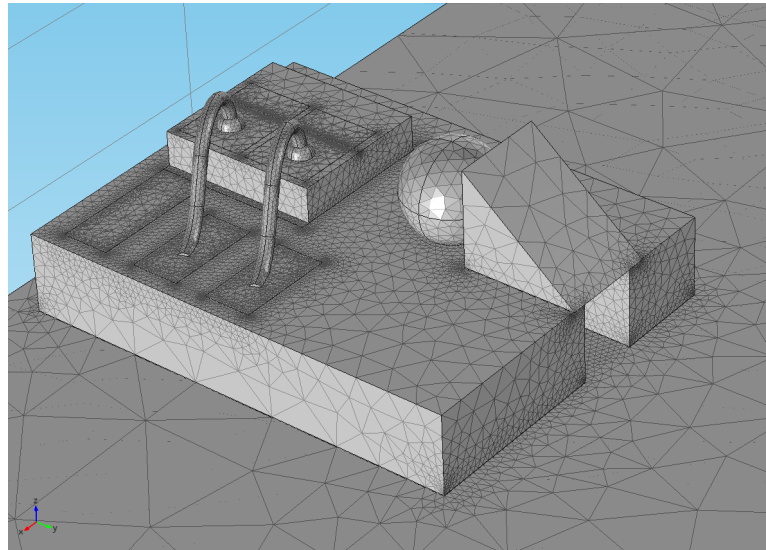


Figure 5.12: COMSOL mesh of micro-optical bench and components

defined by the Robin boundary condition

$$-\mathbf{n} \cdot (-k\nabla T) = h(T_\infty - T) \quad (5.4)$$

where \mathbf{n} is the normal vector for an exterior surface, T_∞ is the ambient temperature, and h is a heat transfer coefficient. This condition essentially states that the heat leaving the surface is proportional to the difference in temperature between the surface and the ambient air. The heat transfer coefficient h is an estimate of the efficiency of this heat removal. A full treatment of the derivation of heat transfer coefficients is beyond the scope of this thesis. However, for the purposes of estimating the thermal behavior of this system, a coefficient defined in part by the ratio of the surface area to the perimeter of a typical SOI chip was used. As will be seen later, convection cooling does not serve as the primary method for removing heat, so this estimate sufficed. The second type of boundary condition was to simply treat the temperature of one of the external surfaces as a constant. This condition was used to approximate the behavior of a Peltier active thermo-electric cooler (TEC).

Given these boundary conditions, a steady-state solution can be found when $\frac{\partial T}{\partial t} = 0$. COMSOL searches for this solution through an iterative process that seeks to minimize the left-hand side of (5.3). In order to do this, a model of a laser, micro-optical bench and SOI chip was created in COMSOL. The geometry of this model was defined in terms of standard COMSOL primitives and transformations, and the thermal properties of the materials (ρ , C_p , k) were sourced from a public reference [3] as well as the data sheet for the epoxy [44].

Care must be taken when defining structures with thin layers in COMSOL, such as

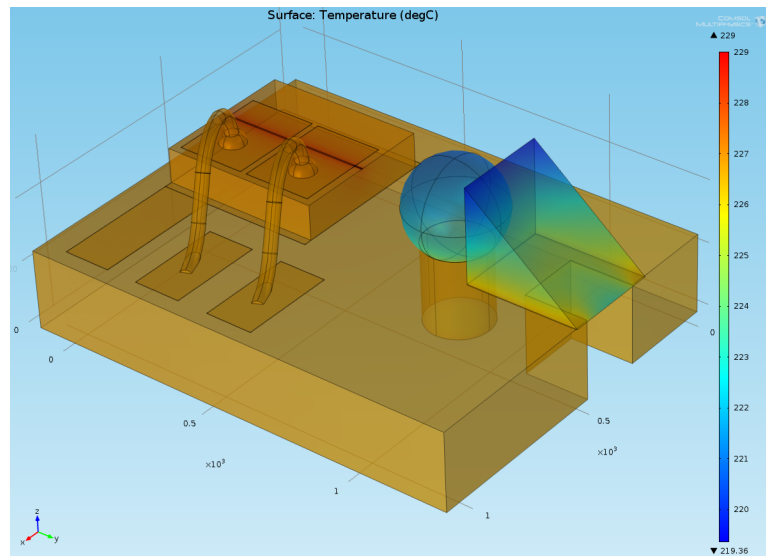


Figure 5.13: Simulation results of micro-optical bench in air showing overheating

the epoxy bonding layers and the electrical tracks. In order to discretize a model, COMSOL divides it into tetragonal 3D elements in a process called “meshing.” If a default meshing strategy is applied to thin features, an unnecessarily large number of mesh elements will result, wasting both memory and computation time. There are two strategies that can be applied to avoid this problem. The first strategy is to define a custom mesh, whereby different domains in the geometry have different meshing parameters. For example, the thin layers can have a “very coarse” mesh applied to them. On the other hand, certain features—especially round features—may need a finer mesh in order for the elements to match properly at boundaries, such as where the ball lens meets the round hole of the micro-optical bench. Fig. 5.12 shows the results of this meshing strategy as applied to a model of the micro-optical bench with a laser and the substrate epoxy-bonded to an SOI chip.

The other strategy is to remove the very thin layers from the geometric portion of the model and add them as “Thin Thermally Resistive Layers” in the thermal portion of the model. This allows the specification of the thickness and bulk thermal conductivity of the layer without having to include it in the meshing process and results in a more uniform mesh of the remaining components.

The first simulation to be performed was of the micro-optical bench and laser without the inclusion of the target SOI chip. This provided insight into the thermal behavior of the system during an active alignment, before the micro-optical bench is bonded. A relatively low heat source of 40 mW in the active region of the laser was used to simulate laser operation not far above threshold. As can be seen from the results in Fig. 5.13, significant overheating occurs, with the active region reaching a temperature of 229 °C in the steady state. In reality, this temperature would not be reached as most semiconductor lasers would suffer catastrophic damage before

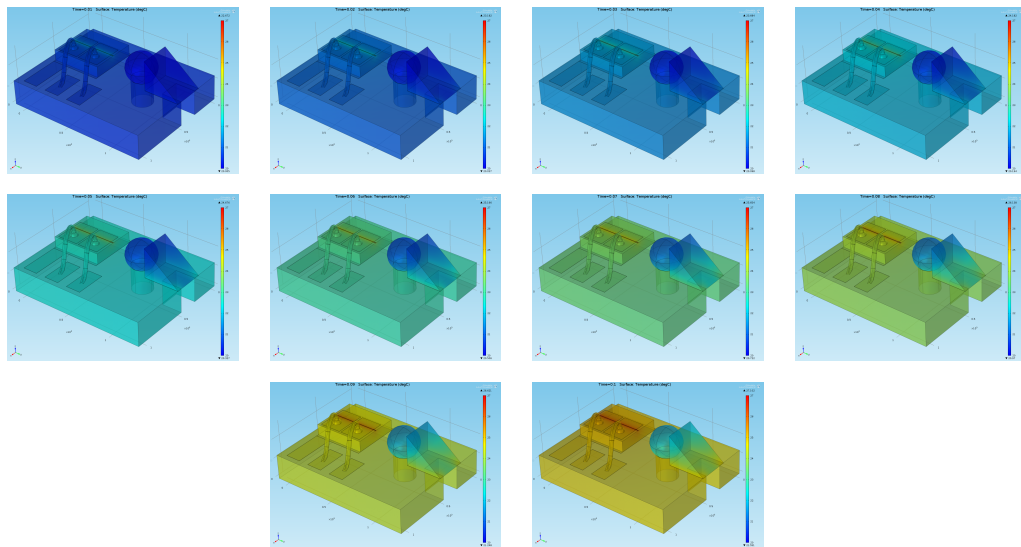


Figure 5.14: Heating of micro-optical bench in 10 ms intervals, indicating that pulses as wide as 100 ms can be used to power the laser during active alignment to grating coupler

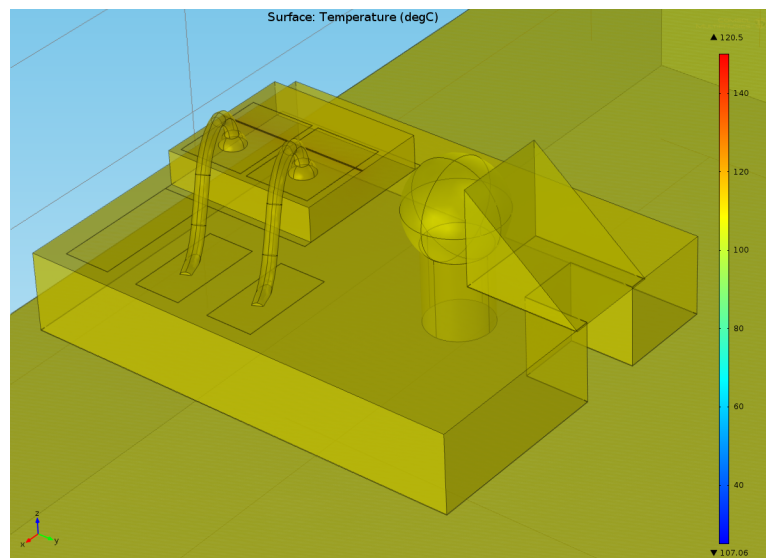


Figure 5.15: Simulation results of micro-optical bench on chip with passive cooling

reaching this point, and the epoxy holding the optics would fail as well.

However, what this simulation does indicate is that active alignment will need to be performed not by operating the laser in a CW mode, but instead in a pulsed mode. A time-dependent simulation in COMSOL (Fig. 5.14) gives an estimate that the laser can be pulsed up to 100 ms without the active region heating more than 10 °C so long as sufficient cooling time is allowed between pulses. In an actual application, the pulse width and period will need to be tuned for an individual laser to maximize measurable power while minimizing heating and preventing damage to the laser and micro-optical bench.

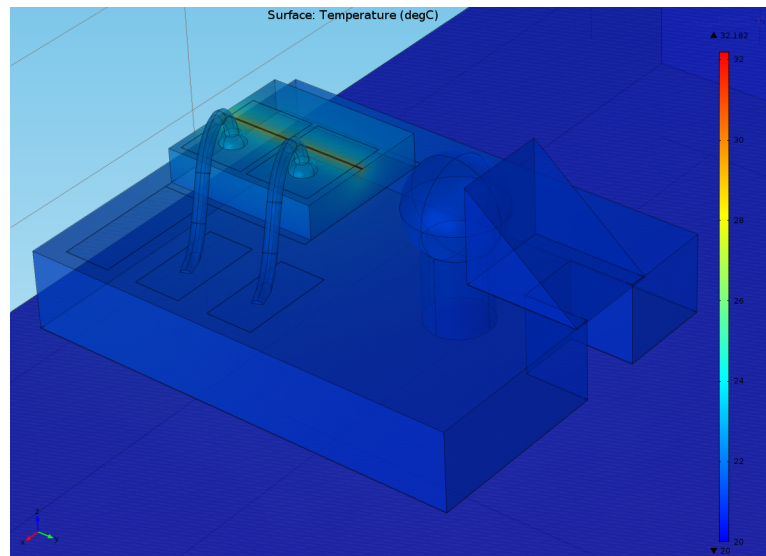


Figure 5.16: Simulation results of micro-optical bench on chip with TEC set at 20 °C

The next case to consider is when the micro-optical bench and laser are bonded to an SOI chip. A simulation of this was performed, this time with the laser running at full power. A rough estimate for the heat generated from the active region of a semiconductor laser was calculated by considering a drive voltage and current of 2 V and 100 mA respectively with all power given over to heat. As such, the Q in (5.3) for the active region was set to 200 mW, and the results are shown in Fig. 5.15.

In this case, the active region of the laser reaches a maximum of 120 °C. This is much lower than the previous case because the SOI chip serves as a heat sink and spreader for the heat that passes from the laser into the AlN substrate. The thermal conductivity of the SOI chip is not as high as that of AlN, but still high enough to provide significant transmission of the heat. Passive convective cooling is then able to remove more heat from the increased surface area of the chip. The passive cooling could be further improved by placing the chip on a copper heat sink with fins to increase the surface area available for the convective cooling. Such a design would serve well for a low power laser.

However, for higher-power lasers and lasers that need very stable temperatures for intended operation, active cooling must be considered. In order to do this, the previous simulation was modified so that the boundary condition at the bottom of the SOI chip was set to a fixed temperature value of 20 °C. This approximates an SOI chip attached to a Peltier cooler using epoxy with a very high thermal conductivity. The results of this simulation are shown in Fig. 5.16, which shows a maximum temperature in the active region of the fully-driven laser of 32 °C. This temperature is quite suitable for the efficient operation of a semiconductor laser and thus validates the thermal design of the micro-optical bench.

5.2.4 Electrical Design

Not only was AlN chosen as the substrate material for its desirable thermal properties, but also for its superior electrical performance. The electrical permittivity of AlN has long been known to be stable at high frequencies desired for electrical modulation [52–54] with recent measurements showing a stable value of 8.47 at as high as 100 GHz [55]. With this stable value, it is relatively simple to design a broadband transmission line that can be used to deliver a radio-frequency (RF) electrical signal to the laser for the purposes of direct modulation. With the lower surface of the micro-optical bench coated with gold and connected as a ground plane, the geometry of a microstrip line (MSL) on the top surface can be calculated using the procedure given in [56], which yields a track width of 274.5 μm for a characteristic impedance of 50 Ω .

Similarly, a G-S-G coplanar waveguide (CPW) transmission line can be included with only top metallization of the micro-optical bench. The geometry of this transmission line for a desired impedance can be derived from the formulae in [57], yielding the expression

$$\frac{w}{g} = \frac{1}{2Z_0\epsilon_0c\sqrt{2(\epsilon_r + 1)}} \quad (5.5)$$

where w is the width of the signal track between the ground planes, g the separation of the ground planes, Z_0 the characteristic impedance, c the speed of light, and ϵ_r and ϵ_0 the relative and vacuum permittivities respectively. The gap then between the signal track and the ground planes is simply $\frac{g-w}{2}$. For the 150 μm track width in the mechanical design, this expression yields an 11.7 μm gap width, which is too small for the processing capabilities of the substrate manufacturer. Instead, the signal track would need to be widened to at least 323 μm , with larger values preferable so as to mitigate the effects of manufacturing tolerances.

Both of these designs are given as a heuristic and would need to be validated using a full-wave electromagnetic simulator such as Ansys HFSS. The effects of track thickness are neglected in the CPW case, and the full dielectric response of the surrounding air is neglected in both cases, and so adjustment may need to be made according to the results of such a full-wave simulation.

5.3 Conclusions

The design process for a micrometer-scale optoelectronic system has been outlined, with a micro-optical bench intended for hybrid integration of discrete lasers with SOI photonic integrated circuits given as an example. This example illustrated the

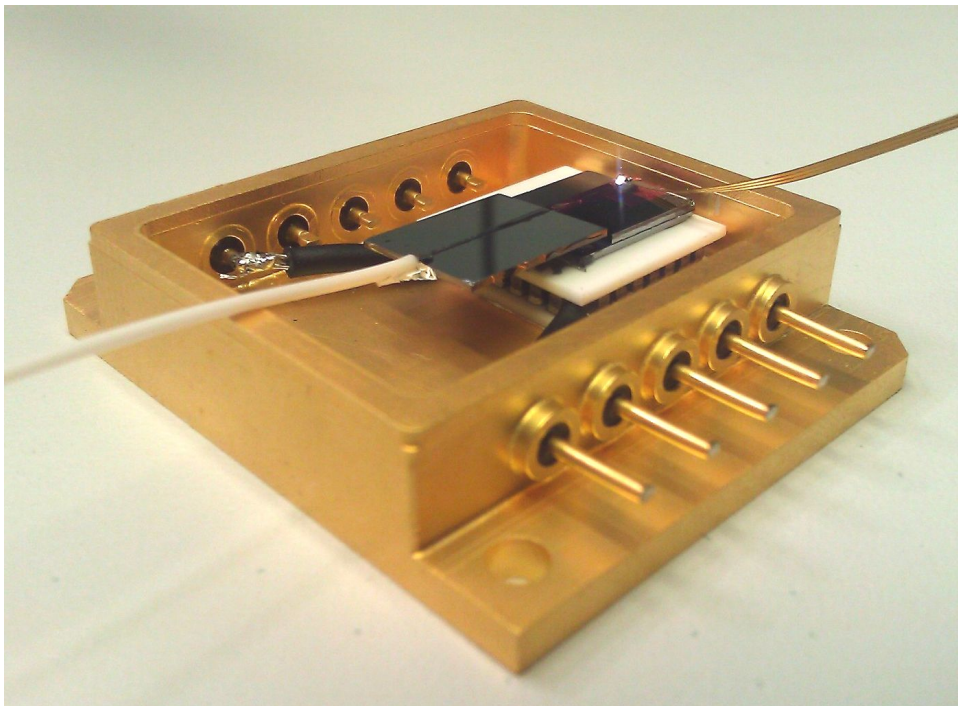
optical and mechanical design steps as the primary parts of realizing a working system. Furthermore, it showed how the various steps of the design can feedback to one another and how the potential exists for multiple iterations of the design process as later steps inform restrictions and aspects of performance of the previous steps.

Despite the current focus on optical and mechanical design, in future very-highly-integrated systems such as enabled by the SOI platform, the thermal design will increasingly come to the forefront. Rather than just verifying a stable performance, additional thermal design will be required. Heat generated by lasers integrated with SOI have the potential to seriously impact the performance of sensitive nanophotonic devices such as silicon ring resonators and arrayed waveguide gratings (AWGs). Either athermal devices and design practices will need to be implemented for SOI, or a very deliberate understanding and control of heat and its distribution in a design will need to be implemented.

Furthermore, as CMOS logic is integrated with SOI photonics, the impact of heat generated by transistors will become increasingly significant. This additional heat source will impact the performance of lasers, and the dynamic nature of the heat generation will create significant challenges to thermal design. Strategies for heat isolation and removal will be necessary to fully realize this potential.

Chapter 6

Implementation and Testing of Hybrid Integration Technology for Lasers



6.1 Introduction

This chapter will detail the process necessary to bring the micro-optical bench from concept to reality. A detailed set of steps will enumerate the machines, materials and operations necessary to construct the micro-optical bench assembly and integrate it with an SOI photonic integrated circuit. Following this, verification and performance tests will be presented showing proven operation and efficient performance with both single-frequency and tunable lasers.

6.2 Construction of the Micro-Optical Bench Assembly

The micro-optical bench design defines a set of steps that must be performed to construct the micro-optical bench assembly. Mechanical factors, such as the need for the laser die to be attached to the micro-optical bench substrate before wire bonding can be performed, play a primary role in determining the order in which these construction steps can take place. However, there are additional thermal restraints which significantly impact this ordering as well. High temperature processes must in general precede lower temperature processes, and the UV cure epoxy in particular has a failure temperature of 120 °C, which itself cannot be reached until after an aging process. With these considerations accounted for, a summary of the resulting process order and the maximum temperatures reached in each step is given in Table 6.1.

The first stage of construction is the die bonding process by which the laser die is attached to the micro-optical bench substrate (Fig. 6.1a). A die bonding machine was used, which allows for the manual alignment of the die along the edge of the solder reflow pad. In the first step of this process, the micro-optical bench substrate was placed on a vacuum chuck heating plate with a standby temperature of 250 °C.

Table 6.1: Schedule of Temperatures for micro-optical bench Construction

Process	Max. Temp. (°C)
Die Bonding	340
Wire Bonding	120
Thermocompression Bonding	250
UV Epoxy Precuring	—
UV Epoxy Aging	60
Thermal Adhesive Curing	—
Silver Epoxy Curing	100

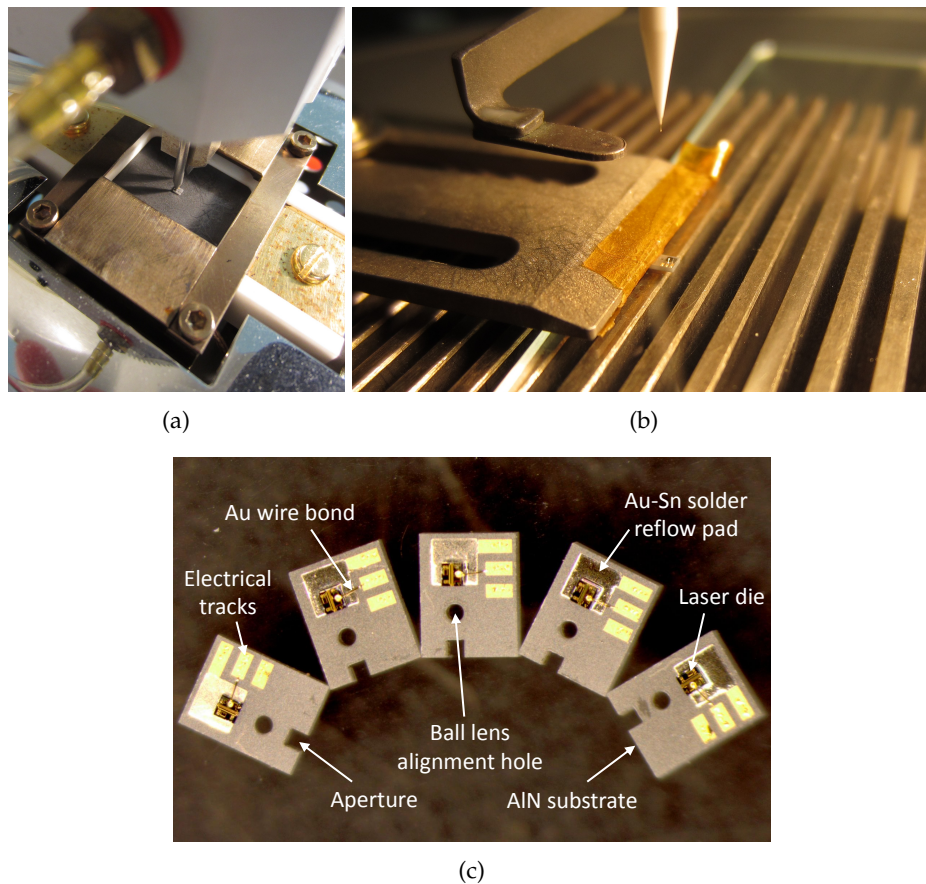


Figure 6.1: (a) Laser die being bonded to micro-optical bench substrate (b) Wire bonding laser contacts to substrate tracks and placing ball bonds (c) Batch of micro-optical benches after die and wire bonding

Then, the laser die was lifted with a vacuum pick-up tool and brought above the substrate. Fine rotation controls allowed for ensuring the die was parallel to the solder pad edge, and a high magnification microscope aided in aligning the active region with the center of the ball lens hole. When the die was aligned and in place, a nitrogen cover gas was applied. The heating plate temperature was then raised briefly to 340 °C, causing the solder to reflow then resolidify, fixing the laser die in place with an electrical connection formed between the laser cathode and the micro-optical bench substrate ground track.

Several methods of bonding are used in electrical integration of microsystems, including thermocompression and thermosonic bonding. With thermocompression bonding, heat and pressure are applied simultaneously to form a bond between two metal surfaces. With thermosonic bonding, ultrasonic energy is applied in addition to the heat and pressure. This allows lower levels of heat and pressure to be used.

Gold wires connections were formed between the laser anode pad or pads (in the case of the two-section laser) and the signal tracks on the substrate using a Kulicke

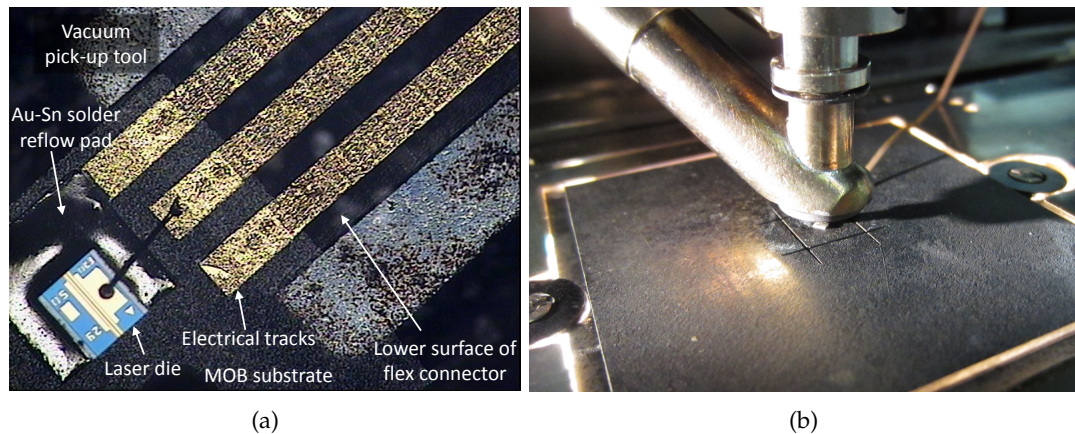


Figure 6.2: (a) Aligning flex connector electrical tracks to micro-optical bench electrical tracks (b) Thermocompression bonding in progress

& Soffa 4524 ball bonder (Fig. 6.1b). This bonding machine employs a thermosonic process to bond a gold ball connected to a wire to the laser pad. The wire is then extended to the micro-optical bench track and terminated with a wedge bond. A temperature range of 100 °C–120 °C was used for the bonding. In addition to the wires, several gold stud bumps were placed on the tracks near the edge of the substrate. These consisted of just the ball bond without the wire or wedge and were used to improve the quality of the thermocompression bonds in the next step.

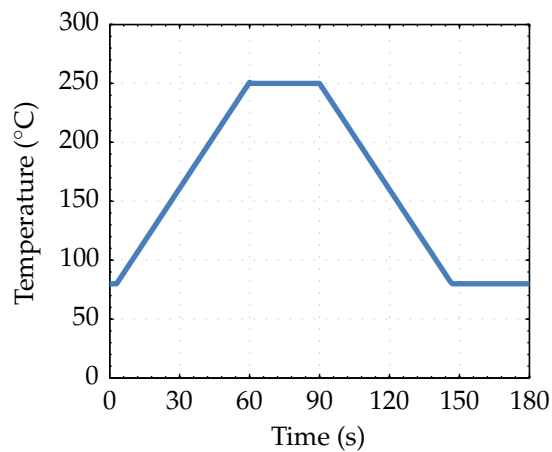
A Finetech FINEPLACER Lambda semi-automatic flip-chip system was used to perform thermocompression bonding between the flexible circuit connector and the micro-optical bench substrate tracks. This system can also be used to do thermosonic bonding as well as other bonding processes. The key function of the flip-chip process is to facilitate the precise alignment of the lower surface of one object with the upper surface of another before performing one of these processes.

The micro-optical bench substrate was placed on the vacuum chuck heating plate of the flip-chip system, while the flex connector was held by a heated vacuum pick-up arm. The flex connector had to be bent and oriented in such a way as to avoid contact with other parts of the system through the range of motion of the pick-up arm. If it were to hit any of these parts, the vacuum would be compromised and the flex circuit would fall out of position.

With the pick-up tool raised, a beam splitter allowed the top surface of the micro-optical bench and the lower surface of the flex connector to be imaged simultaneously and aligned with one another (Fig. 6.2a). Once alignment was completed, the pick-up arm was lowered and 10 N of force was applied (Fig. 6.2b). This was accompanied by heating of both the pick-up arm and lower heating plate from their standby temperatures of 80 °C according to the schedule shown in Fig. 6.3b. Active cooling was disabled for the pick-up arm, as the jet of air from the



(a)



(b)

Figure 6.3: (a) Finetech FINEPLACER Lambda flip-chip bonder (b) Heating schedule for thermocompression bonding

cooler would blow the flex connector out of place. Once the bonding was complete, the lower vacuum holding the micro-optical bench substrate was released and the substrate and flex assembly was lifted with the pick-up arm to verify the bond. Given a successful bond, the assembly was then removed from the pick-up arm. The bond was then further reinforced with UV cure epoxy to withstand handling during the rest of the construction process.

Finally, the optics were attached to the substrate to complete the micro-optical bench assembly. Approximately 0.15 nL of UV cure epoxy—about the size of a 50 μm cube—was applied along the rim of the ball lens hole. The ball lens was then placed in the hole manually and cured in place with 500 mW of UV light with a spectral range of 320 nm to 500 nm for 75 s, yielding a total curing energy of 37.5 J. Then, approximately 0.2 nL of epoxy was distributed around the top of the aperture, being careful not to fill the gap between the lower half of the ball lens and where the prism

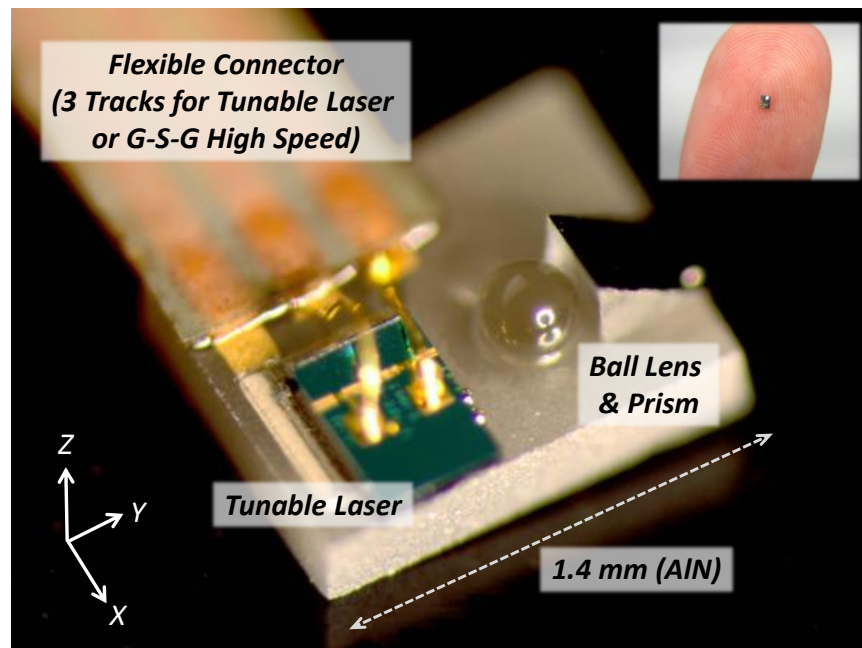


Figure 6.4: Micro-optical bench assembly with tunable laser (main) Size of micro-optical bench compared to index finger (inset)

is to be placed. The prism was then set on this epoxy and brought into physical contact with the ball lens. The rotation of the prism was fixed by visually aligning its thin edge parallel to the edge of the micro-optical bench substrate. Finally, the epoxy was cured with a longer cure time of 150 s for a total energy of 75 J. A completed micro-optical bench assembly with a two-section tunable laser is shown in Fig. 6.4.

6.3 Integration with the SOI Chip

For the purposes of testing and measurement, an SOI chip was prepared before integrating with the micro-optical bench assembly. The chip contained a simple straight waveguide, one end of which was coupled to a fiber using the planar packaging process described before. During this process, one fiber was aligned and epoxied over the output grating, whereas the fiber over the input grating was aligned but not epoxied. The working distance of the input fiber was maximized with respect to Fabry-Pérot reflections, and then the optical spectrum of the insertion loss from fiber to fiber was measured and recorded. This spectrum was obtained by measuring the spectrum of the superluminescent diode (SLD) input light and subtracting it from the output spectrum in the logarithmic scale. It represents the optical loss and wavelength variation of the input grating, waveguide and output grating and was used to normalize later results to isolate the performance of the micro-optical bench.

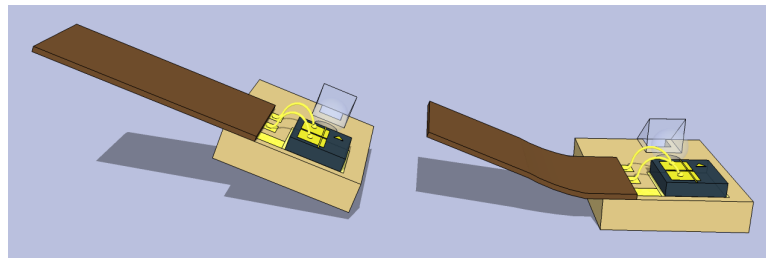


Figure 6.5: Flex connector bent down before contacting chip (left) Torque from bend aligns micro-optical bench flat on chip surface (right)

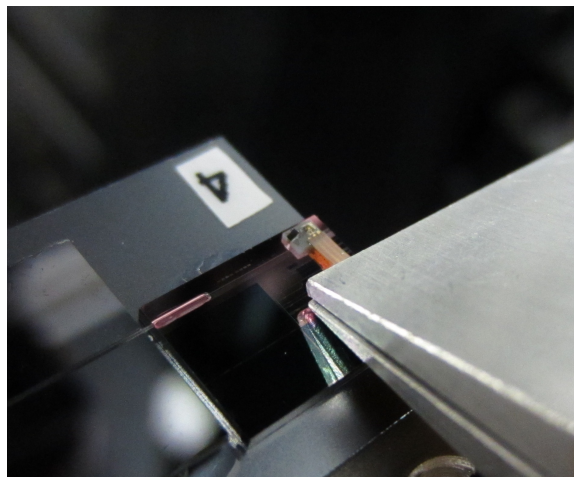


Figure 6.6: Micro-optical bench mounted in clamp during alignment

Once the chip and output fiber assembly was prepared, it was mounted on the vacuum chuck of the fixed sample stage of the waveguide alignment system (as shown previously in Fig. 3.3). The flex connector of the micro-optical bench assembly was then mounted in an electrically-insulated clamp (Fig. 6.6), which was itself attached to one of the motion stages of the system. The connector was mounted so that the micro-optical bench assembly was as close to the clamp as possible, minimizing any bending in the lateral directions, while at the same time still leaving some room for the connector to bend up and down and for the micro-optical bench to move without coming into contact with the clamp. This latter bending is important, as the assembly was mounted with the flex connector and micro-optical bench substrate bent slightly down, ensuring that when the micro-optical bench was placed in contact with the chip, the restorative torque of the bend caused the micro-optical bench to sit flat on the chip surface (Fig. 6.5). This process served as a simple self-alignment technique for both the pitch and roll of the micro-optical bench assembly.

With the micro-optical bench and flex connector mounted in the clamp, the laser was driven to allow for active alignment. The driving current was provided by a normal laser current source connected to a pulse generator. The pulsed operation was necessary due to the heating discussed in the previous chapter. For both the

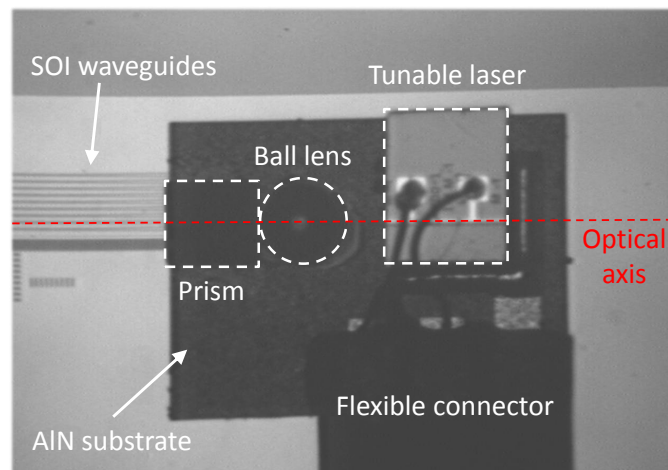


Figure 6.7: Overhead image from high-magnification IR camera showing micro-optical bench and components during alignment

two-section tunable laser and single wavelength Fabry-Pérot lasers packaged for testing, the pulse generator was set to produce $65\ \mu\text{s}$ pulses every $2.5\ \text{ms}$. These values were found by trial-and-error to give maximum output without damaging the lasers. Because the maximum high-precision sampling rate of the power meter was only $25\ \text{Hz}$ [58], it was set to run in continuous measurement mode rather than a triggered mode and allowed to average the power of the pulses over the $40\ \text{ms}$ sample period. This meant that the reading given by the power meter was not the actual peak power during the pulse, but it still provided a relative measure of the alignment of the micro-optical bench substrate over the grating. The output voltage of the pulse generator was chosen such that in the case of the Fabry-Pérot lasers the drive current was $20\ \text{mA}$, or just above threshold, and in the case of the two-section laser $100\ \text{mA}$ was divided between the two sections, representing a normal operating condition.

Once biased, the laser was then brought into contact with the chip, and a passive yaw alignment was performed using the straight waveguide and parallel lithographic features as a reference. This alignment was performed under a high magnification camera, and the active region of the laser, rather than the edge of the micro-optical bench substrate, was used to align to the lithographic features on the chip (Fig. 6.7). The micro-optical bench was then moved over the input grating until at least $0.5\ \mu\text{W}$ of optical power was detected at the output fiber, and then the automated features of the waveguide alignment system software were used to perform the rest of the active alignment process.

With power maximized, approximately $0.25\ \mu\text{L}$ of low-viscosity ($300\ \text{cP}$) epoxy was carefully dispensed at the lower edge of the micro-optical bench substrate opposite the grating. The epoxy was then allowed to distribute under the micro-optical bench substrate by capillary action. Once it had been suitably distributed, the epoxy was

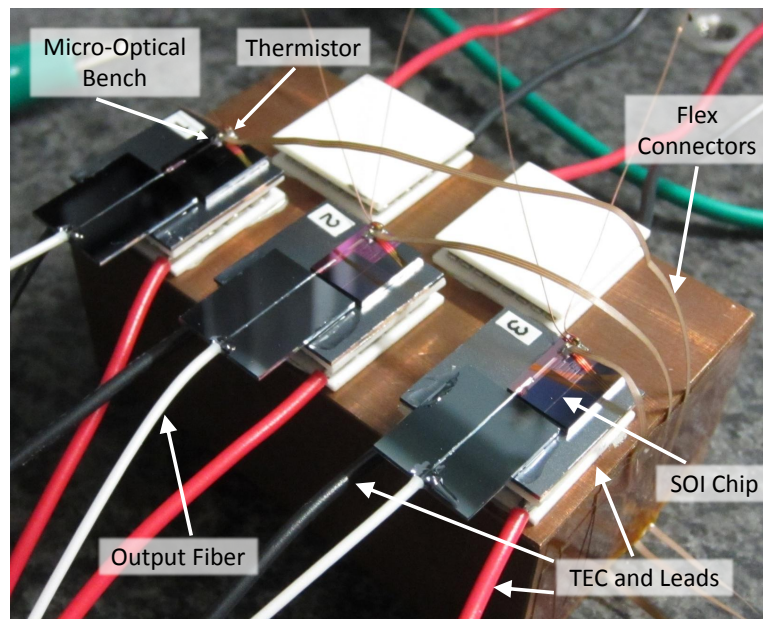


Figure 6.8: Integrated lasers with active temperature control and monitoring

cured with 500 mW of UV light applied from several directions over a period of 150 s, resulting in a total curing dose of 75 J.

With the cure complete, the flex connector was carefully removed from the clamp, and the vacuum chuck was turned off. The packaged laser and chip were then moved to a hot plate for an epoxy aging process, whereby the assembly was kept at or below 60 °C for a period of 12 h. After this aging process, the UV epoxy is completely cured, and can withstand future heating up to 120 °C.

For testing purposes, the packaged laser and chip were then mounted on a Peltier thermo-electric cooler (TEC) using thermal adhesive. A 1.4 mm 10 k Ω radial thermistor with a diameter of 0.8 mm was also affixed with thermal adhesive at the rear of the micro-optical bench so that the laser temperature could be monitored for controlling the TEC. Finally, the TEC was attached with thermal adhesive either in a butterfly-style metal case (as shown on the chapter cover) for demonstration or on a copper block (Fig. 6.8) for lab testing.

For the butterfly package, the TEC leads were soldered directly to case pins, whereas the thermistor leads were bonded using silver epoxy to a pair of smaller wires previously soldered to case pins. The silver epoxy then underwent a curing process at 100 °C. This is a lower temperature than normally used for silver epoxy curing and required a longer cure cycle, but such a temperature was required by the 120 °C temperature limit of the fully-cured UV epoxy.

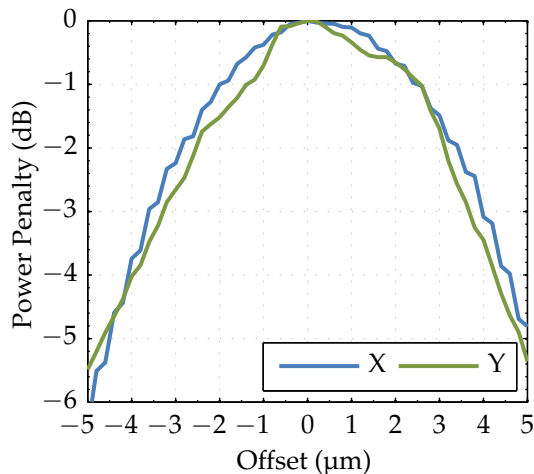


Figure 6.9: Lateral alignment tolerances of micro-optical bench placement

6.4 Tests and Measurements

6.4.1 Alignment Tolerance

The lateral alignment tolerances of the micro-optical bench were tested during the packaging process for the two-section tunable laser. The automated metrology features of the waveguide alignment system software were used to measure the power at the output fiber while moving the micro-optical bench in $0.5\ \mu\text{m}$ steps in two axes. The results of this test are shown in Fig. 6.9. The slight oscillations in the graph can be attributed to the way that the micro-optical bench was mounted. It was held with a small length of flex connector separating the rigid mount of the clamp from the actual micro-optical bench. As a result, the movement of the micro-optical bench was not absolutely rigid. However, it was sufficiently rigid for final alignment during the packaging process and also to produce these results.

The most important information drawn from these results is the approximately $4\ \mu\text{m}$ range over which the additional loss due to misalignment is less than 1 dB. Such a tolerance indicates that a passive process can be used in the alignment of the micro-optical bench, and thus this laser integration technology is suitable for mass manufacturing and wafer-scale processing.

6.4.2 Tunable Laser Spectrum

The tunable laser used in this research provides more than 10 nm of wavelength tuning using the Vernier effect [59, 60]. Such a tunable laser consists of two or more asymmetric optical cavities, or sections, divided by a slot or Y-coupler. Each section has a different mode spacing as a result of this asymmetry. Furthermore, these

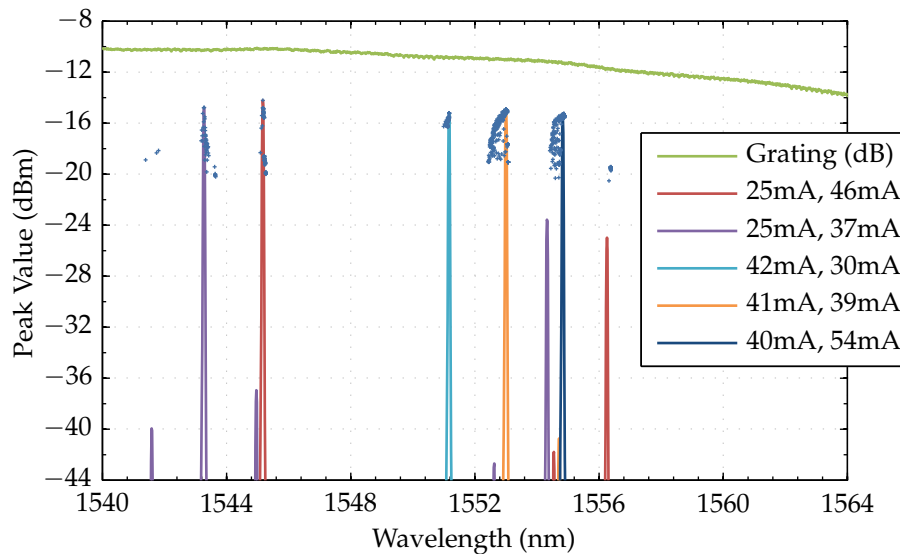


Figure 6.10: Peak values for various drive currents of packaged tunable laser including sample spectra

sections are electrically isolated from one another. By adjusting the drive current in a particular section, the optical spectrum of the modes in that section is altered slightly. When there is strong spectral overlap between a mode in all of the sections, the mode at that wavelength experiences gain throughout the entire laser cavity and results in a single narrow peak in the laser output. The different wavelengths where this overlap can occur then represent the various possible tunings of the laser.

Once integrated with the SOI chip, the tunable laser was characterized in an automated process driven by a computer running a LabView program. This program set the drive currents for the two sections of the laser and measured the output optical spectra using an optical spectrum analyzer (OSA). The range of currents consisted of all combinations of values between 25 mA and 55 mA in 1 mA intervals. After setting a particular pair of currents, the program delayed for several seconds to allow the temperature controller and laser output to settle. Then, an OSA sweep was triggered and the results were transferred to the controlling computer to be saved.

The initial analysis of this data involved using a LabView program to build a data set containing all the peak powers and wavelengths of the tunings. This data set is plotted in Fig. 6.10. The full spectrum of five of these tunings is overlaid on the graph to illustrate the quality of the output in terms of line width and mode singularity of the tunings. These are not meant to replace a proper delayed self-heterodyne measurement process for line width measurement, but to instead provide a rough approximation and to verify the absence of cross-talk between tunings.

The insertion loss spectrum of the gratings is also overlaid on the graph. This is to indicate expected variations in peak power between the tunings and give an indication of the flatness of the spectrum of the laser without packaging. However, in this case the actual coupling efficiency of the micro-optical bench packaging process could not be determined. This is because the divergence angles and unpackaged power of the laser were not provided. Furthermore, the values plotted were not normalized against a power meter reading and should only be taken as relative values.

Another LabView program was then used to analyze the saved data and identify data sets with side mode suppression ratios (SMSR) above a certain threshold. 77 tunings were found to have an SMSR greater than 32 dB, although these tunings cluster closely around two wavelengths at approximately 1551.1 nm and 1552.8 nm. When the threshold was reduced to 30 dB, 180 tunings were found, and an additional cluster around 1554.8 nm appeared. In total, more than 55 % of the tunings had an SMSR greater than 20 dB

6.4.3 Coupling Efficiency

The coupling efficiency of the laser integration process was measured by packaging several Fabry-Pérot lasers provided courtesy of Eblana Photonics. These lasers were individually characterized by Eblana and provided between 30 mW and 34 mW output power at a drive current of 100 mA. Also, they had nominal beam divergences of 30° and 24° respectively for each axis in the far field.

In order to accurately gauge the performance of the physical micro-optical bench assembly versus the design, the Zemax simulation had to be modified to specify these divergences and rerun to determine a new insertion loss value. However, the divergence angles were specified in terms of the full width at half maximum (FWHM) of the beam power, whereas Zemax specifies divergence angles as the half-angle at $1/e^2$ of the beam power or $1/e$ of the beam field. The FWHM value can be converted to the value required by Zemax using the following relationship

$$\tan \theta = 1.699 \tan \frac{\theta_{FWHM}}{2}. \quad (6.1)$$

With this value in place, Zemax returns a theoretical insertion loss from laser to grating (not including the loss of the grating itself) of 3.38 dB.

To determine the actual loss of the micro-optical bench, several measurements were taken with each laser biased at 100 mA and the temperature controller set at 20 °C. The first measurement was a reading of the total power from an optical power meter. Then, the output fiber was connected to an OSA, and the spectrum of the

output power was measured. As the resolution bandwidth of the OSA was 0.05 nm and the measurements were taken at 0.01 nm intervals, there was some overlap in power between measurements. This was corrected for by normalizing the optical spectrum against the total measured power using the following relationship

$$P(\lambda) = \frac{P_o}{\sum P_{OSA}(\lambda)} P_{OSA}(\lambda) \quad (6.2)$$

where $P(\lambda)$ is the normalized power at each wavelength, P_o is the total optical power as measured by the power meter and $P_{OSA}(\lambda)$ is the power at each wavelength as measured by the OSA. Once this normalization was complete, the losses due to the gratings and waveguide were then removed. This was done by taking the optical spectrum of the losses between input grating and output fiber measured during the fiber packaging of the chip and subtracting it from the normalized power $P(\lambda)$ in the logarithmic scale.

At this point, a representation of the power at the input grating had been obtained. This must then be compared to the total power emitted by the laser as measured by the manufacturer to determine the contribution of the micro-optical bench and its optics to the coupling efficiency. In order to do this, the power at the input grating is converted to the linear scale (from dBm to watts) and summed across all wavelengths. The ratio of this result and the laser power then represented the measured insertion loss of the micro-optical bench.

The result of measuring several lasers was an insertion loss of (3.89 ± 0.43) dB with a best-case insertion loss of 3.36 dB. These measurements were also consistent when repeated at a temperature setting of 25 °C. One measurement of approximately 7 dB insertion loss was discarded due to scratches on the laser active region that occurred during wire bonding.

It should be noted that the best case insertion loss is actually better than the simulated insertion loss. This occurred because for the particular divergence angles of these lasers, the optimum working distance is different than for the 10° and 30° angles used in the original design. In the 10°/30° design, the optimum working distance was 171 μm, whereas for these particular lasers the optimum was 166 μm. At this working distance, the simulated insertion loss was only 3.19 dB. The discrepancy between loss values is quite small, so the general purpose design can be reused for small runs and demonstrators of a variety of laser geometries, and yet the working distance is also a single factor that can be easily optimized for production runs where 10 000 or more of an individual laser geometry will be packaged.

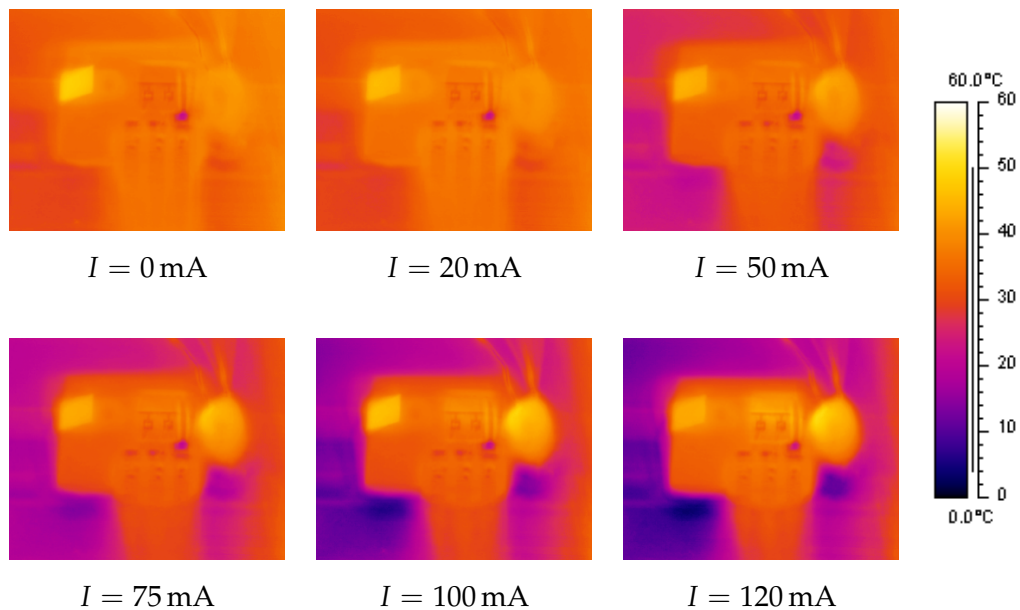


Figure 6.11: Steady-state thermal measurements of micro-optical bench at various drive currents

6.4.4 Thermal Imaging

A FLIR Merlin thermal camera was used to measure the steady-state and dynamic thermal response of the micro-optical bench assembly integrated with a silicon photonic chip. For these tests, the fully-packaged demonstrator shown on the chapter cover was used. The steady-state response of the micro-optical bench assembly was measured first, and the results for several different drive currents are shown in Fig. 6.11. In each case, the temperature was stabilized by a Peltier cooler under the silicon chip and supporting substrate that was driven by a separate temperature controller unit. Feedback to this unit was provided by a thermistor placed directly behind the micro-optical bench using a highly thermally-conductive epoxy.

The results of these measurements should not be taken to represent absolute temperatures, nor should the relative temperatures of features of different materials be considered reliable. This is due chiefly to different emissivities of different materials as well as the reflective properties of certain materials. For example, the gold surfaces have a very low emissivity, and thus the active region and bond pads of the laser and micro-optical bench appear as low temperatures, while their horizontal orientation also prevented reflection of thermal radiation from other parts of the system. On the other hand, the non-horizontal reflective surfaces of the prism coating and the thermistor glass package reflected such extraneous thermal radiation. Furthermore, the thermistor glass reflected infrared light from the back facet of the laser, the magnitude of which can be seen to increase with the increase

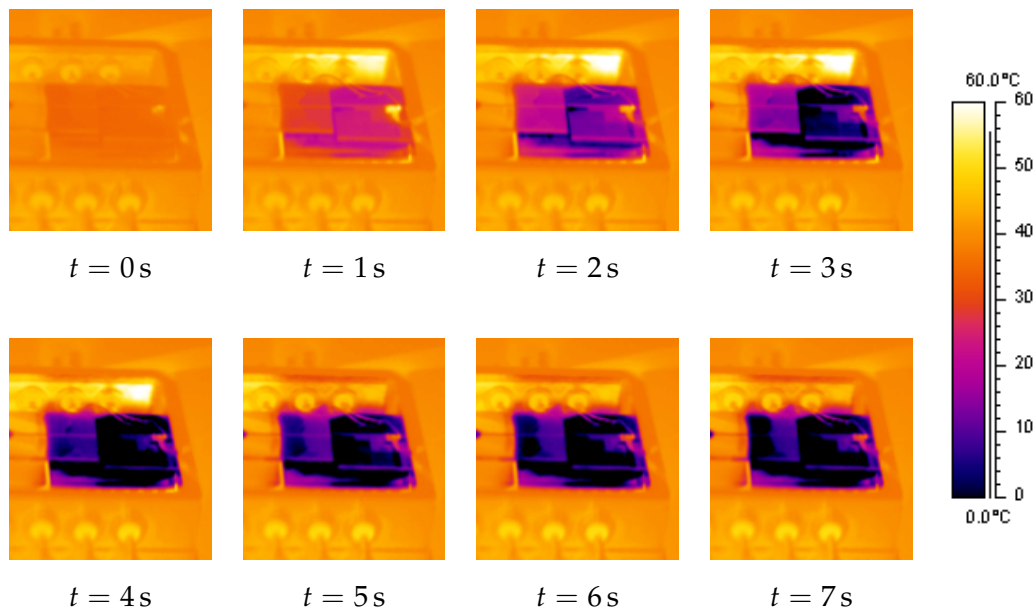


Figure 6.12: Dynamic thermal response of micro-optical bench and silicon chip showing long thermal time constant suitable for high-speed direct modulation

in current.

The most telling areas to observe are the laser die near the active region, the AlN bench itself and the surrounding silicon chip area. For each increase in current, the die temperature went up, whereas the AlN bench temperature went slightly down and the surrounding chip area went down in a more pronounced fashion. The temperature shown for the surrounding chip area is actually more indicative of the thermo-electric cooler temperature as the silicon wafers used for the chip and underlying substrate have a low emissivity and are fairly transparent in infrared at the temperatures in question [61]. Taken as a whole, these results represent the expected behavior, with a non-divergent temperature response validating the thermal portion of the design.

The dynamic response in Fig. 6.12 gives an idea of the performance of the thermal design. This shows a settling time of between 3 s to 4 s. There is a small amount of overshoot at $t = 4$ s, but this is compensated for by $t = 5$ s and the temperature remains steady after that point. The temperature reading of the surrounding case should be neglected, as this was a reflective metal surface. Also, as mentioned before, the temperature shown in the chip area is actually an indication of the temperature of the underlying thermo-electric cooler due to the emissivity of silicon and its transparency in the infrared range. Even so, the temperatures given should not be considered exact.

For the case of a directly-modulated laser operating at telecommunications data rates, these measurements indicate that a settling period would be needed when

initially turning on the laser. However, after this point the temperature would remain steady given a data stream with fairly fixed statistics. This is because the thermal time constant evident from this measurement is orders of magnitude greater than the width of an, e.g., 10 GHz data pulse.

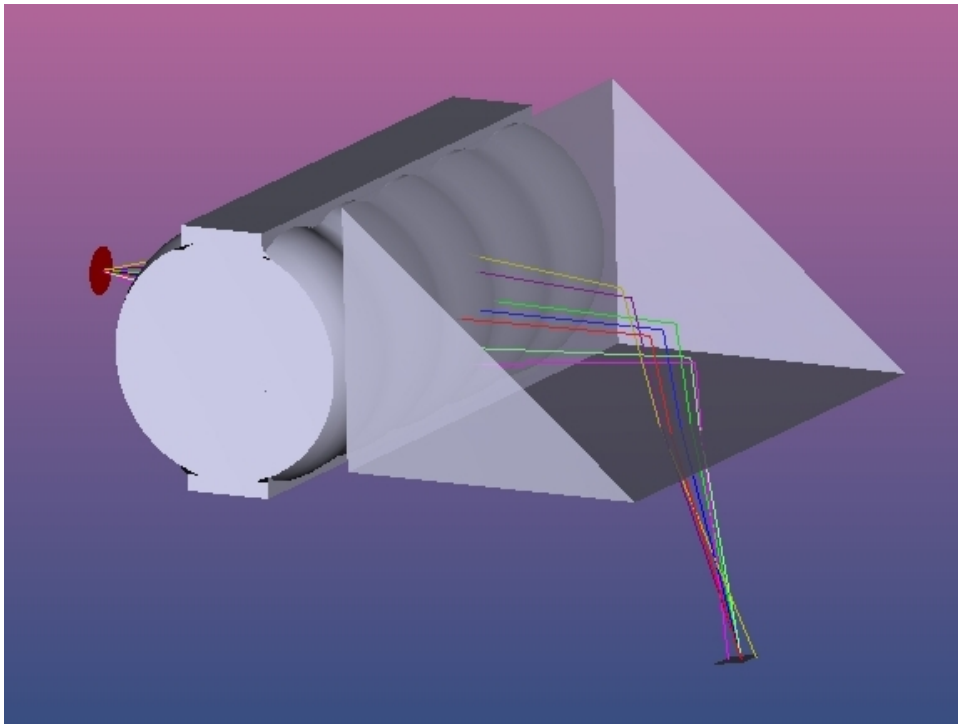
On the other hand, if the data statistics change, as in the case of a long period of inactivity, then another period of settling will be required. This can be avoided by modulating the laser with a dummy data stream during such periods, although this decreases the overall energy efficiency of the system. Still, there is a net energy savings over a system where the laser is run in continuous-wave operation and modulation is performed by interference or absorption.

6.5 Conclusions

In this chapter, the laser integration design of the previous chapter was constructed and tested. It was shown to have alignment tolerances suitable for passive alignment and wafer-scale assembly and to be thermally stable. It also resulted in measured coupling efficiency consistent with the design simulations and suitable for use with low-loss grating couplers. In particular, the stable single polarization of the laser removes the necessity of using lossier 2D gratings. Instead, 1D gratings with demonstrated losses as low as 0.75 dB [21] can be combined with this technology to couple light into submicrometer photonic circuits with better than 40 % efficiency. Further improvements, including the use of antireflective-coated optics and aspherical lenses in the place of ball lenses, will improve this coupling efficiency even further.

Chapter 7

Conclusions and Further Work



7.1 Summary

In this thesis, two new technologies were introduced. First, a novel process for planar fiber packaging was proposed and developed. This process was shown to be extensible to fiber arrays and to be compatible with passive-alignment-based wafer-scale assembly. Innovations made when extending the original process for high-performance, high-yield multiple fiber packaging have led to the submission of an EU patent that will be accompanied by a future US patent submission. The demand for this technology has already led to its inclusion in the ePIXfab silicon photonics foundry and to collaborations with a wide range of European research institutions developing the next generation of silicon photonic devices and highly-integrated systems. Projects using this technology include the EU FP7 projects ESSenTIAL [62], PLAT4M [63] and FABULOUS [64]. Design rules for leveraging this packaging process in the design flow of future photonic integrated circuits have been included in PhoeniX Software's MaskEngineer commercial software product as well [65].

The planar fiber packaging process went on to inspire a novel technology for the hybrid integration of photonic sources with submicrometer silicon photonic systems. The micro-optical bench design at the core of this technology possesses many desirable optical, mechanical, thermal and electrical properties. The optics enable low-loss coupling to SOI waveguides using single-wavelength and tunable laser sources, as well as a variety of other light sources. The mechanics of the micro-optical bench construction are based on a set of self-alignment and passive alignment processes, and the final integration of the assembly with an SOI system can be performed at wafer scale using industry-standard pick-and-place machinery. The thermal characteristics of the design are stable, and it is electrically suited to the packaging of high-speed directly-modulated lasers with low radio frequency (RF) losses and reflections. A comparison between this laser integration technology and other published technologies is summarized in Table 7.1.

Significant interest has already been shown in these packaging and integration technologies, yet further enhancements are possible based on the foundation established in this thesis. Designs for several of these enhancements will be outlined in the following sections. These designs will need to be verified scientifically through construction and repeated testing, but the reliability of the correlation between the design and simulations and the measured results has already been demonstrated repeatedly throughout this work.

	Bookham Technology [36]	Kotura [37]	VTT [35]	Fujitsu [38]	Luxtera [21, 40]	Tyndall
SOI type	Thick ridge	Thick ridge	Thick ridge	Thin ridge	Thin strip	Thin strip
Coupling method	Direct end	Direct end	Direct end	Inverse taper	Grating	Grating
Alignment type	Self	Active	Passive	Passive	Self (lens) Passive (lid) Active (final)†	Self (lens) Self/passive (prism) Active (final)†
Optical isolator	No	No	No	No	Yes	Compatible
Aspherical/asymmetric lenses	N/A	N/A	N/A	N/A	No	Yes
Compatible with laser arrays	Yes	Yes	Yes	Yes	No	Yes
Laser/source type	SOA + Bragg	SOA + Bragg	Any	SOA + Bragg	Any	Any

†Final alignment demonstrated with active alignment, but compatible with fast passive alignment

Table 7.1: Comparison of Hybrid Integration Technologies for SOI

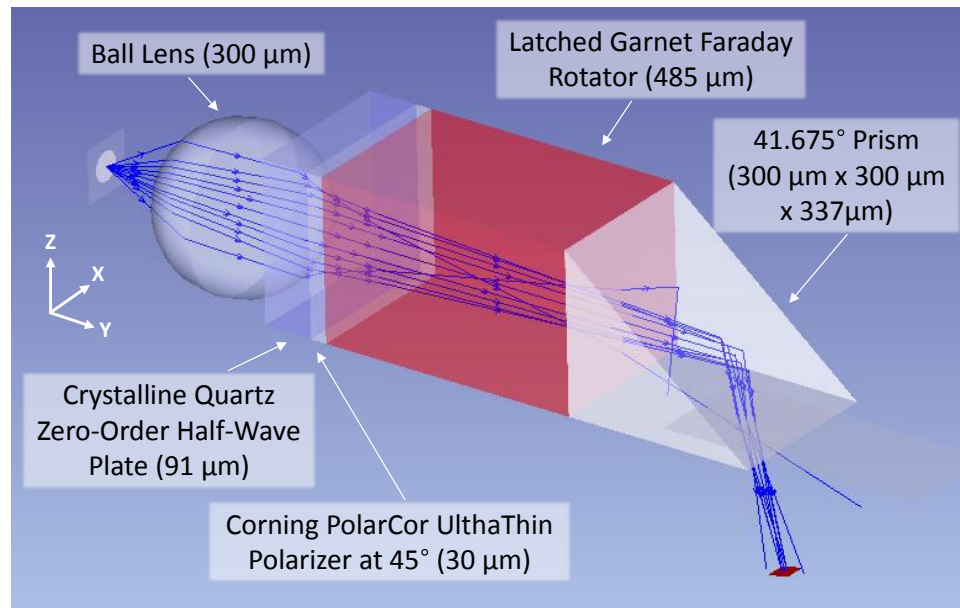


Figure 7.1: ZEMAX model of micro-optical bench with integrated isolator

7.2 Polarization-Dependent Isolator

One common feature of packaged lasers is an integrated optical isolator. This isolator prevents optical feedback generated elsewhere in a photonic system from coupling into the laser and disturbing the stability of its operation. For general systems, an isolator designed to operate independent of polarization is required. However, due to the fact that a 1D grating coupler will only efficiently couple one polarization for both input and output, a simplified polarization-dependent isolator design can be used.

A schematic of this design is shown in Fig. 7.1. It consists of three different materials bonded together with thin layers of epoxy. The first is a half-wave plate, which provides a reciprocal polarization rotation based on the birefringent properties of crystalline quartz. This is followed by a thin linear polarizer made of dichroic glass. The final and most crucial piece is a non-reciprocal polarization rotator (a so-called Faraday rotator) made of a latched bismuth-doped yttrium iron garnet (Bi:YIG). Latched garnet differs from garnet used in other polarization rotators due to the fact that it does not require the use of a separate permanent magnet. The magnetization of the material is set by raising it to its 185 °C Curie temperature and applying a magnetic field [66]. When the material is cooled, this magnetization remains fixed.

The operation of the isolator can be described in terms of Jones calculus. Each component can be described by a Jones matrix, where the half-wave plate, polarizer and Faraday rotator are given by the following three matrices respectively,

$$\mathbf{M}_{\lambda/2} = \begin{bmatrix} \cos 2\theta & \sin 2\theta \\ \sin 2\theta & -\cos 2\theta \end{bmatrix} \quad (7.1)$$

$$\mathbf{M}_{\mathbf{P}} = \frac{1}{2} \begin{bmatrix} 1 & 1 \\ 1 & 1 \end{bmatrix} \quad (7.2)$$

$$\mathbf{M}_{\mathbf{R}} = \begin{bmatrix} \cos \varphi & -\sin \varphi \\ \sin \varphi & \cos \varphi \end{bmatrix} \quad (7.3)$$

where θ is the angle between the X axis and the fast axis of the half-wave plate and φ is the angle specifying the amount of rotation induced by the Faraday rotator, with counterclockwise taken to be positive in both cases. The orientation of the polarizer is fixed at $+45^\circ$ from the X axis, and this is reflected in the constant value of its Jones matrix.

When light is passing from the laser to the grating, it experiences a polarization transformation defined by the multiplication of the previous matrices. This yields the following matrix.

$$\mathbf{M}_{\mathbf{R}}\mathbf{M}_{\mathbf{P}}\mathbf{M}_{\lambda/2} = \begin{bmatrix} (\sin 2\theta + \cos 2\theta)(\cos \varphi - \sin \varphi) & (\sin 2\theta - \cos 2\theta)(\cos \varphi - \sin \varphi) \\ (\sin 2\theta + \cos 2\theta)(\cos \varphi + \sin \varphi) & (\sin 2\theta - \cos 2\theta)(\cos \varphi + \sin \varphi) \end{bmatrix} \quad (7.4)$$

Setting θ to $+22.5^\circ$ and φ to -45° and multiplying this matrix by the Jones vector for X-polarized light, the following result is obtained.

$$\mathbf{M}_{\mathbf{R}}\mathbf{M}_{\mathbf{P}}\mathbf{M}_{\lambda/2}\mathbf{x} = \begin{bmatrix} 1 \\ 0 \end{bmatrix} \quad (7.5)$$

This means that for the X-polarized light from the laser passing through the isolator, there is no net effect. However, in the case of light passing from the grating toward the laser, the matrices are applied in the opposite order, yielding the following matrix.

$$\mathbf{M}_{\lambda/2}\mathbf{M}_{\mathbf{P}}\mathbf{M}_{\mathbf{R}} = \begin{bmatrix} (\sin 2\theta + \cos 2\theta)(\cos \varphi + \sin \varphi) & (\sin 2\theta + \cos 2\theta)(\cos \varphi - \sin \varphi) \\ (\sin 2\theta - \cos 2\theta)(\cos \varphi + \sin \varphi) & (\sin 2\theta - \cos 2\theta)(\cos \varphi - \sin \varphi) \end{bmatrix} \quad (7.6)$$

To simplify the calculation, clockwise is taken to be positive this time. So, seen from behind, the fast axis of the half-wave plate is $+22.5^\circ$ (clockwise) from the X axis, and

similarly the linear polarizer is oriented at $+45^\circ$. The angle of rotation of the Faraday rotator also remains the same due to its non-reciprocal behavior. With these values set, when the matrix is applied to X-polarized light from the grating the following result is obtained, showing that the light was absorbed by the linear polarizer.

$$\mathbf{M}_{\lambda/2}\mathbf{M}_P\mathbf{M}_{RX} = \begin{bmatrix} 0 \\ 0 \end{bmatrix} \quad (7.7)$$

In reality, however, linear polarizers do not have infinite extinction ratios. The polarizer chosen in this design has an extinction ratio of greater than 23 dB [67], and any remaining light ends up polarized in the Z-direction. The effect of this remaining light on the laser must be considered. In general, the operation of a semiconductor laser with respect to feedback can be divided into five regimes [68]. For communications applications, operation in any of Regimes I–III is acceptable. These correspond to feedback of less than -40 dB. Depending on the contents of the silicon photonic circuit and the efficiency of the grating couplers, it may be necessary to include two polarizers in series. Furthermore, depending on the quality of the antireflective (AR) coating on the isolator components, it may also be necessary to mount the isolator rotated 8° so that any back reflections will be directed away from the laser cavity.

In terms of construction, the isolator can be included in a single stack of components with the prism. This stack can then be self-aligned by placing it directly against the ball lens with a final passive rotational alignment performed to orient it parallel to (or offset 8° from) the micro-optical bench substrate edges or the active region strip of the laser. The increased size of the stack makes it easier to handle during assembly. This is especially true when compared to the discrete prism, which does not have a flat top surface and has limited side surfaces, and where contact with the surfaces in the optical path should be avoided to prevent damage.

With the isolator included, the optimum working distance for the tested Fabry-Pérot lasers changes to $125 \mu\text{m}$. The simulated minimum insertion loss (excluding the loss of the grating coupler) also decreases from 3.19 dB to only 2.2 dB. This improvement in performance is a direct result of the decreased working distance, as the beam size at the ball lens is smaller and therefore experiences less of the effects of spherical aberrations.

For this simulation, in addition to adding the isolator, the prism angle was corrected to 41.675° to account for refractions at the lower surface. These refractions are similar to those that occur at the lower surface of the fiber before the epoxy is applied. This change, however, had only a minor effect, shifting the optimum working distance by $1 \mu\text{m}$ and improving the simulated insertion loss by

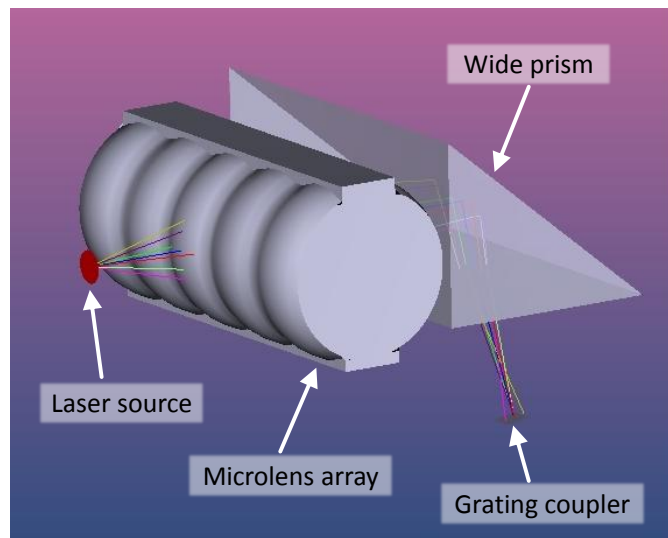


Figure 7.2: ZEMAX model of micro-optical bench with lens array

approximately 0.015 dB.

On the other hand, it does indicate a significant tolerance in the angle of the prism, but only in the case where the final micro-optical bench assembly is actively aligned. For passive alignment, such a variation in prism angle would cause the reflected beam to miss the grating entirely. However, the manufacturing tolerance for the prism angle is $\pm 0.25^\circ$, so the prism angle can be considered a controlled parameter where deliberate design changes can be accompanied by the adjustment of lateral alignment markers to account for the altered beam-aiming and still maintain compatibility with passive alignment.

7.3 Laser Arrays and Aspherical Lenses

Another useful enhancement to the micro-optical bench design is to extend it for use with arrays of lasers, whether in discrete dies or in a single laser bar. In particular, laser bars allow for a dense integration of multiple types and wavelengths of lasers. In order to facilitate this, the ball lens of the original micro-optical bench design is replaced with a microlens array. Such arrays are commercially available and are made in bulk quantities by the carefully-controlled etching of a glass wafer [69]. This wafer is then diced into smaller arrays of diverse size and quantity as required.

A micro-optical bench was modeled with such an array and a widened prism using Zemax (Fig. 7.2), with the full lens data given in Table 7.2. This model was based on standard microlens array production capabilities using a $600\ \mu\text{m}$ glass wafer, as well as the same $10^\circ/30^\circ$ laser beam divergence assumption from the original optical design. Several simulations were run to determine the effect of varying the pitch of

Table 7.2: Zemax Lens Data for Multiple Laser Integration with Lenslet Arrays

Surface	Type	Radius	Thickness	Glass	Aperture	Tilt/Decenter/Repeat	Description
0	Standard	Infinity	1 μm				For Ray Drawing Only
1	Standard	Infinity	185 μm		100 $\mu\text{m} \times 100 \mu\text{m}$ Rectangle		Stop Surface
2	Coordinate Break		0				Used for Alignment Tolerance
3	Lens Array	150 μm	100 μm	F_SILICA	635 $\mu\text{m} \times 300 \mu\text{m}$ Rectangle	Repeat: Number X=5, Width X=127 μm	Len Array Front
4	Standard	Infinity	400 μm	F_SILICA	Pickup From Surface 3		Len Array Body
5	Standard	Infinity	100 μm	F_SILICA	Pickup From Surface 3		End of Lens Array Body
6	Lens Array	-150 μm	0		Pickup From Surface 3	Repeat: Pickup From Surface 3	Len Array Rear
7	Coordinate Break		0				Used for Alignment Tolerance
8	Standard	Infinity	179 μm	N-BK7	635 $\mu\text{m} \times 300 \mu\text{m}$ Rectangle	40 μm Decenter Y Before Surface	Prism Start
9	Coordinate Break		0			-50° Tilt About X	Set up Angled Reflector
10	Standard	Infinity	0	MIRROR	635 $\mu\text{m} \times 466 \mu\text{m}$ Rectangle		Prism Reflector Surface
11	Coordinate Break		-150 μm			-40° Tilt About X	Finish up Angled Reflector
12	Standard	Infinity	0		635 $\mu\text{m} \times 358 \mu\text{m}$ Rectangle		End of Prism
13	Standard	Infinity	-255 μm		535 $\mu\text{m} \times 500 \mu\text{m}$ Rectangle	-223 μm Decenter Y Before Surface 223 μm Decenter Y After Surface	Substrate Aperture
14	Standard	Infinity	0		40 $\mu\text{m} \times 40 \mu\text{m}$ Rectangle	-137 μm Decenter Y Before Surface -10° Tilt About X Before Surface	Grating Coupler Surface

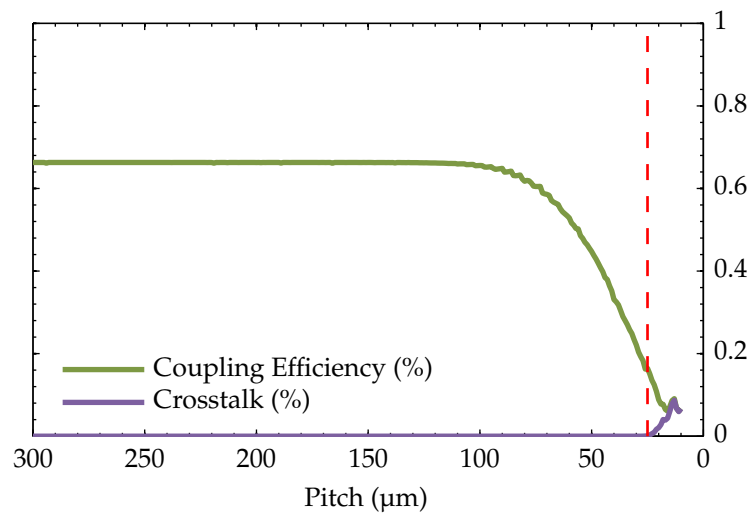


Figure 7.3: Simulated coupling efficiencies and crosstalk at various lens array pitches

lasers in a laser bar on the coupling efficiency of the micro-optical bench design and whether any crosstalk occurred between neighboring lasers. The Zemax macros to perform these simulations are shown in Listings A.4 and A.5 respectively.

The results of these simulations are summarized in Fig. 7.3. These results show that the pitch of the lasers can be reduced to approximately $100\ \mu\text{m}$ with no reduction in coupling efficiency. However, after this point, the coupling efficiency declines fairly steeply. On the other hand, no crosstalk occurs until the laser pitch descends below $25\ \mu\text{m}$, which itself approaches the practical lower limit for the spacing of the $12\ \mu\text{m}$ wide 1D gratings.

Another advantage of using microlens arrays is that the etching process which defines them allows for the specification of aspherical lenses. This, combined with the fact that the dicing of the arrays creates flat surfaces that provide a reference for the orientation of the lenses, allows for the integration of such lenses on the micro-optical bench substrate with minimal complexity. Instead of placing a ball lens in a self-aligning round laser-drilled hole, the lens array can be self-aligned in a rectangular trench (Fig. 7.4). In such a configuration, the contact of the lower curve of the lenses with the trench edge will self-align the array, establishing planarity in both roll and pitch as well as setting proper yaw alignment. Another option is to place the lens array directly on top of the micro-optical bench substrate surface as is done with the prism, with the flat lower surface aligning roll and pitch but with an additional passive or active alignment step required for yaw.

In addition, the lens array etching process and roll self-alignment allows the use of lens surfaces that are radially asymmetric. This facilitates compensation for the differing divergences of the laser output in the horizontal and vertical directions by specifying different curvatures in each axis. The combination of aspherical and

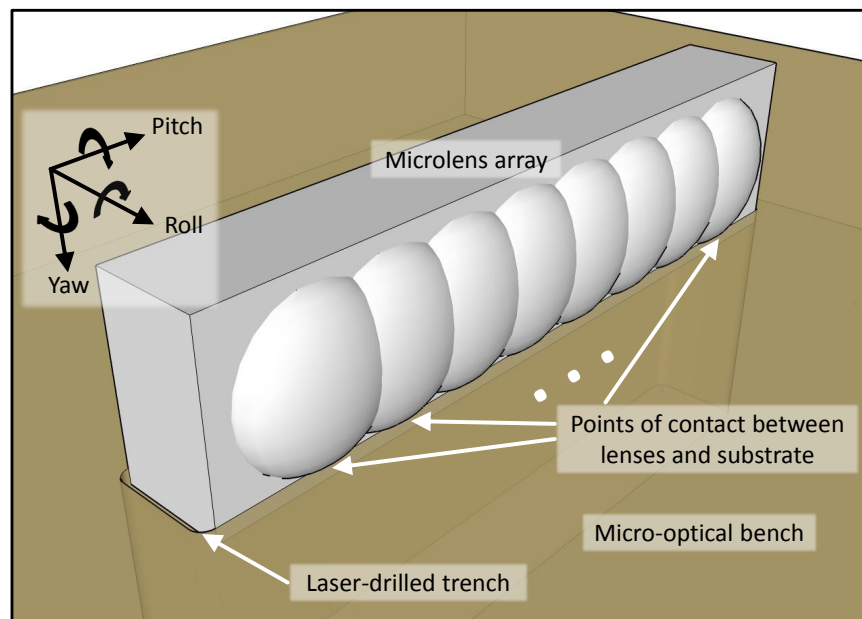


Figure 7.4: Schematic of lens array self-aligned in laser-drilled trench

asymmetric lens design capabilities allows for very specific tailoring of the lens to an individual laser, and promises to further improve the coupling efficiency of the micro-optical bench integration technology.

7.4 Final Thoughts

Several enhancements have been proposed to improve the stability, functionality and performance of the micro-optical bench technology. These enhancements illustrate the flexibility and extensibility of the technology and form the basis of a roadmap for future research on MOEMS-based hybrid integration. This research promises to enable the integration of not just lasers, but of any active devices that cannot be realized in current silicon- and germanium-based CMOS processing technologies.

In such a way, this technology facilitates in the present day the production of highly-integrated photonic systems comprising of components and materials that might not otherwise be deemed compatible. In designing such systems, there is no limitation in the selection of components to only what can be produced by a single process flow, cleanroom or production facility. This frees the designer to choose the best tools for each job with the confidence that they can be combined into a single, manufacturable unit.

Crucially, both the fiber packaging and the hybrid integration technologies are directed toward large-scale production. The chief goal and promise of silicon photonics is not only to drastically miniaturize photonic systems, but also to reduce

the cost and increase the production quantity of photonics to the level of that achieved by electronics by leveraging the existing CMOS processing technology used in the manufacture of such systems. However, the electrical integration done in current CMOS manufacturing does not pose the level of alignment challenges presented by photonic systems, especially when single-mode light propagation is desired.

Even so, for mass production of photonics to succeed, the constituent integration and packaging processes must be able to be performed at the wafer scale. To accomplish this, highly-accurate self-alignment must be used where possible, and where it is not feasible, passive alignment must be used. Active alignment results in increased complexity and production time that ultimately results in prohibitively higher costs and lower throughput. Ultimately, photonic devices must be produced in quantities of billions of units and at a cost that makes them available to people of all means. For medical applications, ideally the cost will be low enough to produce disposable devices.

Electrical integration and photonic integration do have one significant challenge in common: the management of heat. Whereas in electrical systems heat management is concerned more with power efficiency and preventing catastrophic failure, in photonic systems, especially with nano-scale features in silicon, heat poses a more fundamental challenge. Temperature changes in silicon systems have a significant impact on device performance, particularly in wavelength-sensitive devices such as micro-ring resonators and arrayed waveguide grating (AWG) multiplexers/demultiplexers.

It was mentioned earlier that one possibility is to use active cooling and to have a very deliberate understanding of the temperature distribution in a device. However, in the long run this too is prohibitively expensive, as well as counter to the ecological goal of reducing power consumption. To address this, work needs to continue to improve the efficiency of lasers so that less excess heat is generated for a given optical power requirement. Yet even with purely passive devices, significant effort needs to be devoted to designing low-cost athermal devices in silicon, so that the same device can be used in the Sahara as in Sweden.

The work presented in this thesis has already contributed to the research necessary to realize these goals by greatly simplifying the testing of these devices. Silicon chips fiber-packaged with this technology have been tested at many temperatures and in many environments without the need for constant alignment and realignment in a lab using bulky and obtrusive equipment. These devices left the lab, and even left the country, headed to research centers where standard fiber connectors were used to link the components under test to sources, measurement equipment and other components. Rather than landing sensitive probe pins under a

microscope to bias tiny pads on active devices, convenient pluggable modules were constructed (Fig. 7.5). Going still further, an electrically-tunable laser was integrated with submicrometer waveguides in a silicon photonics test bed. Given all these accomplishments, a truly significant step in bringing silicon photonics into the low-cost, mass-produced, plug-and-play world has been realized.

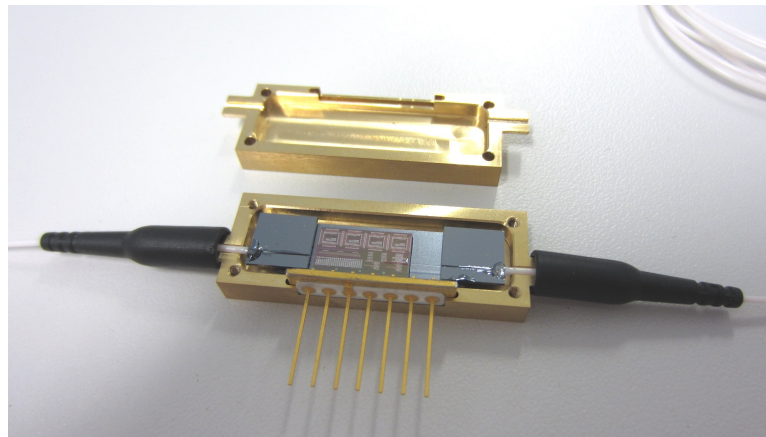


Figure 7.5: Silicon modulator in pluggable photonic package

Appendix A

Zemax Macro Source Listings

Listing A.1: Zemax Macro to Determine Working Distance

```
# Set file for output, goes to C:\Program Files\ZEMAX
filename$ = "sqmob3.txt"
FORMAT .6

max_power = 0
max_wd = 0

# Loop through all desired working distance values.
# The loop values do not act as expected and are
# adjusted accordingly.
# Also, adding 0.000001 avoids precision issues with
# Zemax at numbers such as e.g. 0.01.
FOR wd, 0.163001, 0.1811, 0.001

    # Set distance to lens.
    SETSURFACEPROPERTY 1, THIC, wd

    # Get coupling efficiency.
    c1 = OCOD("FICP")
    total_power = OPEV(c1, 0, 0, 0, 0, 0, 0)

    IF (total_power > max_power)
        max_power = total_power
        max_wd = wd
    ENDIF

    # Output to screen and file.
    PRINT wd, ", ", total_power
    OUTPUT filename$, APPEND
    PRINT wd, ", ", total_power
    OUTPUT SCREEN
NEXT
```

A. ZEMAX MACRO SOURCE LISTINGS

```
# Set optimal working distance value
SETSURFACEPROPERTY 1, THIC, max_wd
```

Listing A.2: Zemax Macro to Determine Lateral Alignment Tolerance

```
# Set file for output, goes to C:\Program Files\ZEMAX
filename$ = "sqmob3.txt"
FORMAT .6

# Loop through all desired x-offset values.
# The loop values do not act as expected and are
# adjusted accordingly.
# Also, adding 0.000001 avoids precision issues with
# Zemax at numbers such as e.g. 0.01.
FOR xoffset, 0.000001, 0.0151, 0.001

    # Set x-offset.
    SETSURFACEPROPERTY 2, PARM, xoffset, 1

    # Get coupling efficiency.
    c1 = OCOD("FICP")
    total_power = OPEV(c1, 0, 0, 0, 0, 0, 0)

    # Output to screen and file.
    PRINT xoffset, ", ", total_power
    OUTPUT filename$, APPEND
    PRINT xoffset, ", ", total_power
    OUTPUT SCREEN

NEXT

# Return value to original.
SETSURFACEPROPERTY 2, PARM, 0, 1
```

Listing A.3: Zemax Macro to Determine Ball Lens Alignment Tolerance

```
# Set file for output, goes to C:\Program Files\ZEMAX
filename$ = "sqmob3.txt"
FORMAT .6

# Loop through all desired ball lens offset values.
# The loop values do not act as expected and are
# adjusted accordingly.
# Also, adding 0.000001 avoids precision issues with
# Zemax at numbers such as e.g. 0.01.
FOR yoffset, -0.016001, 0.0121, 0.001

    # Set y-offset of ball lens.
    SETSURFACEPROPERTY 2, PARM, yoffset, 2
    SETSURFACEPROPERTY 5, PARM, -yoffset, 2
```

A. ZEMAX MACRO SOURCE LISTINGS

```
# Get coupling efficiency.
c1 = OCOD("FICP")
total_power = OPEV(c1, 0, 0, 0, 0, 0, 0)

# Output to screen and file.
PRINT yoffset, ", ", total_power
OUTPUT filename$, APPEND
PRINT yoffset, ", ", total_power
OUTPUT SCREEN

NEXT

# Return values to originals.
SETSURFACEPROPERTY 2, PARM, 0, 2
SETSURFACEPROPERTY 5, PARM, 0, 2
```

Listing A.4: Zemax Macro to Simulate Coupling Efficiency of Lens Arrays of Varying Pitch

```
# Set file for output, goes to C:\Program Files\ZEMAX
filename$ = "sqmobarray.txt"
FORMAT .6

# Loop through all desired pitch values
# The loop values do not act as expected and are
# adjusted accordingly.
# Also, adding 0.000001 avoids precision issues with
# Zemax at numbers such as e.g. 0.01.
FOR pitch, 0.300001, 0.009999, -0.001

# Set pitch of lenslet array
SETSURFACEPROPERTY 3, 10, pitch, 3
SETSURFACEPROPERTY 6, 10, pitch, 3

# Set X aperture to match
SETSURFACEPROPERTY 3, 21, pitch*2.5
SETSURFACEPROPERTY 6, 21, pitch*2.5

# Get coupling efficiency
c1 = OCOD("FICP")
total_power = OPEV(c1, 0, 0, 0, 0, 0, 0)

# Output to screen and file
PRINT pitch, ", ", total_power
OUTPUT filename$, APPEND
PRINT pitch, ", ", total_power
OUTPUT SCREEN

NEXT

# Return values to originals
```

A. ZEMAX MACRO SOURCE LISTINGS

```
SETSURFACEPROPERTY 3, 10, 0.127, 3
SETSURFACEPROPERTY 6, 10, 0.127, 3
SETSURFACEPROPERTY 3, 21, 0.127*2.5
SETSURFACEPROPERTY 6, 21, 0.127*2.5
```

Listing A.5: Zemax Macro to Simulate Crosstalk of Lens Arrays of Varying Pitch

```
# Set file for output, goes to C:\Program Files\ZEMAX
filename$ = "sqmobxtalk.txt"
FORMAT .6

# Loop through all desired pitch values measuring crosstalk
# The loop values do not act as expected and are
# adjusted accordingly.
# Also, adding 0.00001 avoids precision issues with
# Zemax at numbers such as e.g. 0.01.
FOR pitch, 0.30001, 0.009999, -0.001

    # Set pitch of lenslet array
    SETSURFACEPROPERTY 3, 10, pitch, 3
    SETSURFACEPROPERTY 6, 10, pitch, 3

    # Set X aperture to match
    SETSURFACEPROPERTY 3, 21, pitch*2.5
    SETSURFACEPROPERTY 6, 21, pitch*2.5

    # Shift detector X position to adjacent channel
    SETSURFACEPROPERTY 12, 61, pitch

    # Get coupling efficiency
    c1 = OCOD("FICP")
    total_power = OPEV(c1, 0, 0, 0, 0, 0, 0)

    # Output to screen and file
    PRINT pitch, ", ", total_power
    OUTPUT filename$, APPEND
    PRINT pitch, ", ", total_power
    OUTPUT SCREEN

NEXT

# Return values to originals
SETSURFACEPROPERTY 3, 10, 0.127, 3
SETSURFACEPROPERTY 6, 10, 0.127, 3
SETSURFACEPROPERTY 3, 21, 0.127*2.5
SETSURFACEPROPERTY 6, 21, 0.127*2.5
SETSURFACEPROPERTY 12, 61, 0
```

Bibliography

- [1] J. Hecht, *City of Light: The Story of Fiber Optics*. Oxford University Press, 2004.
- [2] Corning Incorporated, "Corning SMF-28 Optical Fiber Product Information," 2002.
- [3] Ioffe Physico-Technical Institute, "New Semiconductor Materials. Characteristics and Properties," 2001. [Online]. Available: <http://www.ioffe.ru/SVA/NSM/>
- [4] E. Hecht and A. Zajac, *Optics*, 4th ed. Pearson, 2003.
- [5] A. Wang, P. G. Finlayson, J. Li, K. Brabant, C. A. Black, J. McAllister II, T. Cao, H. Tang, X. Liang, S. O. Salley, G. W. Auner, and K. Y. S. Ng, "Is Silicon Suitable for Making Implantable Biomedical Devices," in *American Institute of Chemical Engineering Annual Meeting*, Cincinnati, OH, 2005, p. 578a. [Online]. Available: <https://aiche.confex.com/aiche/2005/techprogram/P15420.HTM>
- [6] I. E. Trofimov, "Photonic integration: fashionable or practical?" 2001. [Online]. Available: <http://www.lightwaveonline.com/articles/print/volume-18/issue-4/features/photonic-integration-fashionable-or-practical-53468202.html>
- [7] R. E. Camacho-Aguilera, Y. Cai, N. Patel, J. T. Bessette, M. Romagnoli, L. C. Kimerling, and J. Michel, "An electrically pumped germanium laser," *Optics Express*, vol. 20, no. 10, pp. 11 316–20, May 2012. [Online]. Available: <http://www.opticsexpress.org/abstract.cfm?URI=oe-20-10-11316>
- [8] H. Rong, R. Jones, A. Liu, O. Cohen, D. Hak, A. Fang, and M. Paniccia, "A continuous-wave Raman silicon laser," *Nature*, vol. 433, no. 7027, pp. 725–8, Feb. 2005. [Online]. Available: <http://dx.doi.org/10.1038/nature03346>
- [9] J. H. Song, J. Zhang, H. Zhang, C. Li, and G. Q. Lo, "Si-photonics based passive device packaging and module performance," *Optics Express*, vol. 19, no. 19, p. 18020, Aug. 2011. [Online]. Available: <http://www.opticsexpress.org/abstract.cfm?URI=oe-19-19-18020>
- [10] C. Stamatidis, F. Gomez-Agis, L. Stampoulidis, K. Vyrsoinos, I. Lazarou, H. J. S. Dorren, L. Zimmermann, K. Voigt, D. Van Thourhout, P. De Heyn, and

- H. Avramopoulos, "The BOOM project: Towards 160 Gb/s Packet Switching Using SOI Photonic Integrated Circuits and Hybrid Integrated Optical Flip-flops," *Journal of Lightwave Technology*, vol. 30, no. 1, pp. 22–30, 2011. [Online]. Available: <http://ieeexplore.ieee.org/lpdocs/epic03/wrapper.htm?arnumber=6078384>
- [11] G. Roelkens, P. Dumon, W. Bogaerts, D. Van Thourhout, and R. Baets, "Efficient silicon-on-insulator fiber coupler fabricated using 248-nm-deep UV lithography," *IEEE Photonics Technology Letters*, vol. 17, no. 12, pp. 2613–2615, Dec. 2005. [Online]. Available: <http://ieeexplore.ieee.org/lpdocs/epic03/wrapper.htm?arnumber=1542166>
- [12] H. Sun, A. Chen, A. Szep, and L. R. Dalton, "Efficient fiber coupler for vertical silicon slot waveguides," *Optics Express*, vol. 17, no. 25, p. 22571, Nov. 2009. [Online]. Available: <http://www.opticsexpress.org/abstract.cfm?URI=oe-17-25-22571>
- [13] F. E. Doany, B. G. Lee, S. Assefa, W. M. J. Green, M. Yang, C. L. Schow, C. V. Jahnes, S. Zhang, J. Singer, V. I. Kopp, J. A. Kash, and Y. A. Vlasov, "Multichannel High-Bandwidth Coupling of Ultradense Silicon Photonic Waveguide Array to Standard-Pitch Fiber Array," *Journal of Lightwave Technology*, vol. 29, no. 4, pp. 475–482, 2011. [Online]. Available: <http://www.opticsinfobase.org/abstract.cfm?URI=jlt-29-4-475>
- [14] C. R. Pollock, *Fundamentals of Optoelectronics*. Irwin, 1995.
- [15] Department of Information Technology (INTEC) Ghent University, "CAMFR (CAvity Modelling FRamework)." [Online]. Available: <http://camfr.sourceforge.net/>
- [16] D. Taillaert, "Grating couplers as Interface between Optical Fibres and Nanophotonic Waveguides," Ph.D. dissertation, Universiteit Gent, 2004.
- [17] D. Taillaert, F. Van Laere, M. Ayre, W. Bogaerts, D. Van Thourhout, P. Bienstman, and R. Baets, "Grating Couplers for Coupling between Optical Fibers and Nanophotonic Waveguides," *Japanese Journal of Applied Physics*, vol. 45, no. No. 8A, pp. 6071–6077, Aug. 2006. [Online]. Available: <http://jjap.ipap.jp/link?JJAP/45/6071/>
- [18] F. Van Laere, G. Roelkens, M. Ayre, J. Schrauwen, D. Taillaert, D. Van Thourhout, T. F. Krauss, and R. Baets, "Compact and Highly Efficient Grating Couplers Between Optical Fiber and Nanophotonic Waveguides," *Journal of Lightwave Technology*, vol. 25, no. 1, pp. 151–156, Jan. 2007. [Online]. Available: <http://jlt.osa.org/abstract.cfm?URI=jlt-25-1-151>
- [19] C. Kopp, E. Augendre, R. Orobtcouk, O. Lemonnier, and J.-M. Fedeli,

- “Enhanced Fiber Grating Coupler Integrated by Wafer-to-Wafer Bonding,” *Journal of Lightwave Technology*, vol. 29, no. 12, pp. 1847–1851, Jun. 2011. [Online]. Available: http://ieeexplore.ieee.org/xpl/freeabs_all.jsp?arnumber=5755125
- [20] X. Chen, C. Li, C. K. Y. Fung, S. M. G. Lo, and H. K. Tsang, “Apodized Waveguide Grating Couplers for Efficient Coupling to Optical Fibers,” *IEEE Photonics Technology Letters*, vol. 22, no. 15, pp. 1156–1158, Aug. 2010. [Online]. Available: <http://ieeexplore.ieee.org/xpl/articleDetails.jsp?arnumber=5482077>
- [21] A. Scherer, “Silicon Photonics - Last 15 Years,” 2012. [Online]. Available: http://www.e3s-center.org/pubs/103/PEB2012_4_AScherer_Webfinal.pdf
- [22] K. Qin, D. Gao, C. Bao, Z. Zhao, X. Zhou, T. Lu, and L. Chen, “High Efficiency and Broadband Two-Dimensional Blazed Grating Coupler With Fully Etched Triangular Holes,” *Journal of Lightwave Technology*, vol. 30, no. 14, pp. 2363–2366, Jul. 2012. [Online]. Available: <http://ieeexplore.ieee.org/xpl/articleDetails.jsp?arnumber=6197207>
- [23] F. Van Laere, T. Claes, J. Schrauwen, S. Scheerlinck, W. Bogaerts, D. Taillaert, L. O’Faolain, D. Van Thourhout, and R. Baets, “Compact Focusing Grating Couplers for Silicon-on-Insulator Integrated Circuits,” *IEEE Photonics Technology Letters*, vol. 19, no. 23, pp. 1919–1921, Dec. 2007. [Online]. Available: http://ieeexplore.ieee.org/xpl/freeabs_all.jsp?arnumber=4383198
- [24] L. Zimmermann, G. B. Preve, T. Tekin, T. Rosin, and K. Landles, “Packaging and Assembly for Integrated Photonics—A Review of the ePIXpack Photonics Packaging Platform,” *IEEE Journal of Selected Topics in Quantum Electronics*, vol. 17, no. 3, pp. 645–651, May 2011. [Online]. Available: <http://ieeexplore.ieee.org/lpdocs/epic03/wrapper.htm?arnumber=5658100>
- [25] T. Tekin, “Review of Packaging of Optoelectronic, Photonic, and MEMS Components,” *IEEE Journal of Selected Topics in Quantum Electronics*, vol. 17, no. 3, pp. 704–719, May 2011. [Online]. Available: <http://ieeexplore.ieee.org/lpdocs/epic03/wrapper.htm?arnumber=5740939>
- [26] H. Chen, T. Koonen, B. Snyder, P. O’Brien, X. Chen, G. T. Reed, H. van den Boom, and O. Raz, “Packaged Mode Multiplexer based on Silicon Photonics,” in *Asia Communications and Photonics Conference*. Optical Society of America, Nov. 2012, p. AT2B.4. [Online]. Available: <http://www.opticsinfobase.org/abstract.cfm?URI=ACP-2012-AT2B.4>
- [27] S. Bernabé, C. Kopp, L. Lombard, and J.-M. Fedeli, “Microelectronic-like packaging for silicon photonics : A 10 Gbps multi-chip-module optical receiver based on Ge-on-Si photodiode,” in *3rd Electronics System Integration Technology*

- Conference ESTC*. IEEE, Sep. 2010, pp. 1–5. [Online]. Available: <http://ieeexplore.ieee.org/xpl/articleDetails.jsp?arnumber=5642980>
- [28] Chiral Photonics Inc., “The Pitch Reducing Optical Fiber Array (PROFA).” [Online]. Available: <http://www.chiralphotonics.com/Web/profa.html>
- [29] J. Van Campenhout, P. Rojo-Romeo, P. Regreny, C. Seassal, D. Van Thourhout, S. Verstuyft, L. Di Cioccio, J.-M. Fedeli, C. Lagahe, and R. Baets, “Electrically pumped InP-based microdisk lasers integrated with a nanophotonic silicon-on-insulator waveguide circuit.” *Optics Express*, vol. 15, no. 11, pp. 6744–9, May 2007. [Online]. Available: <http://www.ncbi.nlm.nih.gov/pubmed/19546984>
- [30] D. Van Thourhout, T. Spuesens, S. K. Selvaraja, L. Liu, G. Roelkens, R. Kumar, G. Morthier, P. Rojo-Romeo, F. Mandorlo, P. Regreny, O. Raz, C. Kopp, and L. Grenouillet, “Nanophotonic Devices for Optical Interconnect,” *IEEE Journal of Selected Topics in Quantum Electronics*, vol. 16, no. 5, pp. 1363 – 1375, 2010. [Online]. Available: <http://ieeexplore.ieee.org/lpdocs/epic03/wrapper.htm?arnumber=5424011>
- [31] Y. Halioua, A. Bazin, P. Monnier, T. J. Karle, I. Sagnes, G. Roelkens, D. Van Thourhout, F. Raineri, and R. Raj, “III-V photonic crystal wire cavity laser on silicon wafer,” *Journal of the Optical Society of America B*, vol. 27, no. 10, p. 2146, Sep. 2010. [Online]. Available: <http://josab.osa.org/abstract.cfm?URI=josab-27-10-2146>
- [32] B. Ben Bakir, A. Descos, N. Olivier, D. Bordel, P. Grosse, E. Augendre, L. Fulbert, and J. M. Fedeli, “Electrically driven hybrid Si/III-V Fabry-Pérot lasers based on adiabatic mode transformers,” *Optics Express*, vol. 19, no. 11, p. 10317, May 2011. [Online]. Available: <http://www.opticsexpress.org/abstract.cfm?URI=oe-19-11-10317>
- [33] S. R. Jain, Y. Tang, H.-W. Chen, M. N. Sysak, and J. E. Bowers, “Integrated Hybrid Silicon Transmitter,” *Journal of Lightwave Technology*, vol. 30, no. 1, pp. 1–8, Jan. 2012. [Online]. Available: http://ieeexplore.ieee.org/xpl/freeabs_all.jsp?arnumber=6062628
- [34] J. Justice, C. Bower, M. Meitl, M. B. Mooney, M. A. Gubbins, and B. Corbett, “Wafer-scale integration of group III–V lasers on silicon using transfer printing of epitaxial layers,” *Nature Photonics*, vol. 6, no. 9, pp. 612–616, Aug. 2012. [Online]. Available: <http://dx.doi.org/10.1038/nphoton.2012.204>
- [35] M. Kapulainen, S. Ylinen, T. Aalto, M. Harjanne, K. Solehmainen, J. Ollila, and V. Vilokkinen, “Hybrid integration of InP lasers with SOI waveguides using thermocompression bonding,” in *2008 5th IEEE International Conference on*

- Group IV Photonics*. IEEE, 2008, pp. 61–63. [Online]. Available: http://ieeexplore.ieee.org/xpl/freeabs_all.jsp?arnumber=4638097
- [36] J. Tidmarsh, S. Fasham, P. Stopford, A. Tomlinson, and T. Bestwick, “A narrow linewidth laser for WDM applications using silicon waveguide technology,” in *IEEE Lasers and Electro-Optics Society 12th Annual Meeting (LEOS '99)*, San Francisco, CA, 1999, pp. 497 – 498 Vol. 2. [Online]. Available: http://ieeexplore.ieee.org/xpls/abs_all.jsp?arnumber=811816&tag=1
- [37] A. J. Zilkie, P. Seddighian, B. J. Bijlani, W. Qian, D. C. Lee, S. Fatholouloumi, J. Fong, R. Shafiiha, D. Feng, B. J. Luff, X. Zheng, J. E. Cunningham, A. V. Krishnamoorthy, and M. Asghari, “Power-efficient III-V/silicon external cavity DBR lasers.” *Optics Express*, vol. 20, no. 21, pp. 23 456–62, Oct. 2012. [Online]. Available: <http://www.opticsexpress.org/abstract.cfm?URI=oe-20-21-23456>
- [38] S. Tanaka, S.-H. Jeong, S. Sekiguchi, T. Kurahashi, Y. Tanaka, and K. Morito, “High-output-power, single-wavelength silicon hybrid laser using precise flip-chip bonding technology,” *Optics Express*, vol. 20, no. 27, pp. 28 057–69, Dec. 2012. [Online]. Available: <http://www.opticsexpress.org/abstract.cfm?URI=oe-20-27-28057>
- [39] A. Narasimha, B. Analui, E. Balmater, A. Clark, T. Gal, D. Guckenberger, S. Gutierrez, M. Harrison, R. Ingram, R. Koumans, D. Kucharski, K. Leap, Y. Liang, A. Mekis, S. Mirsaidi, M. Peterson, T. Pham, T. Pinguet, D. Rines, V. Sadagopan, T. J. Sleboda, D. Song, Y. Wang, B. Welch, J. Witzens, S. Abdalla, S. Gloeckner, and P. De Dobbelaere, “A 40-Gb/s QSFP Optoelectronic Transceiver in a 0.13 μm CMOS Silicon-on-Insulator Technology,” in *OFC/NFOEC 2008*. IEEE, Feb. 2008, pp. 1–3. [Online]. Available: http://ieeexplore.ieee.org/xpl/freeabs_all.jsp?arnumber=4528356
- [40] T. Pinguet, “Silicon Photonics for 25 Gb/s and beyond,” in *SPIE Photonics North*, 2013.
- [41] L. Zimmermann, H. Schröder, P. Dumon, W. Bogaerts, and T. Tekin, “ePIXpack - Advanced Smart Packaging Solutions for Silicon Photonics,” in *14th European Conference on Integrated Optics*, Eindhoven, The Netherlands, 2008, pp. 33–36.
- [42] T. Pinguet, B. Analui, E. Balmater, D. Guckenberger, M. Harrison, R. Koumans, D. Kucharski, Y. Liang, G. Masini, A. Mekis, S. Mirsaidi, A. Narasimha, M. Peterson, D. Rines, V. Sadagopan, S. Sahni, T. Sleboda, D. Song, Y. Wang, B. Welch, J. Witzens, J. Yao, S. Abdalla, S. Gloeckner, P. De Dobbelaere, and G. Capellini, “Monolithically integrated high-speed CMOS photonic transceivers,” in *2008 5th IEEE International Conference on Group IV Photonics*. Cardiff, Wales: IEEE, 2008, pp. 362–364. [Online]. Available: <http://ieeexplore.ieee.org/xpl/articleDetails.jsp?arnumber=4638200>

- [43] B. E. A. Saleh and M. C. Teich, *Fundamentals of Photonics*. Wiley-Interscience, 1991.
- [44] Norland Products Inc., “Norland Optical Adhesive 61.” [Online]. Available: http://www.norlandprod.com/adhesives/noa_61.html
- [45] P. Dumon and D. Taillaert, “Silicon Photonics Platform Building a vertical fibre coupling setup,” 2006.
- [46] P. Dumon, “IMEC Standard Passives.” [Online]. Available: <http://www.epixfab.eu/technologies/imec-siphotonics>
- [47] S. Pathak, M. Vanslembrouck, P. Dumon, D. Van Thourhout, and W. Bogaerts, “Compact SOI-based polarization diversity wavelength de-multiplexer circuit using two symmetric AWGs,” *Optics Express*, vol. 20, no. 26, p. B493, Dec. 2012. [Online]. Available: <http://www.opticsexpress.org/abstract.cfm?URI=oe-20-26-B493>
- [48] Y.-D. Liu, Y.-C. Tsai, Y.-K. Lu, L.-J. Wang, M.-C. Hsieh, S.-M. Yeh, and W.-H. Cheng, “New Scheme of Double-Variable-Curvature Microlens for Efficient Coupling High-Power Lasers to Single-Mode Fibers,” *Journal of Lightwave Technology*, vol. 29, no. 6, pp. 898–904, Mar. 2011. [Online]. Available: http://ieeexplore.ieee.org/xpl/freeabs_all.jsp?arnumber=5678609
- [49] C. C. Davis, *Lasers and Electro-Optics: Fundamentals and Engineering*. Cambridge University Press, 2002.
- [50] R. Beesley, private communication, June 2011.
- [51] COMSOL AB, *Heat Transfer Module User’s Guide Version 3.5a*, 2008.
- [52] A. Collins, E. Lightowers, and P. Dean, “Lattice Vibration Spectra of Aluminum Nitride,” *Physical Review*, vol. 158, no. 3, pp. 833–838, Jun. 1967. [Online]. Available: <http://link.aps.org/doi/10.1103/PhysRev.158.833>
- [53] H. Farzanehfard and A. Elshabini-Riad, “Wideband characterization of aluminum nitride (AlN) substrates and high frequency application on these substrates,” in *Conference on Precision Electromagnetic Measurements*. IEEE, 1990, pp. 218–219. [Online]. Available: <http://ieeexplore.ieee.org/xpl/articleDetails.jsp?arnumber=109996>
- [54] Y. Goldberg, “Aluminum Nitride (AlN),” in *Properties of Advanced Semiconductor Materials: GaN, AlN, InN, BN, SiC, SiGe*, M. Levinshtein, S. Rumyantsev, and M. Shur, Eds. New York: John Wiley & Sons, Inc., 2001, pp. 31–47.
- [55] T. Shimizu, Y. Kawahara, S. Akasaka, and Y. Kogami, “Complex permittivity measurement of aluminum nitride by the cut-off circular waveguide method from 40GHz to 100GHz,” in *Proceedings of the Asia-Pacific Microwave Conference*

- (APMC), 2011, pp. 1450–1453. [Online]. Available:
http://ieeexplore.ieee.org/xpls/abs_all.jsp?arnumber=6174035
- [56] H. Wheeler, “Transmission-Line Properties of a Strip on a Dielectric Sheet on a Plane,” *IEEE Transactions on Microwave Theory and Techniques*, vol. 25, no. 8, pp. 631–647, Aug. 1977. [Online]. Available:
<http://ieeexplore.ieee.org/xpl/articleDetails.jsp?arnumber=1129179>
- [57] C. Wen, “Coplanar Waveguide: A Surface Strip Transmission Line Suitable for Nonreciprocal Gyromagnetic Device Applications,” *IEEE Transactions on Microwave Theory and Techniques*, vol. 17, no. 12, pp. 1087–1090, Dec. 1969. [Online]. Available:
http://ieeexplore.ieee.org/xpls/abs_all.jsp?arnumber=1127105
- [58] Newport Corporation, *2832-C Dual-Channel Power Meter Instruction Manual*, 1995.
- [59] S. O’Brien, F. Smyth, J. O’Carroll, P. M. Anandarajah, D. Bitauld, S. Osborne, R. Phelan, B. Kelly, J. O’Gorman, F. H. Peters, B. Roycroft, B. Corbett, and L. P. Barry, “Design, Characterization, and Applications of Index-Patterned Fabry–Pérot Lasers,” *IEEE Journal of Selected Topics in Quantum Electronics*, vol. 17, no. 6, pp. 1621–1631, Nov. 2011. [Online]. Available:
<http://ieeexplore.ieee.org/lpdocs/epic03/wrapper.htm?arnumber=5755170>
- [60] J.-O. Westrom, S. Hammerfeldt, J. Buus, R. Siljan, R. Laroy, and H. de Vries, “Design of a widely tunable modulated grating Y-branch laser using the additive Vernier effect for improved super-mode selection,” in *IEEE 18th International Semiconductor Laser Conference*. IEEE, 2002, pp. 99–100. [Online]. Available:
<http://ieeexplore.ieee.org/lpdocs/epic03/wrapper.htm?arnumber=1041137>
- [61] N. M. Ravindra, S. Abedrabbo, W. Chen, F. M. Tong, A. K. Nanda, and A. C. Speranza, “Temperature-dependent emissivity of silicon-related materials and structures,” *IEEE Transactions on Semiconductor Manufacturing*, vol. 11, no. 1, pp. 30–39, 1998. [Online]. Available:
http://ieeexplore.ieee.org/xpls/abs_all.jsp?arnumber=661282
- [62] Community Research and Development Information Service (CORDIS), “Epixfab services specifically targeting (SME) industrial take-up of advanced silicon photonics.” [Online]. Available:
http://cordis.europa.eu/projects/rcn/99795_en.html
- [63] —, “Photonic Libraries And Technology for Manufacturing.” [Online]. Available: http://cordis.europa.eu/projects/rcn/104781_en.html
- [64] —, “FDMA Access By Using Low-cost Optical Network Units in Silicon

- Photonics." [Online]. Available:
http://cordis.europa.eu/projects/rcn/104608_en.html
- [65] PhoeniX B.V., "PhoeniX Software - Design Flow Automation." [Online]. Available: <http://www.phoenixbv.com/product.php?prodid=50010201&submenu=dfa&prdgrpID=2&prodname=MaskEngineer>
- [66] Integrated Photonics Inc., "MGL Garnet - Latching Faraday Rotator." [Online]. Available: http://www.integratedphotonics.com/images/Product_Bulletin_MGL_F2-7.pdf
- [67] Corning Incorporated, "Polarcor UltraThin Glass Polarizers Product Information," pp. 1–4, 2005. [Online]. Available: <http://www.corning.com/WorkArea/showcontent.aspx?id=14921>
- [68] R. Tkach and A. Chraplyvy, "Regimes of feedback effects in 1.5- μm distributed feedback lasers," *Journal of Lightwave Technology*, vol. 4, no. 11, pp. 1655–1661, 1986. [Online]. Available: <http://ieeexplore.ieee.org/lpdocs/epic03/wrapper.htm?arnumber=1074666>
- [69] SÜSS MicroTec AG, "SÜSS MicroOptics - Refractive Microlens Arrays." [Online]. Available: <http://www.suss-microoptics.com/products-solutions/microlens.html>

List of Figures

1.1	Cross-section of a sample silicon photonic waveguide	3
1.2	Doped-silica AWG and much smaller silicon AWG	4
1.3	Relative sizes of fiber and silicon photonic components	5
1.4	Angled scanning electron micrograph of silicon ring resonator filter	6
2.1	Schematic of inverse taper coupler	10
2.2	Wavevectors of light refracted and diffracted	11
2.3	Schematic of wavevectors at grating coupler	12
2.4	Components of the wavevector of a guided mode	13
2.5	Angled scanning electron micrograph of grating coupler	14
2.6	Steps to reduce spot size using a grating coupler	14
2.7	Measured insertion loss of grating-coupled waveguide	15
2.8	Schematic of pitch-reducing fiber array (PROFA)	16
3.1	Schematic of light path in angle-polished fiber	20
3.2	Simulated alignment tolerances of single-fiber package	26
3.3	Newport AutoAlign workstation used for fiber and laser packaging	27
3.4	Measured alignment tolerances of single-fiber package	28
3.5	Fiber after controlled distribution of epoxy showing clean end facet	30
3.6	Completed package with top removed	30
3.7	Optical spectrum changes with fiber pitch and introduction of epoxy	31
3.8	Schematic of changes due to the introduction of epoxy at the fiber base	32
3.9	Net effect of epoxy with angle-polished fiber	33
3.10	Schematic of single-fiber design rule dimensions	34
3.11	Optical transmission spectrum of packaged ring resonator filter	35
4.1	Diagram of V-groove showing precise three-point alignment	37
4.2	Standard 127 μm pitch fiber array showing interleaved ribbons	38
4.3	Standard fiber array with 400 μm lower lid and 40° polish	39
4.4	Schematic of “lidless” fiber array showing improved working distance	39
4.5	Image of “lidless” fiber array highlighting yield and performance issues	40
4.6	Schematic of double-polish fiber array	41
4.7	Lateral alignment tolerance of fiber array	42
4.8	X and Y cross-sections of fiber array lateral tolerance	42
4.9	Schematic of effect of roll rotation on fiber array alignment	43
4.10	Schematic of effect of yaw rotation on fiber array alignment	44
4.11	Measured rotational alignment tolerances of fiber array	45
4.12	12 channel array packaged with silicon photonic integrated circuit	45
4.13	Fiber-to-fiber insertion loss of fiber array edge channels	46
4.14	Schematic of 250 μm fiber array design rule dimensions	48

4.15	Schematic of 127 μm fiber array design rule dimensions	49
4.16	Schematics of alignment shunts for fiber array packaging	50
4.17	Outline of two-step alignment process	51
4.18	Fully-packaged AWG with single fiber input, fiber array output	52
5.1	Schematic of actively-aligned micromirror	55
5.2	Scanning electron microscope image of diced fiber	56
5.3	Schematic of MOEMS-based micro-optical bench	58
5.4	Schematic of micro-optical bench constructed with discrete components	59
5.5	Zemax 3D layout of micro-optical bench	60
5.6	Zemax physical optics propagation output	62
5.7	Close-up of plan rays showing effects of spherical aberrations	62
5.8	Simulation results for laser to ball lens working distance tolerance . .	63
5.9	Simulation results for laser lateral alignment tolerance	64
5.10	Simulation results for ball lens height variation	65
5.11	Mechanical design of micro-optical bench substrate	66
5.12	COMSOL mesh of micro-optical bench and components	67
5.13	Simulation results of micro-optical bench in air showing overheating .	68
5.14	Heating of micro-optical bench in 10 ms intervals	69
5.15	Simulation results of micro-optical bench on chip with passive cooling	69
5.16	Simulation results of micro-optical bench on chip with TEC set at 20°C	70
6.1	Die bonding and wire bonding micro-optical bench components	75
6.2	Thermocompression bonding of flex connector to micro-optical bench	76
6.3	Equipment and heating schedule used for thermocompression bonding	77
6.4	Micro-optical bench assembly with tunable laser showing relative size	78
6.5	Diagram of micro-optical bench self-aligning flat on chip surface . . .	79
6.6	Micro-optical bench mounted in clamp during alignment	79
6.7	Overhead image from high-magnification IR camera during alignment	80
6.8	Integrated lasers with active temperature control and monitoring . . .	81
6.9	Lateral alignment tolerances of micro-optical bench placement	82
6.10	Peak values and sample spectra of packaged tunable laser	83
6.11	Steady-state thermal measurements at various drive currents	86
6.12	Dynamic thermal response of micro-optical bench and silicon chip . .	87
7.1	ZEMAX model of micro-optical bench with integrated isolator	92
7.2	ZEMAX model of micro-optical bench with lens array	95
7.3	Simulated coupling efficiencies and crosstalk at various lens pitches .	97
7.4	Schematic of lens array self-aligned in laser-drilled trench	98
7.5	Silicon modulator in pluggable photonic package	100

List of Tables

3.1	Zemax Lens Data for Fiber Coupling	25
3.2	Design Rules for Single-Fiber Packaging	34
4.1	Design Rules for Fiber Array Packaging at 250 μm Pitch	48
4.2	Design Rules for Fiber Array Packaging at 127 μm Pitch	49
5.1	Zemax Lens Data for Laser Integration	61
6.1	Schedule of Temperatures for micro-optical bench Construction	74
7.1	Comparison of Hybrid Integration Technologies for SOI	91
7.2	Zemax Lens Data for Multiple Laser Integration with Lenslet Arrays	96

Publications

Journal Articles

- [1] B. Snyder and P. O'Brien, "Packaging Process for Grating-Coupled Silicon Photonic Waveguides Using Angle-Polished Fibers," *IEEE Transactions on Components, Packaging and Manufacturing Technology*, vol. 3, no. 6, pp. 954–959, 2013. [Online]. Available: <http://ieeexplore.ieee.org/xpl/articleDetails.jsp?arnumber=6416952>
- [2] F. Gity, A. Daly, B. Snyder, F. H. Peters, J. Hayes, A. P. Morrison, C. Colinge, and B. Corbett, "Amplified responsivity from Ge/Si heterojunction photodiodes fabricated by low temperature wafer bonding," *Optics Express*, 2013.
- [3] B. Snyder, B. Corbett, and P. O'Brien, "Hybrid Integration of Wavelength-Tunable Laser with Silicon Photonic Integrated Circuit," *Journal of Lightwave Technology*, 2013. **(Submitted)**
- [4] H. Chen, V. Sleiffer, B. Snyder, M. Kuschnerov, R. van Uden, Y. Jung, C. Okonkwo, O. Raz, P. O'Brien, H. de Waardt and T. Koonen, "Demonstration of a Photonic Integrated Mode Coupler with MDM and WDM Transmission," *Photonics Technology Letters*, 2013. **(Submitted)**

Conferences

- [5] B. Snyder and P. O'Brien, "Planar Fiber Packaging Method for Silicon Photonic Integrated Circuits," in *Optical Fiber Communication Conference*. Optical Society of America, Mar. 2012, p. OM2E.5. [Online]. Available: <http://www.opticsinfobase.org/abstract.cfm?URI=OFC-2012-OM2E.5>
- [6] B. Snyder and P. O'Brien, "Challenges for Silicon Photonics and III-V Packaging and Assembly: The ePIXfab/ESSenTIAL Approach," in *Optical Fiber Communication Conference*, 2012. **(Invited)**
- [7] B. Snyder and P. O'Brien, "Hybrid Laser Integration on Silicon-on-Insulator (SOI) with Compact Optical Isolator," in *Intel Ireland Research Conference (ERIC)*,

- Dublin, Ireland, 2012. [Online]. Available:
<http://www.intel.com/content/www/eu/en/education/eric/ireland-european-conference/presentations2/day2-bradley-snyder.html>
- [8] H. Chen, T. Koonen, B. Snyder, P. O'Brien, X. Chen, G. T. Reed, H. van den Boom, and O. Raz, "Packaged Mode Multiplexer based on Silicon Photonics," in *Asia Communications and Photonics Conference*. Optical Society of America, Nov. 2012, p. ATTh2B.4. [Online]. Available:
<http://www.opticsinfobase.org/abstract.cfm?URI=ACP-2012-ATTh2B.4>
- [9] B. Snyder and P. O'Brien, "Developments in packaging and integration for silicon photonics," in *Proc. SPIE 8614, Reliability, Packaging, Testing, and Characterization of MOEMS/MEMS and Nanodevices XII*, San Francisco, CA, USA, 2013, p. 86140D. [Online]. Available:
<http://proceedings.spiedigitallibrary.org/proceeding.aspx?articleid=1666331>
(Invited)
- [10] M. Rakowski, M. Pantouvaki, H. Yu, W. Bogaerts, K. de Meyer, M. Steyaert, B. Snyder, P. O'Brien, J. Ryckaert, P. Absil, and J. Van Campenhout, "Low-Power, Low-Penalty, Flip-Chip Integrated, 10Gb/s Ring-Based 1V CMOS Photonics Transmitter," in *Optical Fiber Communication Conference*. Optical Society of America, Mar. 2013, p. OM2H.5. [Online]. Available:
<http://www.opticsinfobase.org/abstract.cfm?URI=OFC-2013-OM2H.5>
- [11] B. Snyder, N. Pavarelli, and P. O'Brien, "Review of packaging and integration technologies for Silicon Photonics and implementation of an advanced foundry service," in *SPIE Photonics North*, 2013. **(Invited)**
- [12] H. Chen, R. van Uden, C. Okonkwo, B. Snyder, O. Raz, P. O'Brien, H. van den Boom, H. de Waardt and T. Koonen, "Employing an Integrated Mode Multiplexer on Silicon-on-Insulator for Few-mode Fiber Transmission," in *European Conference on Optical Communication (ECOC)*, 2013.
- [13] H. Chen, V. Sleiffer, B. Snyder, M. Kushnerov, R. van Uden, Y. Jung, C. Okonkwo, O. Raz, P. O'Brien, H. de Waardt and T. Koonen, "Demonstration of Photonic Integrated Mode Coupler with 3.072Tb/s MDM and WDM Transmission over 30km Few-Mode Fiber," in *18th OptoElectronics and Communications Conference / Photonics in Switching (OECC/PS)*, 2013.
(Post-Deadline)

Workshops

- [14] B. Snyder and P. O'Brien, "Packaging & Integration in Silicon Photonics," in *ePIXfab Full Training*, IHP Microelectronics, Frankfurt (Oder), Germany,

November 2012.

- [15] B. Snyder and P. O'Brien, "Packaging & Integration in Silicon Photonics," in *ePIXfab Full Training*, TNO, Eindhoven, The Netherlands, March 2013.

Posters

- [16] B. Snyder, H. Fernando, and P. O'Brien, "Characterization and Packaging of Grating-Coupled Silicon-on-Insulator (SOI) Photonic Devices," in *40th European Solid-State Device Research Conference (ESSDERC) Fringe Posters*, Sevilla, Spain, 2010.
- [17] B. Snyder, F. H. Peters, and P. O'Brien, "Silicon-on-Insulator (SOI) Nanophotonic Devices for Next-Generation Communications Systems," in *Intel European Research & Innovation Conference (ERIC)*, Leixlip, Ireland, 2010, p. 85.
- [18] B. Snyder and P. O'Brien, "Hybrid Integration Design for Lasers on Silicon Waveguides Using Micro-Optical Bench Technology," in *Photonics Ireland*, Malahide, Ireland, 2011.